INFLUENCE OF BREAKING BORES ON THE TRANSPORT OF MACROPLASTICS

PREET LALJIBHAI PATEL

A THESIS SUBMITTED TO
THE FACULTY OF GRADUATE STUDIES
IN PARTIAL FULFILLMENT OF THE REQUIREMENTS
FOR THE DEGREE OF
MASTER OF APPLIED SCIENCE

GRADUATE PROGRAM IN CIVIL ENGINEERING
YORK UNIVERSITY
TORONTO, ONTARIO

JUNE 2022

ABSTRACT

Each year there is an influx of several million tonnes of plastic into oceans. Transport and mobility of aquatic plastics are shaped by many factors including flow conditions. Surge waves - highly turbulent transient flows - observed in rivers and near coastal areas, can result in substantial turbulent mixing and have the potential to transport mismanaged plastic waste offshore. The transport of plastics in flow conditions induced by surge waves and the variation in the transport process owing to the changes in the hydrodynamic properties of a surge wave and macroplastic properties, have not been investigated. In this study, laboratory experiments were performed using a hydraulic flume, to produce surge wave Froude number ranging from 1.40 to 4.90. An in-house particle tracking velocimetry platform was used to capture the transport of macroplastics, which was simulated using solid macro-sized negatively buoyant acrylic, and positively buoyant high-density polyethylene and polypropylene plastic balls. The overall results highlight that the horizontal transport of all the macroplastics was governed by surge wave celerity and macroplastics initial momentum, while the vertical transport was influenced by surge wave Froude number. As macroplastics size decreased, there was an increase in horizontal and vertical transport, since it was easier to mobilize them against their buoyancy. This study illustrates that under high mixing conditions, plastics with marginal

density from water, can entrain heavily with the flow, moving against their buoyancy. This research highlighted the transport and mobility of aquatic plastics to promote a healthier and cleaner aquatic environment.

ACKNOWLEDGEMENTS

I would like to praise and thank the Almighty God.

I would like to sincerely thank my supervisors Dr. Magdalena Krol and Dr. Shooka Karimpour for their unwavering support and guidance throughout this entire journey. Your mentorship and encouragement have been truly invaluable, both personally and professionally. It has been an honour and a privilege to have worked with you. I would like to express my deepest appreciation for giving me this amazing opportunity.

I would also like to thank my committee members, Dr. Usman Khan and Dr. Roger Kempers.

I want to express my most sincere gratitude to our laboratory technician Riad Rajab for helping and providing his valuable feedback throughout the experimental setup. A special thanks to Stefan de Lasa for being a part of this journey.

I would like to express my deepest gratitude to my friends for being there for me throughout my graduate studies: Arefeh and Zhuoran.

I am extremely grateful to the Department of Civil Engineering, Lassonde School of Engineering, for this opportunity.

To my parents, thank you for always encouraging me to believe that I can accomplish anything I set my mind to. You let go of your dreams and sacrificed a lot so that I can achieve mine. A thank you is not enough to express your constant love, support, and encouragement. I would also like to thank my sister for always being there for me. I would not have been successful in all of my endeavours without my family. Finally, a special thank you to my friend Sagar Patel. I truly appreciate all your support and encouragement.

TABLE OF CONTENTS

LIST OF TABLES

LIST OF FIGURES

Chapter 1 – Introduction

1.1 Overview

With global plastics demands increasing, adverse effect of marine life and natural environment is inevitable. For example, there is substantial plastic waste present in aquatic and natural environment which has led to various environmental problems. Plastic production, waste generation, and the deleterious effects of litter on marine life and ecosystem have been well documented in literature (Geyer et al., 2017; Kühn et al., 2015; Plastics Europe, 2020). Plastic mobility and distribution in aquatic systems, however, is not well documented. In particular, understanding mobility and entrainment of plastic debris in intense turbulent phenomena, such as surge waves, which is often observed for instance in coastal areas is of importance. Surge waves are often induced by various instability mechanisms which lead to highly turbulent fronts. Although hydrodynamics properties of surge waves have been outlined in the literature, the transport mechanism of plastic debris in surge waves, induced near coastal regions and rivers, and the variation in the transport process due to the changes in the hydrodynamic properties of a surge wave have not been thoroughly studied. Therefore, the scope of this research is to comprehend the transport of plastic debris in a turbulent surge wave-induced motion. This research examined surge wave capacity and the effect of macroplastic's particle density and size on the approximate transport distance.

1.2 Aquatic Plastics - Background

Oceanic water sustains an incredible diversity of life and drives local and global economies. However, marine waste is increasing rapidly due to growing population and increasing urbanization, and this has impacted more than 800 species of marine wildlife (Secretariat of the Convention on Biological Diversity, 2016). The two primary adverse effects of marine plastic pollution on various species are entanglement in marine waste and ingestion of marine litter (Kühn et al., 2015). Entanglement restricts marine species swimming ability, restricts breathing, and disrupts feeding (Kühn et al., 2015; Laist, 1997). Entanglement of marine wildlife has been reported across the world, from the Arctic (Knowlton et al., 2012), to the Southern Ocean (Waluda & Staniland, 2013). Entanglement was reported for various species group, including seabirds, marine ducks, penguins, whales, seals, otters, polar bear, turtles, sea snakes, invertebrates, other fish species, and marine birds, mammals and turtles (Kühn et al., 2015). One of the most common objects these species are entangled in are ghost fishing gear, which is either lost or abandoned at sea. In addition, marine waste is usually mistaken for food and is commonly ingested by marine life, and this may block their digestive tract (Laist, 1997). Injection of marine debris have been documented for various species, including seabirds, marine ducks, penguins, whales, seals, turtles, invertebrates, fish species, and turtles (Kühn et al., 2015). According to Laist (1997), the number of marine species documented worldwide for marine waste entanglement and ingestion was 136 and 177, respectively. Increased marine waste has resulted in higher incidence of marine life entanglement and ingestion. A recent study reported that the number of marine species entangled in marine debris increased from 136 to 344, and marine life documented with ingestion of marine debris increased from 177 to 331 marine species (Kühn et al., 2015). Marine pollution can consist of plastic, glass, metal, rubber, wood, and composite material; however, plastic is the primary type of marine waste in oceanic waters (Kornei, 2017). Although it is reported that plastic represents 60% to 80% (Gregory & Ryan, 1997) of total marine debris, some studies estimate it as high as 92% (Derraik, 2002) making it a serious problem for marine life.

1.2.1 Plastics consumption - Entanglement

Entanglement of marine life in plastic debris is more visible than plastic ingestion and is often related to larger plastic debris. Marine species have been entangled in fishing nets, polypropylene packaging straps, plastic bags, and rubber O-rings (Greg Hofmeyr et al., 2006). Entanglement have been reported for fur seals, sea lions, fulmars, green turtles, right whales, and loggerhead turtles (Secretariat of the Convention on Biological Diversity and the Scientific and Technical Advisory Panel – GEF, 2012). Entanglement has been recorded for various marine species all over the world including Antarctic fur seals in the subantarctic island (Greg Hofmeyr et al., 2006), right whales in North Atlantic (Knowlton et al., 2012), and rabbitfish in Japan (Matsuoka et al., 2005) along with others (Adimey et al., 2014; Gregory, 2009; E. Moore et al., 2009; M. Moore et al., 2013; Page et al., 2004; Rodríguez et al., 2013; Ryan, 2018; Stelfox et al., 2016). Entanglement in plastic waste can lead to suffocation, limited mobility due to strangulation, and possibly death (Benjamins et al., 2012; Kühn et al., 2015; Laist, 1997; Stelfox et al., 2016).

1.2.2 Plastics consumption - Ingestion

Plastic pollution poses risk to marine wildlife, the natural environment, and the human food chain. The two main concerns revolving around marine plastics are ingestion and entanglement. Recent studies stated that 52% of turtles and 90% of seabirds have ingested marine plastics (Schuyler et al., 2016; Wilcox et al., 2015). Annually, marine plastics pose risk to more than 100,000 sea turtles and is responsible for the death of over a million sea creatures (Pincetich et al., 2010). Ingestion of plastic debris occurs worldwide, from the Murres in northwestern Atlantic (Bond et al., 2013), Puffinus Tenuirostris in northern Pacific (Yamashita et al., 2011), and Northern Fulmar Fulmarus in the North Sea (van Franeker et al., 2011), to mesopelagic fishes in South Atlantic (McGoran et al., 2021), and fishes in the South Pacific Subtropical Gyre (Thiel et al., 2018). Ingestion of plastic debris is also reported for marine turtles, whales, seals, and seabirds (Kühn et al., 2015; Laist, 1997; Lenzi et al., 2016). Several other species have also been documented globally for consuming plastic debris (Besseling et al., 2015; Boerger et al., 2010; Bravo Rebolledo et al., 2013; Bugoni et al., 2001; Colabuono et al., 2009; Davison & Asch, 2011; Jiménez et al., 2015; Lusher et al., 2015; Mrosovsky et al., 2009; Osinga & 't Hart, 2006; van Franeker & Law, 2015). Once plastic waste is ingested, it can release toxic chemicals and travel up the marine food chain (Browne et al., 2008; Chua et al., 2014; Mizukawa et al., 2009; Santos et al., 2021; Wardrop et al., 2016), which may eventually end up in the human food chain (Forrest & Hindell, 2018; Kosuth et al., 2018; Ohta et al., 2002; Rochman et al., 2015; van Cauwenberghe & Janssen, 2014).

1.2.3 Plastic production

The widespread application of versatile synthetic and semi-synthetic polymers have led to the production of 8.3 billion tonnes of plastics since the start of the plastics industry in the 1940s. Commonly used products containing plastic polymer are reported in Table 1-1. Countless benefits of plastics in numerous sectors led to the global production of 368 million tonnes of plastics in 2019 (Plastics Europe, 2020), an increase of 9 million tonnes from 2018 (Plastics Europe, 2019). With the current consumption rate, annual global plastic production is expected to reach 1.1 billion tonnes by 2050 (Ellen MacArthur Foundation, 2016), equating to a cumulative plastics production of 33 billion tonnes (Rochman et al., 2013). The current ratio of plastics to fish in the ocean (by weight) is 1:5 but plastics in the ocean are expected to weigh more than fish by 2050 (Ellen MacArthur Foundation, 2016). A total of 6.3 billion tonnes of plastic waste has been generated as of 2015 (Geyer et al., 2017) and of this, roughly 600 million tonnes (9%) have been recycled, nearly 800 million tonnes (12%) have been incinerated, while approximately 4.9 billion tonnes (79%) accumulate in landfill or the natural environment (Geyer et al., 2017).

Table 1-1. Common uses of high demand plastic polymers (Plastics Europe, 2020).

Polymers	Common Uses
High-density polyethylene (HDPE)	Milk containers, cleaning agents and cosmetic containers, toys, pipes, hardware, etc.
Low-density polyethylene (LDPE)	Plastic bags, food wrappers, agricultural film, trays, etc.
Polypropylene (PP)	Food packaging, bottle lids, food containers and wrappers, microwave containers, pipes, automotive parts, bank notes, etc.
Acrylic (ACR)	Lenses, paint, glass replacement, home improvement

Beneficial properties of plastics and its relatively inexpensive production, allow this material to define everyday life. According to Plastics Europe (2020), polypropylene (PP) and polyethylene (PE) accounts for nearly 50% of the global plastics market (Table 1-2). Not surprisingly, these two polymers are also predominant in the aquatic environment, from beaches and surface levels to deep-sea sediments. Plastics density (Aksit et al., 2019; Harper & Petrie, 2003; Singhal et al., 2012) and size classification varies greatly (Eriksen et al., 2014; Hartmann et al., 2019; Isobe et al., 2014). Five plastic size classification are used when studying aquatic plastics (Table 1-3). While several other studies often extend the size range for microplastics to include plastic debris of 1 µm to 5 mm (GESAMP, 2016; Schwarz et al., 2019). Primary microplastics are less than 5 mm in size before they arrive in the marine environment and secondary microplastics are plastics which are greater than 5 mm before ending up into the marine environment. Macroplastics and mesoplastics can potentially contribute to microplastics pollution (also known as secondary microplastics), as they are degraded by ultraviolet radiation (sunlight), wind abrasion, and wave action, leading to smaller plastic particles.

Table 1-2. Breakdown of global plastic demand (Plastics Europe, 2020).

Polymer type	Density (g/cm^3)		Global plastic demand distribution in 2019 (Plastics Europe, 2020)	
	Min	Max	Percentage	$*10^6$ tonnes
Polypropylene (PP)	0.89	0.92	19.40%	71.39
Polyethylene (LDPE/LLDPE)	0.88	0.93	17.40%	64.03
Polyethylene (HDPE/MDPE)	0.93	0.97	12.40%	45.63
Polyvinyl Chloride (PVC)	1.15	1.58	10.00%	36.80
Polyethylene Terephthalate (PET/PETE)	1.29	1.40	7.90%	29.07
Polyurethane (PUR)	0.02	1.30	7.90%	29.07
Polystyrene (PS/EPS)	0.05	1.10	6.20%	22.82
Others (plastics + thermoplastics)	0.15	2.20	18.80%	69.18
Freshwater density (ρ_w)	~ 1.00		–	
Seawater density (ρ_{ws})	~ 1.03		–	

The presence of plastics has been observed throughout different environmental compartments including marine and aquatic environments. A total of 11.6 – 21.1 million tonnes of 32 – 651 µm plastics are suspended in the Atlantic Ocean (Pabortsava & Lampitt, 2020). Assuming a constant concentration of plastics across the Atlantic Ocean, leads to an estimated 200 million tonnes of PE, PP, and polystyrene (PS) currently circulating in the Atlantic Ocean (National Oceanography Centre UK, 2020). Plastics have been rapidly accumulating in the five garbage patches: the North Pacific Gyre (L. Lebreton et al., 2018) the South Atlantic Gyre (Ryan et al., 2019), the North Atlantic Gyre (Law et al., 2010), the South Pacific Gyre (L. Lebreton et al., 2018), and the Indian Ocean Gyre (Maximenko et al., 2012).

Table 1-3. Plastics size classification.

Classification	Size
nanoplastics	1 nm – <1 µm
microplastics	1 µm – <1 mm
mesoplastics	1 mm – <1 cm
macroplastics	1 cm – <1 m
megaplastics	1 m <

1.2.4 Polymer distribution in the marine environment

The marine environmental compartment can be divided into four categories with respect to plastic accumulation: beaches, surface water, water column, and deep-sea sediments (Figure 1-1). The following section will describe these environments and the plastic composition often found in these areas.

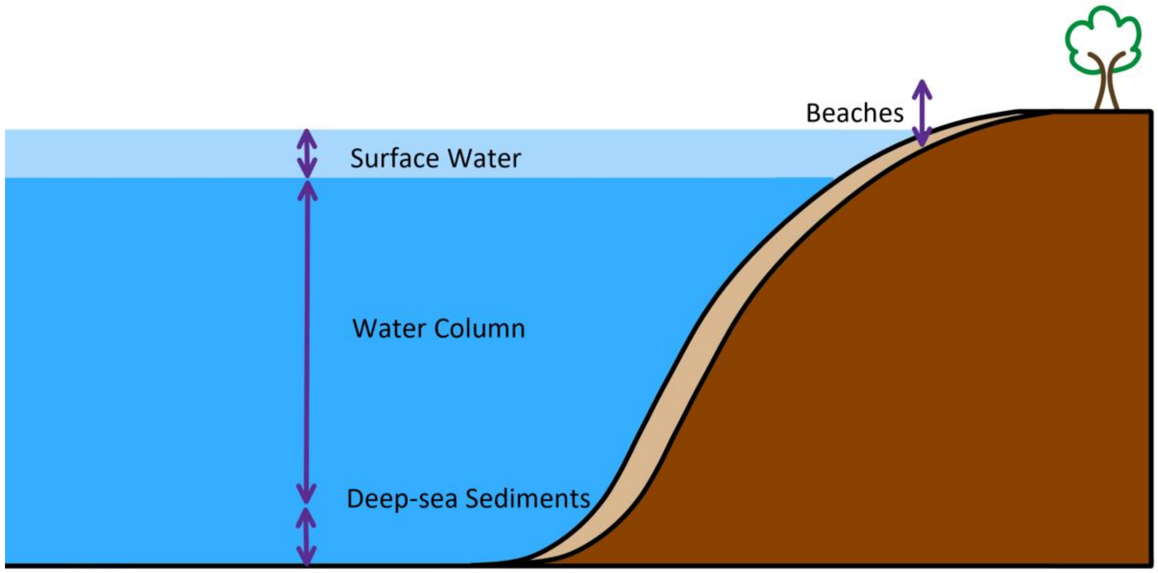

Figure 1-1. Marine environmental compartments.

Polymer composition – beaches

Frequent use of beaches for tourism and recreational activities may increase plastic waste along the shorelines, which may seep into aquatic environment. Plastics have been reported on both freshwater and marine beaches. A study that investigated the distribution and degradation of mesoplastics and macroplastics along freshwater beaches of Lake Erie, St. Clair, and Huron, found that PE and PP were predominant polymer types in the 5,602 plastics samples collected (Zbyszewski et al., 2014). Similar studies carried out along the beaches of freshwater Lake Huron (Zbyszewski & Corcoran, 2011) the lake shores in south Central South America (Blettler et al., 2017, 2019) and along the Nandoni freshwater reservoir in South Africa (Dalu et al., 2019), reported the prevalence of both PE and PP polymers. While plastic abundance has been documented along freshwater shorelines (Dalu et al., 2019), PE and PP were also reported in marine environments. For example, PE and PP was observed on the beaches along the west coast of India (Maharana et al., 2020), on six beaches investigated in Central Chile (Gómez et al., 2020), and along the Ookushi Beach, Japan (Nakashima et al., 2012). Microplastics distribution in freshwater beaches and ocean beaches is also prevalent. A review study on microplastics pointed out that PE and PP dominated sea surface samples for both freshwater beaches and ocean beaches (Schwarz et al., 2019).

Polymer composition – surface water

A study in 2014, estimated 390 billion pieces of mesoplastics and macroplastics are afloat at sea (Eriksen et al., 2014). Mesoplastics and macroplastics pollution on top of the surface water layer (from top of the water layer to few meters of water depth) varies from 6,350 – 31,751 tonnes (Cózar et al., 2014) to 211,736 tonnes (Eriksen et al., 2014); while a recent study carried out in 2016 estimated that 258,700 tonnes of macroplastics are currently circulating at the surface water layer (Koelmans et al., 2017). Macroplastics have been observed as far as Amundsen Sea, West Antarctica, despite having virtually no human presence (Barnes et al., 2010), pointing to transport of the particles through currents and wave motions. In terms of polymer types, PE and PP seems to be the dominant plastic found on the surface water. Presence of PE and PP have been found in large quantities in freshwater reservoirs across the world, and studies carried in marine environment yielded similar results. A total of 59 surface water samples collected across freshwater Lake Michigan indicated that PE was more prevalent, followed by PP (Mason et al., 2016). Large quantities of plastic bags (PE – packaging, films, wrappings, and sheets) was the primary source of waste along the surface water of the Mediterranean French coast (Di-Méglio & Campana, 2017). In addition, studies conducted in surface water reported the dominance of PP and PE (Gasperi et al., 2014; Lahens et al., 2018; Sadri & Thompson, 2014). A review study found that PE was the most common polymer floating in urban rivers (Al-Zawaidah et al., 2021). Microplastics distribution in surface water also showed similar results. Several studies conducted on microplastics concluded that PE and PP were predominant in surface water (Athapaththu et al., 2020; Mason et al., 2016; Zeri et al., 2018). A review study by (Erni-Cassola et al., 2019) investigated 17 surface water studies; PE and PP were prevalent in marine microplastics litter. The overall data suggest that low-density polymers (e.g., PE and PP) are predominant at the surface water layer in both freshwater and seawater reservoirs across the globe.

Polymer composition – water column and deep-sea sediments

Water column (space between the ocean's surface and floor) and deep-sea sediments (ocean floor) are accumulation zones and sinks for plastics. Macroplastics contribute to secondary microplastics, which eventually accumulates in deep-sea sediments and the water column. Polymer composition of macroplastics in the water column and deep-sea sediments are not well documented. However, composition of microplastics in the water column is well researched. A review study in the epipelagic zone (200m >) analyzed microplastics distribution in freshwater and ocean water column; PE and PS were predominant in marine water column, while other plastics were prevalent in freshwater water column (Schwarz et al., 2019). Another review study stated that polyester, polyamide, and acrylic were more common in the water column (Erni-Cassola et al., 2019), and similar distribution was obtained by Choy et al. (2019). Meanwhile, polymer distribution in deep-sea sediments was found to be more diverse than in the water column. A review paper in freshwater and ocean sediments stated that polyester, polyamide, and polyacrylonitrile were often encountered in deep-sea sediments (Schwarz et al., 2019). While another review paper revealed that polyester, polyamide, and acrylic were predominant in deep-sea sediment (Erni-Cassola et al., 2019). The variation in polymer distribution may be influenced by local activities, industries, and sampling methods. Additional research is required in water column and deep-sea sediment to comprehend macroplastics and microplastics polymer distribution. Nonetheless, the presence of plastics in the water column and deep-sea sediment is concerning for marine organisms and natural environment.

1.3 Transport pathways

Plastics can enter marine environments from various land-based sources and off-shore pathways. Land-based sources are responsible for 80% of global annual plastics inputs, while the remaining 20% originates from off-shore routes. Entry pathways are shown in Table 1-4.

Table 1-4. Land-based and off-shore macroplastics entry pathways. Adapted from Lechthaler et al. (2020).

	Land-Based Sources	Off-shore Sources
Littering	1. Local 2. Tourism 3. Activities and events	1. Illegal dumping at the sea
Industry	1. Demolition and construction 2. Agriculture activities 3. Industrial activities	1. Fishing activities 2. Aquaculture activities
Natural storm events	1. Local agencies 2. Mismanaged waste treatment/disposal 3. Vulnerable landfills in the vicinity of coasts and water courses 4. Coastal infrastructure	1. Cargo lost at sea
Waste management	1. Discharge of untreated municipal stormwater and sewage 2. Municipal landfill waste 3. Waste lost during transport	1. Commercial shipping 2. Exploration vessels 3. Private cruises 4. Public shipping

Coastal events are the primary transport pathways for plastic waste, followed by world rivers. In 2010, 275 million tonnes of plastic waste were generated by 192 countries (Jambeck et al., 2015). Of this, approximately 99.5 million tonnes of plastic waste were produced within 50 km of the coastline (Jambeck et al., 2015). From this, an estimated 31.9 million tonnes were categorized as inadequately managed plastic waste (Jambeck et al., 2015), which is readily available to be transported to the marine environment. In 2010, up to 12.7 million tonnes of plastic litter made its way into the ocean (Jambeck et al., 2015) but the amount of plastic debris that flows into the oceans annually is expected to increase with growing plastics demand and production. In addition, coastal events (e.g., flood events, surge waves, and tsunamis) have the potential to transport inadequately managed waste near the coastline to the marine environment. Destructive nature of tsunami waves drives millions of tonnes of debris into marine environment; this amount can be within the range of annual global plastics input into the oceans. For example, the city most affected by the 2004 Indian Ocean tsunami generated 10 million m^3 of debris (Bjerregaard, 2010); most of which washed into the Indian Ocean. Similarly, there was an influx of 5 million tonnes of debris in the Pacific Ocean due to the 2011 Tohoku tsunami (Ministry of the Environment, Japan 2012). Of this, 3.5 million tonnes sank to the seabed, near Japan's coast, while the remaining 1.5 million tonnes is still floating in oceanic water (Ministry of the Environment, Japan 2012).

World rivers are also responsible for transporting plastic litter from inland sources to the marine environment. The estimates of plastics transported by riverine systems diverge greatly between 0.41 million tonnes to 4 million tonnes (L. C. M. Lebreton et al., 2017; Meijer et al., 2021; Schmidt et al., 2017). Twenty of the world's most polluting rivers, located primarily in Asia, were transporting nearly 67% of global riverine plastics input, despite covering 2.2% of continental landmass (L. C. M. Lebreton et al., 2017).

There are several other transport mechanisms which move plastics from inland sources to the marine environment. Even weak turbulence can lead to the resuspension of particles. In addition to the surface currents (turbulence and currents) and meteorological conditions (winds), macroplastics accumulation and transport is largely impacted by their size, density, and shape (van Utenhove, 2019).

1.4 Plastic mobility in aquatic systems:

1.4.1 Settling and rising

Settling and rising of a particle in a stationary fluid has a notable impact on its transport. Three primary forces (gravitational, buoyancy, and drag) act on a particle settling or rising in a quiescent fluid. When the net forces acting on a particle are zero, the particle settles with a constant velocity, commonly referred to as terminal velocity. Positively buoyant plastics (e.g., PE and PP) tend to stay near the surface level, as discussed in the polymer composition section 1.2.4. The rising and settling of microplastics in a quiescent fluid can occur due to biofouling and defouling. The growth of microorganisms on particle surface can lead to sinking, even for positively buoyant particles. As particles sink further, photodegradation occurs due to absences of sunlight, promoting defouling (Ye & Andrady, 1991). As a result of biofouling and defouling, microplastics' settling may continuously fluctuate in the water column (Kooi et al., 2017).

1.4.2 Windage

Low density plastics, such as PE and PP are highly susceptible to surface current, wind forces, and waves. Particle transport owing to wind forces is known as windage, also referred as leeway drift. In addition to surface currents, wind forces may also impact plastic particle's velocities and trajectories.

Microplastics can be redistributed throughout the water due to leeway drift. For buoyant particles, wind force acts on the particle's surface area which is situated above the surface level, this results in drift followed by drag forces. Not surprisingly, particles with higher unsubmerged volume are more susceptible to leeway drift. Numerical simulation by Chubarenko et al. (2016), indicated that a spherical PE particle can travel 250 km (across the Baltic Sea) in roughly a week, under moderate winds. The transport speed is independent of the particle size, and it is governed by the ratio of the unsubmerged volume to submerged volume (Chubarenko et al., 2016). This suggests that macroplastics can be transported large distances, if the ratio of unsubmerged to submerged volume is sufficient.

Wind forces are the driving factors for ocean circulation, and Ekman currents are a product of wind forces and ocean circulations. Frictional forces owing to windage, usually drags the upper 100 meters of water layer from west to east, meanwhile Coriolis effect pushes ocean water perpendicular from the direction of wind force. Since the Coriolis force acts in different directions in both the northern and southern hemisphere, Ekman spiral occurs perpendicularly in the clockwise direction and in counter clockwise direction from the northern hemisphere and southern hemisphere, respectively. Ekman currents are the result of two different natural phenomena: net water transport owing to frictional forces due to wind and Coriolis effect. Transport and accumulation of plastic wastes near the water surface are considerably influenced by Ekman currents (Onink et al., (2019).

1.4.3 *Mobility in sediments*

Thermohaline circulations are the main source of energy of bottom currents and global density gradients are the driving component, which are governed by temperature gradients (thermo) and variation in salinity (haline). When the sea ice is formed near the polar regions, salt is left behind. Consequently, salinity in the ambient water increases, and the heavier fluid with higher salinity settles to the ocean basin. Subsequently, surface water is advected to replace the settling of the fluid with high salinity. This ongoing movement of surrounding water freezing, heavier ambient fluid settling while surface water is driven in, is the primary process behind the ocean conveyor belt thermohaline circulation (NOAA, 2013).

Transport of microplastics across seafloor has been documented to some extent. Field data and surface circulation models show that the thermohaline process transferred floating debris to Greenland and Barents seas, which began their journey in the north Atlantic (Cózar et al., 2017). Several other studies have reported the transport of plastics in deep-sea sediments are controlled by thermohaline circulation (Bergmann et al., 2017; Kane et al., 2020).

1.4.4 *Turbulent Entrainment*

Marine and freshwater systems are often deemed turbulent, which largely contributes to the distribution and mixing of plastics. Near coastal areas, along with wind generated turbulence, the effect of breaking waves and other coastal phenomenon also transports plastic debris. For example, tsunamis have the potential to relocate millions of tonnes of debris (Bjerregaard, 2010; Ministry of the Environment, Japan 2012). Similarly, wind-induced turbulence facilitates Langmuir circulation, which can submerge positively buoyant particles. Langmuir circulations are developed when surface wind travels above the sea layer, forming counter-rotating vortices parallel to the direction of surface wind. Strong winds induced stronger Langmuir circulations, which can expedite the settling of positively buoyant debris. The vertical shear in Langmuir turbulence due to downwind and crosswind is weaker than that Ekman turbulence (Liang et al., 2018). However, the Langmuir turbulence in the first few meters of water column has higher vertical shear due to downwind currents than that of the Ekman currents, since there is a rapid decrease of the Stokes drift (Liang et al., 2018). Furthermore, the mixing of debris in the boundary layer and the vertical shear in the horizontal velocity determines the horizontal dispersion (Liang et al., 2018).

Particles are also transported along the seafloor due to the movement of fluid across the ocean basins. The driving factor is density variation which is a result of differential temperature and variation in salinity. High density materials will ultimately sink to the seafloor and low-density debris will also sink due to biofouling, and thermohaline currents govern the transport of these debris, present on the seabed. Plastics also arrive at the seafloor due to gravity currents. Concentration of plastic pollution at the river mouth is a magnitude greater than in open waters, and this immediate fluvial inputs from river discharge contribute to turbidity currents (Kane & Clare, 2019). Turbidity currents deposit large quantities of plastics to seafloor which are then advected by bottom currents. Sediment laden flow should have sufficient turbulent energy to keep sediments in suspension (Knoblauch, 1999). Plastics with densities greater than that of sea water are prone to turbidity currents in the water column. An experimental study performed by (Pohl et al., 2020), indicated that the turbidity currents have the potential to transport and deposit large quantities of microplastics to deep-sea sediment. From there the thermohaline process would further transport plastic particles along the seafloor and deep-sea trenches. Deep-sea currents have significant impact on marine food chain, ecosystems, and microorganisms since they are effective in distributing oxygen and nutrients. Unfortunately, the same deep-sea currents that transfer oxygen and nutrients, can also move plastic debris.

Effect of turbulence mixing has a great impact on particle transport. Experimental and numerical work shows that as turbulence increases, regardless of the particle Stokes number, the settling velocity also increases (Kawanisi & Shiozaki, 2008). Whereas for intermediate turbulence, settling velocity of particles with large Stokes number decreases, while the settling velocity of particles with smaller Stokes number is higher (Kawanisi & Shiozaki, 2008). Stokes number is a non-dimensional parameter which represents the ratio of the particle relaxation time (Eq. 1-1) to the time scale. A review study conducted by Dey et al. (2019) investigating the particle settling from experimental observations and numerical simulations, stated that in a flow with low to intermediate turbulence intensity, the particle motion is governed by Stokes number, defined below (Eq. 1-2).

Particle entrainment is also influenced by its density, size, and the density of the ambient fluid. The correlation between particle size, fluid viscosity, particle density, and the density of the ambient fluid is defined by the particle relaxation time, τ_p:

$$\tau_p = \frac{D^2(\rho_p - \rho_w)}{18\mu} \qquad \text{Eq. 1-1.}$$

where D is the particle diameter, ρ_p is the particle density, ρ_w is the fluid density, and μ is the dynamic viscosity of the fluid. Particle relaxation time is used to define the natural vertical tendency of the particle in the fluid (Eq. 1-1). Increase in particle diameter or marginal density from that of ambient water, or both, increases the particle relaxation time. Smaller particles (e.g., smaller microplastics) display lower particle relaxation times and are good passive tracers, as reviewed by Shamskhany et al. (2021). Particles with lower Stokes numbers indicated higher turbulence time scales or lower particle relaxation time. The influence that small-scale turbulence has on the particle motion is characterized by the Stokes number, St:

$$St = \frac{\tau_p}{(u_1 + c)/g} = \frac{gD^2(\rho_p - \rho_w)}{18\mu(u_1 + c)} \qquad \text{Eq. 1-2.}$$

where g is gravity, c is surge wave celerity, and u_1 is the upstream velocity. The velocity used in the Stokes number calculation was the sum of upstream velocity and celerity. Using just the upstream velocity will not define the effect of the celerity, and using just celerity would ignore the influence of plastic particles initial momentum due to upstream velocity. The combination of both upstream velocity and celerity can determine plastic particle's Stokes number much more accurately. The ratio of small-scale turbulence and particle relaxation time defines the Stokes number. The Stokes number is used to describe the behaviour of a particle in a fluid flow. A smaller Stokes number suggest that the particle will easily be able to adapt to the new environment. Since the particle interaction with the ambient structure will not lag as much as a larger particle. A particle with larger Stokes number is associated with lower time scale or higher particle relaxation time. Consequently, larger particles will be influenced by their natural tendency to sink or rise, and will be inclined to stay on its original path, requiring longer time to relax to the newer environment.

1.5 Surge wave dynamics

Surge waves are generated in natural channels and humanmade canals due to sudden change in flow, including depth, pressure, or velocity. Transient flow conditions in oceanic waters are generated by natural disasters, such as underwater earthquakes, volcanic eruptions, landslides, and weather. These events trigger a large-scale displacement in oceanic waters, which results in a series of long waves i.e. tsunamis. Tsunami waves radiate outward in all directions from the source of generation and can transport particles large distances. In deep water, tsunami waves with large wavelengths propagate rapidly with wave speeds of up to 800 km/hr (John P. Rafferty & Kenneth Pletcher, 2021). When tsunami waves reach shallow waters near the coastal region, their wavelength decreases and wave height increases, by a magnitude or two, also known as wave shoaling effect (Figure 1-2). Tsunami waves arrive onshore with wave heights that can reach several tens of meters

(Britannica, 2021), resulting in severe unforeseen damage on coastal communities. Such a phenomenon is responsible for countless deaths and billions of dollars in damage. The 2004 Indian Ocean tsunami triggered by undersea earthquake resulted in at least 225,000 deaths (Britannica, 2021) forcing millions to relocate, and left an economic damage of billions of dollars, across several countries, making it one of the deadliest natural disasters. Similarly, in 2011, the Great East Japan Earthquake triggered the Tohoku tsunami. This led to the death of more than 18,500 people (John P. Rafferty & Kenneth Pletcher, 2021), and left an estimated economic damage of over $200 billion.

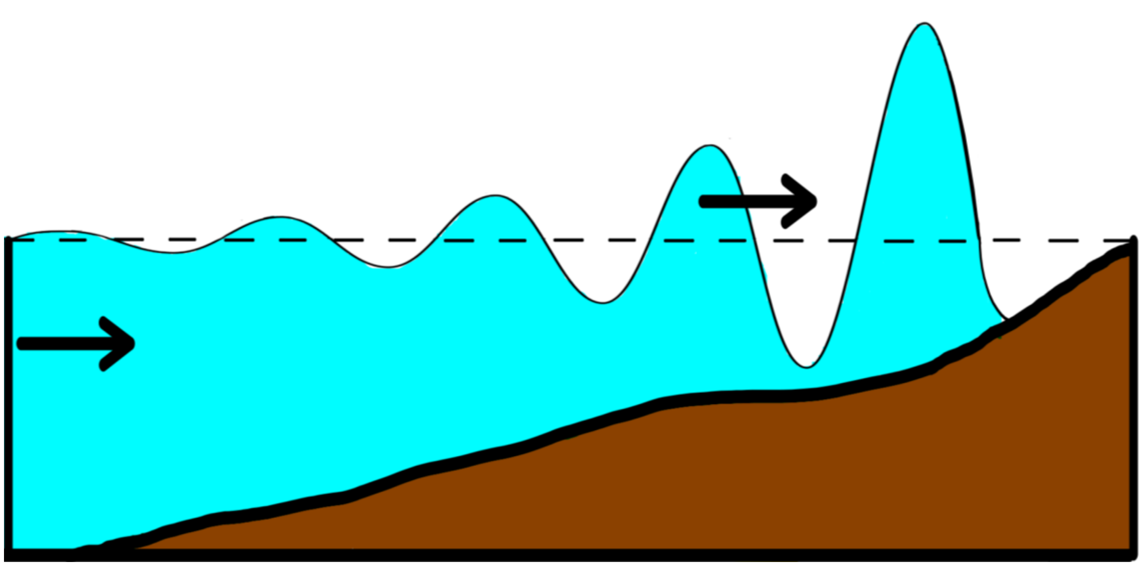

Figure 1-2. Cross section of a coastal region during a tsunami, where the wave shoaling effect amplifies the wave height.

Tsunami waves are well-known example of surge waves, where the leading water surface advances against an estuary with an incoming flow. Both tsunami and surge waves have similar hydraulic characteristics; however, surge waves are generated in rivers and narrow water channels. Both tsunami waves and surge waves are modelled as solitary waves (Xie & Chu, 2019; Zhang et al., 2015), and have the potential to transport large quantities of debris. Surge waves have substantial influence on estuaries and river mouths, where debris is suspended owing to wave motion, and bed erosion is initiated underneath the surge front (Koch & Chanson, 2008). This process gives a sharp rise to sediment concentration in the water column. Turbulent mixing produces large turbulent magnitudes and turbulent stress fluctuations below the surges (Chanson, 2011). Turbulent mixing at the surge wave front can then transport marine waste and deposit it elsewhere. As a result, surge waves fronts have intensive air entrainment and strong turbulence mixing, which have significant impact on sediment transport, and eco-systems.

Such a phenomenon is observed in nature when an earthquake, landslide, or volcanic eruption releases energy which displaces the overlaying water. In addition, removal and closure of a gate within a channel can produce a positive and a negative surge wave which rapidly advances away from the source of generation with its propagation velocity, also known as celerity. In an open channel flow, a partially closed gate results in two different water elevations, higher water depth before the gate, upstream, and lower water depth after the gate, downstream. Gate removal of a partially closed sluice gate will produce a positive surge wave propagating in the downstream direction and negative surge wave advancing in the upstream direction. Conversely, in an uninterrupted flow, sluice gate closure will generate a negative surge wave propagating towards the downstream of the channel and positive surge wave advancing towards the upstream of the channel, see Figure 1-3. Positive surge waves are stable and progress uniformly. Whereas negative surge waves are unstable and diminish immediately as the receding wave becomes flatter while travelling away from the source of generation.

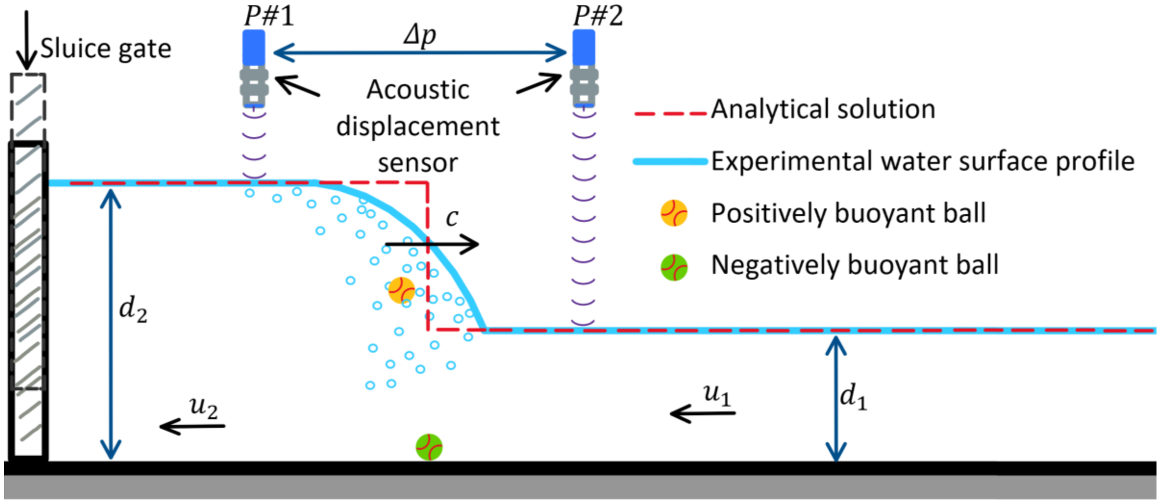

Figure 1-3. Gate closure generates a positive surge wave propagating against the incoming flow. Parameters closer to the outlet and inlet are referred to as downstream and upstream, respectively. The upstream water depth is denoted as d_1, upstream velocity is u_1, celerity is c, downstream water depth is d_2, and downstream velocity is u_2.

To satisfy conservation of mass, breaking surge waves experience a sudden change in water depth which leads to a rapid change in the longitudinal velocity (Chanson & Lubin, 2013). Surge waves are categorized as an undular surge wave, which has a gradual surge front followed by a train of wave undulations, or as a breaking surge wave, which has a steep surge front with significant turbulent kinetic energy and air entrainment in the surge wave roller. The strength of a surge wave can be defined by its Froude number, Fr_s:

$$Fr_s = \frac{u_1 + c}{\sqrt{g d_1}} \qquad \text{Eq. 1-3.}$$

Literature suggests that the undular surge wave is produced when $Fr_s < 1.3$, undular surge wave with slight breaking at the first wave front is formed when $1.3 < Fr_s < 1.45 – 1.5$, and breaking surge wave is created for $Fr_s > 1.45 – 1.5$ (Chanson, 2010a, 2010b, 2011).

In an undular surge wave, bed erosion is initiated beneath every wave crest which gives rise to sediment concentration in the water column. Suspended debris could be carried away by wave motion (propagation of disturbances) and well developed free-surface undulations (Chanson & Lubin, 2013). Whereas, in breaking surge wave sediment concentration in the water column increases when the bed is destabilized due to the surge wave roller. The suspended debris is advected upstream by the bed load motion, and debris is transported further upstream due to the recirculation region. Such a breaking surge wave introduces air entrainment and strong turbulent mixing (Chanson, 2010b) this has substantial effect on eco-system and sediment transport process.

1.6 Motivation

Research efforts have been devoted to investigate plastics production (Plastics Europe, 2020), plastic waste generation (e.g., Geyer et al., 2017; Jambeck et al., 2015), possible transport pathways (L. C. M. Lebreton et al., 2017; van Utenhove, 2019), and polymer composition (e.g., Koelmans et al., 2017; Zbyszewski et al., 2014). In addition, the adverse consequences of plastic waste on marine wildlife (ingestion and entanglement) has been studied by various authors (Bond et al., 2013; Kühn et al., 2015; Laist, 1997), as have the effects of plastics on the human food chain (Forrest & Hindell, 2018; Kosuth et al., 2018; Rochman et al., 2015).

Figure 1-4. Photograph of waves of plastic waste (mainly one time use plastic bottles) washing onto a beach in Durban, South Africa. Photographs obtained from a The Litterboom Project (2020) video.

The transport of plastics in marine and freshwater systems are often linked to the plastics' buoyancy. However, as described in the literature review, plastics lighter than freshwater and seawater are found in deep-sea sediments while heavier plastics can be found at the surface. Turbulent mixing has a critical role on the entrainment of plastics, even in the macro sized range, and on the transport of debris. Images of surge waves and tsunami waves have surfaced on the internet carrying large quantities of plastic debris and objects within the range of megaplastics (Figure 1-4). Although, the influence of surge waves and tsunami waves (i.e., wave force and wave drag coefficient) have on coastal infrastructures and seawalls are also well understood (Linton et al., 2013; Ramsden, 1996; Xie & Chu, 2019), the impact of tsunamis and surge waves on the transport of plastic debris have not been well studied and documented. In particular, the effect of particle size, density and surge wave strength on transport and entrainment remains poorly understood.

Therefore, this research aims to investigate the entrainment of macroplastic in surge waves. In particular, the goal is to i) analyze surge wave capacity and their role on the transport of predominant plastics of various densities (i.e., PP, HDPE, and ACR) in a marine environment, and ii) to provide early-stage evidence that turbulent flow can alter the sinking and rising patterns of plastics, even at the marco-size range.

1.6.1 Contributions of research and anticipated outcomes

Surge waves with high Froude numbers will result in higher turbulent kinetic energy and substantial air entrainment, promoting intense mixing and changing the course of floating plastic debris. This study has resulted in improved understanding of surge waves and their role on the transport of floating debris of various sizes and densities (particle trajectory, velocity, and horizontal and vertical transport in surge waves), by analyzing surge waves properties and particles properties (i.e., density and size). Furthermore, this study investigates the role of macroplastic density and size on their entrainment and mobility in highly turbulent flow. Influence of macroplastics density and size was examined for a wide range of surge wave Froude numbers. The results provide insight into the differences and similarities in macroplastics horizontal and vertical transport across surge wave with a wide range of surge wave Froude number. Entrainment of negatively and positively buoyant macroplastics have been observed and quantified. The results provide insight into how negatively buoyant macroplastics behave similar to positively buoyant macroplastics at higher surge wave Froude number. This research presented the first evidence of two distinct transport process of positively buoyant macroplastics in highly turbulent surge wave.

This research also greatly contributes to the inexpensive in-house experimental setup of open-source particle tracking velocimetry (PTV) program. The novelty of this experimental procedure may promote the use and the exploration of in-house PTV technique, to measure particles' velocities and trajectories. Furthermore, this research will also inspire the limitations of open-source PTV programs to be addressed.

Exploratory findings may yield new insights and lead to further novel research to explore surge wave capacity, and transport of plastics across the surge wave (along the flume width in the 3D). This research may also initiate studies on the impact of coastal infrastructures due to surge waves and lead to a healthier and cleaner aquatic environment.

1.6.2 Thesis Structure

- Chapter 1 (current chapter): Presents an outline on the plastics pollution in different marine environments, followed by describing the adverse effects of plastic pollution on marine wildlife. Moreover, plastics production and waste generation is reviewed. Furthermore, potential transport pathways, mobility of plastics, and influence of turbulence on plastics transport have been identified. Lastly, surge wave dynamics and transport observed in nature owing to surge waves is discussed.
- Chapter 2: presents the experimental methodology used for investigating the transport of macro-sized debris in breaking surge waves. Several add-on and

modifications made to the flume are reported. Moreover, initial flow conditions and analytical solution used to develop the initial flow condition are presented. Lastly, the post processing methods and software used for particle tracking are described.

- Chapter 3: discusses the flow parameters and the variation in experimental and theoretical variables. Initially, the air entrainment and mixing layer induced in surge waves are described, and observations are linked to the literature. Furthermore, the results of negatively buoyant macroplastics are presented, where the initial observation, impact of surge wave Froude number, and impact of particle size are examined.
- Chapter 4: addresses the initial observations for positively buoyant macroplastics, followed by the influence on macroplastics transport mechanism due to surge wave Froude number, and the impact of macroplastic size is compared.
- Chapter 5: concludes the experimental findings on the transport of plastic debris in surge waves and provides a future recommendation based on the present method.

Chapter 2 – Methodology

The methodology chapter has five sections: experimental setup (Section 2.1), analytical solution (Section 2.2), initial flow conditions (Section 2.3), post processing of the experimental results (Section 2.4), and analyzing the results using a PTV program (Section 2.5).

2.1 Experimental Setup

Experiments were performed using GUNT HM 162 experimental hydraulic flume. In the laboratory, surge waves are generated by sudden removal/closure of a sluice gate. The flow was interrupted with immediate gate closure to generate a positive, stable breaking surge wave advancing towards the upstream of the channel, as demonstrated in Figure 1-3. To conduct this experiment, GUNT HM 162 experimental hydraulic flume with dimensions of 5000 mm by 309 mm by 450 mm was used (Figure 2-1). The experimental GUNT HM 162 flume designed for teaching and research was equipped with control structures, flow regulation, and various flow measurement techniques. The flume's smooth inlet transition structure is designed to minimize turbulence when the flow enters the experimental unit. In addition, the channel bed is made from smooth galvanized steel to further reduce turbulence. The hydraulic flume can be inclined in small increments with a touch of a button, producing a uniform flow with constant discharge and water depth. Numerous adds-on are available for research and teaching purposes. For example, piers, a wave generator, sediment feeder, radial gate, and a wide range of weirs and spillways structures. The flume can be modified for several flow measuring instruments. Such as level gauge, velocity meter, electronic pressure measurement, particle image velocimetry (PIV), ten tube manometers, and pitostastic tube. The side walls of the flume are made from tempered glass for flow observation. The flowrate, sediment injection pump, wave generator, and bed inclination are controlled by a digital board powered by a programmable logic controller system.

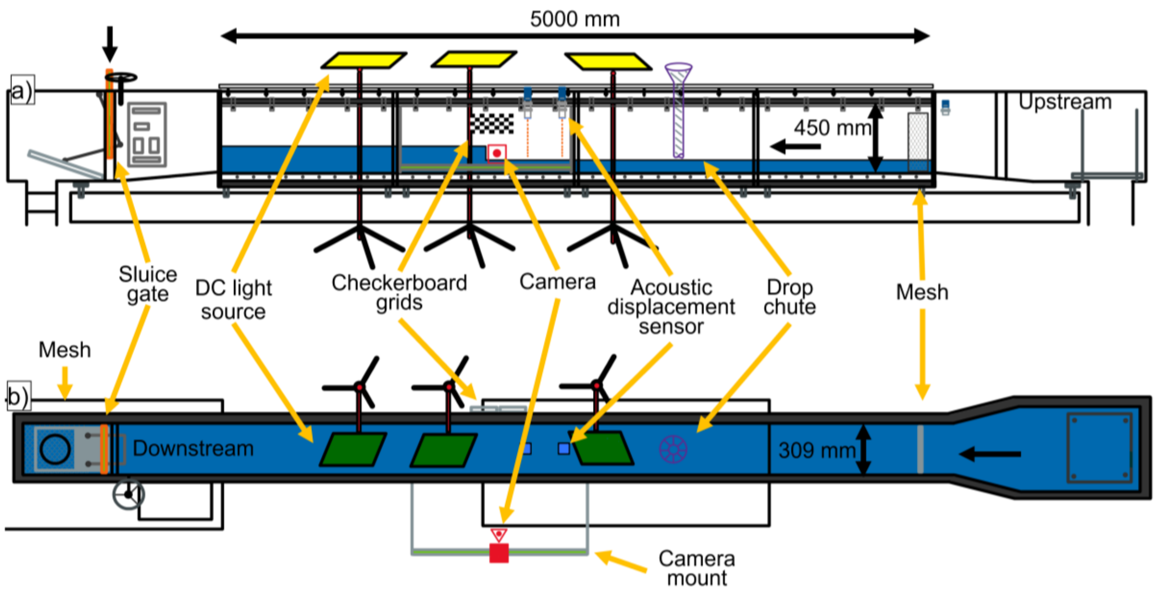

Figure 2-1. Schematic of experimental setup showing: a) side observation panels and b) top view of the GUNT flume.

2.1.1 Plastics particles

Macroplastics were initially transported downstream with the upstream velocity, starting at the drop chute (see Figure 2-1) while the surge wave advanced in upstream direction with the surge wave celerity. Plastics particles introduced into the surge wave were chosen based on 1) their abundance in the marine environment, and 2) their density to ensure sufficient entrainment. For this study, three different plastic polymers were selected: HDPE, PP, and ACR. The positively buoyant HDPE and PP plastics were selected since they are predominant in marine environment, as reviewed in section 1.2.4. Moreover, ACR was considered to mimic plastics present in nature which are heavier than the density of ambient water. In addition, lower Stokes number ensures higher entrainment (Shamskhany et al., 2021), and smaller Stokes number can be obtained by reducing particle size or by decreasing the density difference between the particle and the ambient fluid. Therefore PP, HDPE, and ACR solid plastic balls (referred to hereafter as macroplastics) were selected since their density is marginally lower and higher than the density of ambient water (Table 2-1). This increases the entrainment of these macroplastics in a surge wave.

Table 2-1. Properties of macroplastics used in this study.

Polymer	Diameter (cm)	Min density (g/cm^3)	Max density (g/cm^3)
PP	2.54, 1.91, 1.11	0.90	0.93
HDPE	2.54, 1.91, 1.11	0.94	0.97
ACR	2.54, 1.91, 1.11	1.17	1.20

2.1.2 Sluice gate

A 1.27 cm thick acrylic sheet (60.96 cm by 30.48 cm) was used as a sluice gate. To minimize the outflow after the gate was lowered, a rubber seal was applied on one side of the gate (Figure 2-2). Applying a rubber seal around the perimeter of the entire acrylic sheet can further minimize the outflow. However, this increased the closure time due to the increased friction between the gate and the flume wall. The flume was equipped with a tilting weir gate, which provided complete closure. However, due to the force of the incoming flow, closure time with the existing tilting weir gate took a few seconds. Since the rapid gate closure time must be less than 0.20 s to ensure rapid closure (Chanson, 2010a, 2010b, 2011), a drop sluice gate was designed to work with the existing setup. The sluice gate was lowered on a rubber plate that was present at the downstream side of the channel bed to achieve a nearly zero outflow (Figure 2-2), while maintaining the closure time of less than 0.20 s.

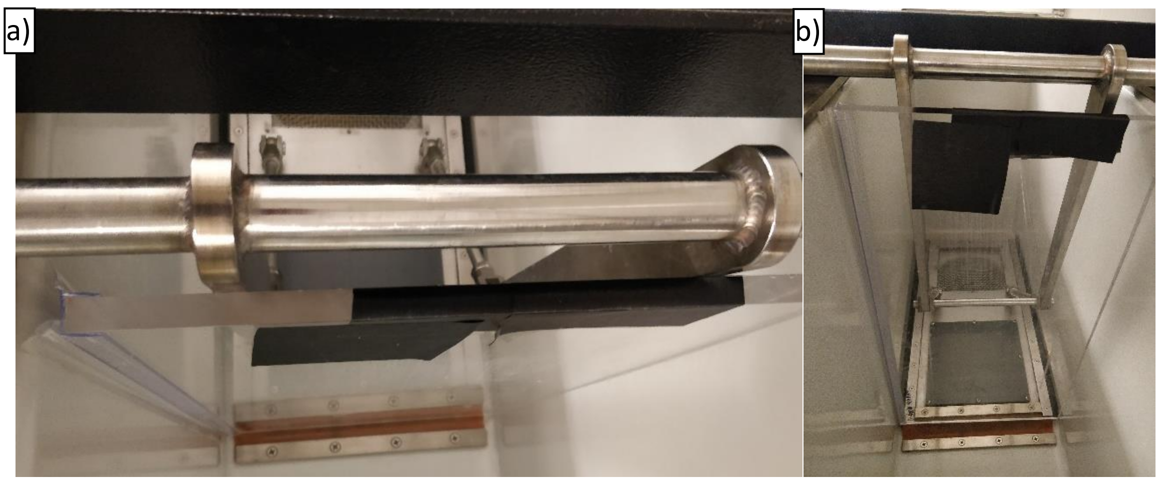

Figure 2-2. The picture shows a) top view and b) front view of the tilting weir gate at the downstream of the flume. The sluice gate was lowered on the orange rubber gasket.

2.1.3 Mesh

A mesh was required at both the inlet and outlet area, to prevent the macroplastics from seeping into the inner system of the flume and damaging the pump. A stainless-steel mesh was placed right above the outlet opening while at the inlet, a vertical mesh was installed (Figure 2-3).

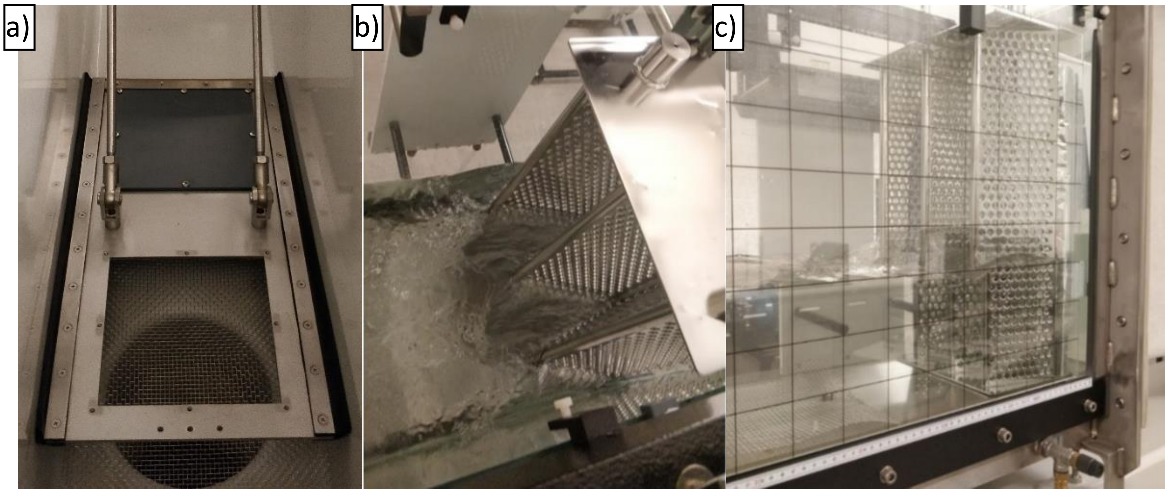

Figure 2-3. Mesh secured near: a) the outlet and, b) & c) the inlet of the channel.

2.1.4 Drop chute

Originally macroplastics were dropped into the flume from a height of nearly half a meter. This added unnecessary momentum to the macroplastics, which extended the transport of the macroplastics in the vertical direction due to experimental errors. Additionally, macroplastics were observed to deviate from the center of the flume. This may alter the entrainment mechanism due to the initial momentum generated by the free fall of the macroplastics. To minimize the impact of initial momentum, a drop chute was designed to ensure macroplastics were always released in the center (Figure 2-4 a) and right above the water surface to reduce the potential energy when macroplastics are released (Figure 2-4 b). The chute was mounted on top of flume and the height was regularly adjusted to accommodate varying upstream water depth (Figure 2-4 c).

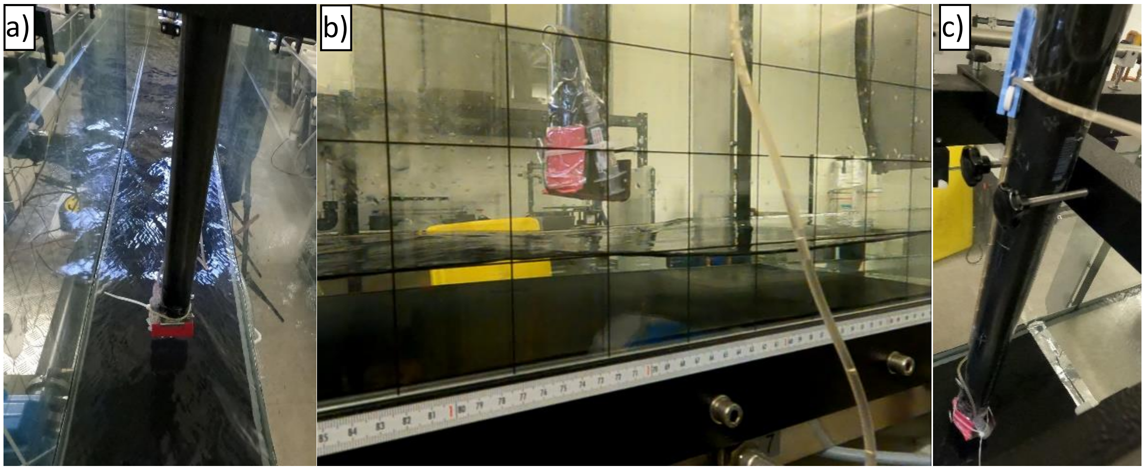

Figure 2-4. Drop chute installed in the center, near the inlet of the channel: a) drop chute, b) chute release mechanism, and c) chute mount.

2.1.5 *Flume bed*

The flume is equipped with a galvanized steel bed (Figure 2-5 a). This reflective material introduces glare in the camera and prevents the PTV program from detecting macroplastics. Therefore, an anti-reflective material was required to cover the reflective flume bed. The anti-reflective sheet was cut to fit into the width of the channel. Furthermore, the material’s surface roughness was smooth and did not affect the flow or the propagation of the surge wave. While having the strength to grip onto the flume bed and remain stationary during surge propagation. A black magnetic sheet with a thickness of 0.76 mm (3048mm by 304.8mm) was placed on the flume bed to reduce reflection, as seen in Figure 2-5b. However, preliminary testing showed that the sheet was sliding towards the downstream in surge waves with higher Froude number. Therefore, the sheet was fixed to the flume bed with tape which solved this problem.

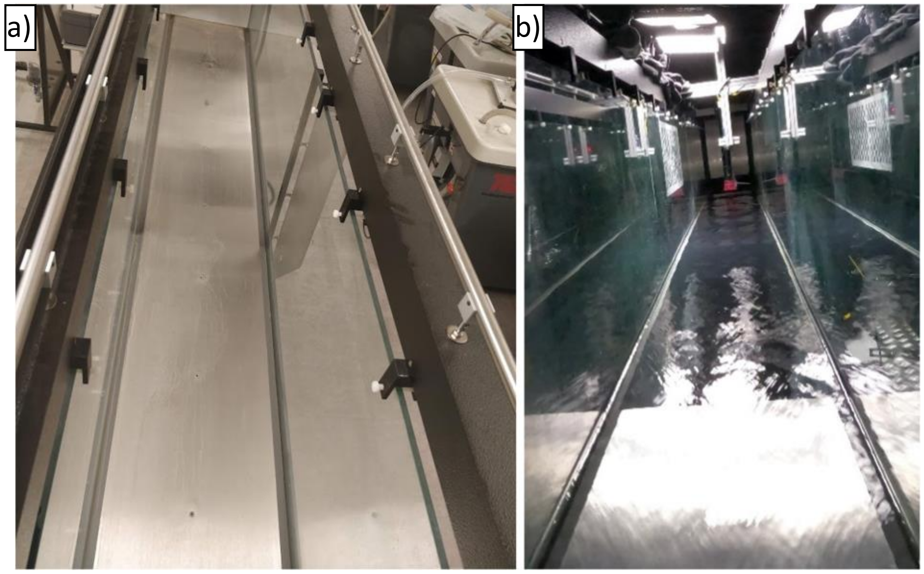

Figure 2-5. Photographs of the flume bed: a) without any anti-reflective solution (looking downstream) and b) showing the difference between galvanized bed and anti-reflective sheet (looking upstream).

2.1.6 Camera

There were several issues that had to be managed to ensure proper capture of the particles by the camera and the particle tracking software. After the sluice gate is dropped, the breaking surge wave advances towards the upstream and reaches the inlet within a few seconds. A high frame rate and high-resolution camera was required to capture greater details for analyzing the transport of macroplastics in a breaking surge wave. GoPro HERO 9 camera was utilized for capturing the transport process at a resolution of 2704 by 1520 at frame rate of 120 frames per seconds. A higher frame rate of 240 frames per seconds was possible with the current camera, however, that decreases the resolution. To ensure the recording can be repeated, a rail mount was designed to hold the camera (Figure 2-6a) which also made camera mounting easier and offered flexibility in camera calibration and leveling. The camera was secured on top of the railing mount at the third viewing panel from the inlet, which was the interrogation area (Figure 2-6b). Slight movement of the camera required leveling and calibration. Therefore, the camera was triggered using a wireless remote to minimize all physical contact with the camera.

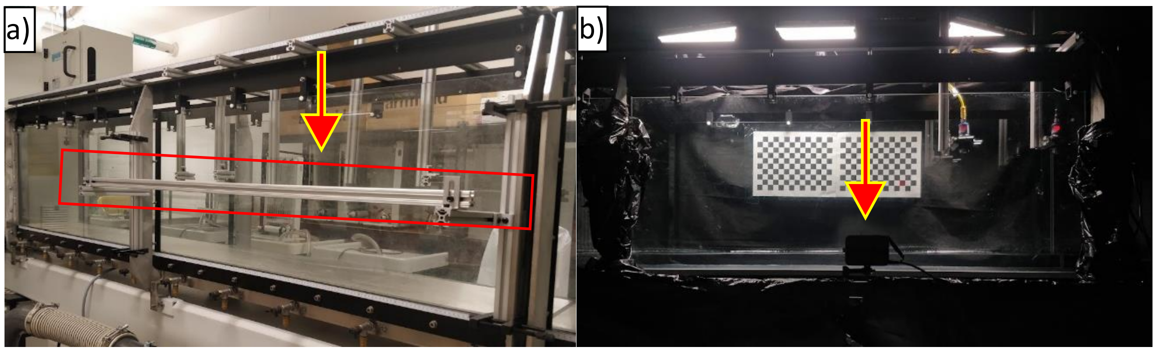

Figure 2-6. Experimental setup: a) showing the rail mount fixed on the third observation panel from inlet and b) the position of the GoPro camera.

The rail mount introduced glare in the camera, and partially prevented the PTV program from detecting macroplastics, similar to the reflection of the flume bed (Section 2.1.5). The simple solution was to cover the entire rail mount with black plastic sheets (Figure 2-6b). Furthermore, to prevent PTV program from tracking outliers, a black photography studio backdrop was added to the rear of the flume, shown in (Figure 2-6b).

All rooms run on an AC electrical system which results in the room lights flickering at a frequency of 120 Hz (double the electrical grid frequency of 60 Hz). As such, the room lights were interfering with recording that was conducted at 120 frames per second or higher and prevented the PTV program from identifying the particles. Therefore, the conventional AC lights were turned off, and three portable DC (direct current) light sources were adapted to prevent flickering (lighting setup is shown in Figure 2-7).

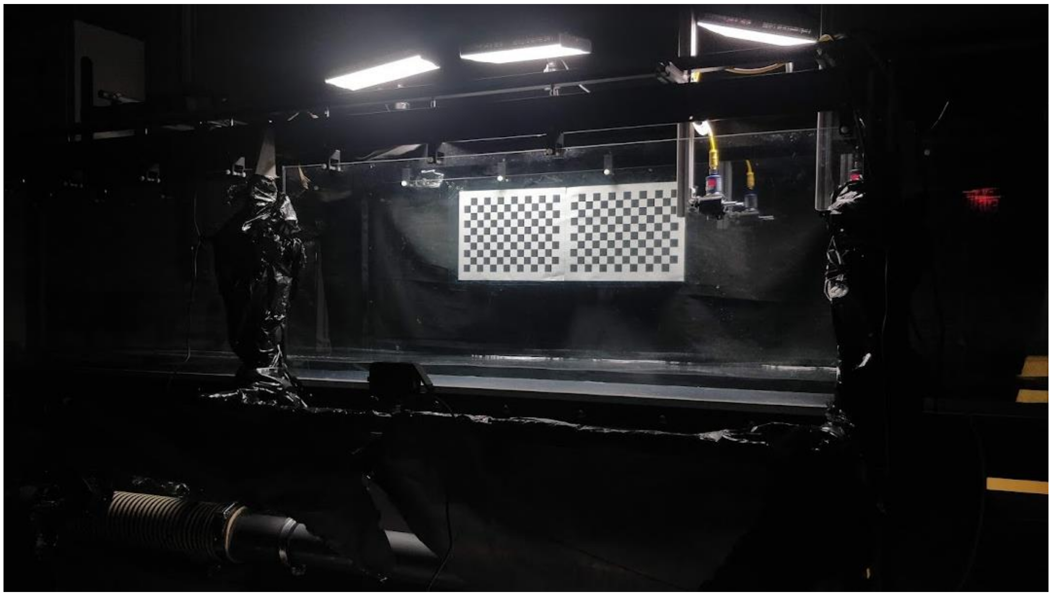

Figure 2-7. Portable DC lights luminating the interrogation area.

Lastly, the lighting in the laboratory was kept at a minimal level to reduce glare experienced by the camera. However, this hindered PTV program from continuously following the particle. Initially, all macroplastics were painted with a bright colour (e.g. red, orange, green, and yellow). However, the PTV program still had difficulty with tracking these particles. Particles were then painted with neon glow in the dark paint, and the PTV program was able to track the particles while keeping the light low to minimize glare.

2.1.7 Water depth measurement

Flowrate and upstream water depth are required to determine upstream velocity and surge celerity. Flowrate was obtained from hydraulic flume's control panel, while the upstream water depth was measured using two microsonic mic+35/IU/TC acoustic displacement sensors (Figure 2-8a). These sensors were chosen since the upstream water depth should be measured very accurately as this variable can alter other variables. These sensors had a blind zone of 0 to 65 mm, and operating range of 350 mm, with a maximum range of 600 mm. The ideal operating range was between 65 mm to 350 mm. Acoustic displacement sensors were secured on a flexible mount, which enables easy adjustment to ensure recording was always performed in the operating range (Figure 2-8b). In addition, these sensors had a response time of 64 ms, which equates to roughly 15 Hz. Therefore, the water depth measurements were conducted at a frequency of 15 Hz. Acoustic displacement sensors were mounted 26.5 cm apart, and 64 cm for low surge wave Froude number experiment. Sensors were powered with Keysight E3630A triple output DC power supply unit; which were linked to the Catman data acquisition & analysis program, with the use of HBM QuantumX MX840B, to digitalize water depth measurements. Every time there was a change in particle size or polymer type, the water depth readings were set to zero. Assigning measurement frequency and executing zero balance on all the sensors were performed using Catman data acquisition software.

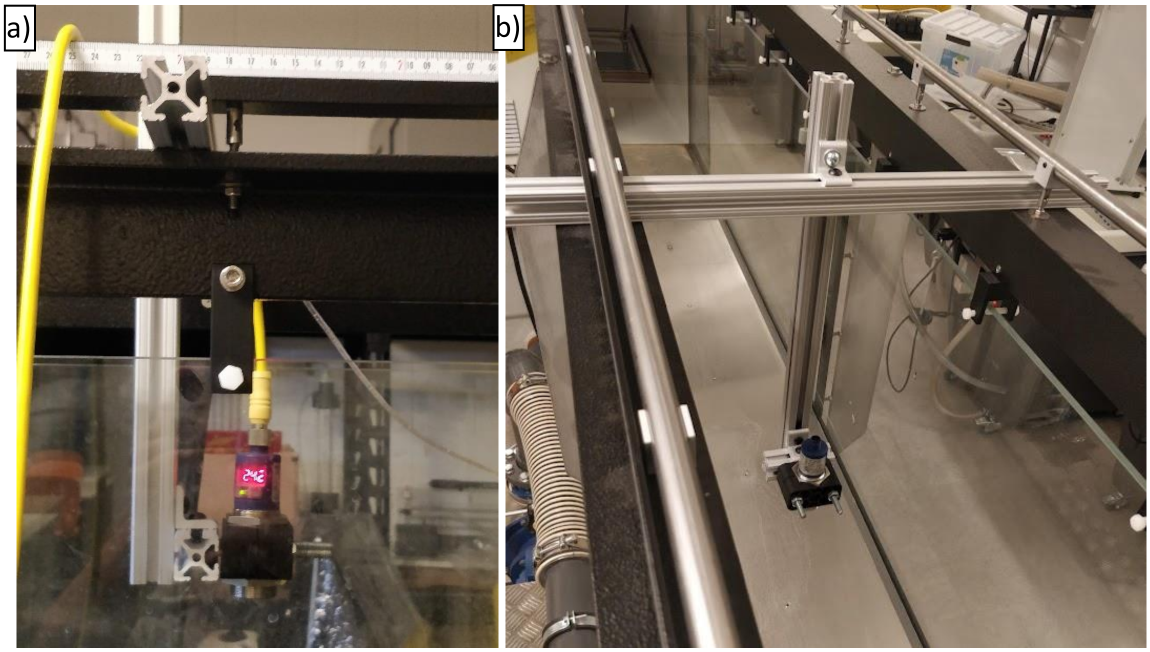

Figure 2-8. Setup of: a) an acoustic displacement sensor reading water depth and, b) sensor secured on an adjustable mount (looking downstream).

2.2 Analytical solution

The analytical solution for the surge wave Froude number is derived based on a surge wave reflecting off a closure, in this case a sluice gate. Analytical solution was used to determine initial flow conditions. Frictional effects are generally neglected to simplify the analysis. Consider a positive surge wave advancing upstream, observed by a spectator traveling at surge celerity, c, where the upstream velocity, u_1, is $(u_1 + c)$, and downstream velocity, u_2, is $(u_2 + c)$.

Parameters used in the analytical solutions are presented in Figure 1-3, where d_1 is the upstream water depth, obstructed by rapid sluice gate closure, producing a positive surge wave propagating upstream with celerity, c, and downstream water depth, d_2. Downstream velocity, u_2, is nearly zero due to complete closure.

Considering the following continuity equation in a moving frame of reference, with a unit water depth (Eq. 2-1).

$$d_1(u_1 + c) = d_2(u_2 + c) \quad \text{Eq. 2-1.}$$

Unit flow, q, is a product of upstream velocity and upstream water depth $q = u_1 d_1$. This relation is used to derive the analytical solution for celerity (Eq. 2-2).

$$c = \frac{q}{d_2 - d_1} \quad \text{Eq. 2-2.}$$

Considering the momentum equation below in a moving frame of reference, to derive the analytical solution for downstream water depth (Eq. 2-3).

$$\frac{1}{2}d_1^2 - \frac{1}{2}d_2^2 = \frac{c^2 d_2^2}{g} - \frac{(u_1 + c)^2 d_1}{g} \quad \text{Eq. 2-3.}$$

Substituting Eq. 2-2 in the momentum equation above (Eq. 2-3) to solve for analytical unit flow (Eq. 2-4).

$$q^2 = \frac{1}{2}\frac{g}{d_2}(d_2 + d_1)d_1(d_2 - d_1)^2 \quad \text{Eq. 2-4.}$$

Theoretical downstream water depth can be calculated by solving the formulation above. Surge wave Froude number below (Eq. 2-5) was obtained by replacing celerity and upstream velocity with Eq. 2-2 and q/u_1, respectively, in Eq. 1-3.

$$Fr_s^2 = \frac{1}{2}\frac{d_2}{d_1}\left(\frac{d_2}{d_1} + 1\right) \quad \text{Eq. 2-5.}$$

2.3 Initial flow conditions

Surge waves with various surge wave Froude numbers were generated to explore the transport of the macroplastics. Upstream water depth had to be controlled to achieve a surge wave with a specific surge Froude number, this includes bed inclination and raising the tilting weir gate. Hydraulic flume with zero bed inclination and without the use of tilting weir gate to build upstream water depth, generated a surge wave with Fr_S of approximately 1.70. To explore the transport of macroplastics, surge waves with a wide range of surge wave Froude number were required. The preferred range for Fr_S was 1.40 to 2.60 (with an increment of 0.30), since this range covered undular surge waves, undular to breaking surge waves, and breaking surge waves. To produce surge waves with Fr_S of less than 1.70, upstream water depth was increased by partially raising the tilting weir gate (tilting weir gate shown in Figure 2-2). While the flume bed was raised from -0.5% to +2.5%; to generate a surge wave with Fr_S of greater than 1.70. Detailed flume bed inclination, tilting weir gate height, and flowrate for each Fr_S are reported in Table 2-2 and

Table 2-3.

Iterations were performed to determine initial flow conditions for lower surge wave Froude number. After assigning flowrate and bed angle, tilting weir gate was raised in 1 cm increments. Once water depth was stabilized, water depth readings for the last 4.00 s (corresponding to the time where water depth did not change) were obtained from both the acoustic displacement sensors. Lastly, analytical solutions were used to determine downstream water depth, celerity, and Fr_S. Iterations were continued until a desired Fr_S of approximately 1.40 was achieved (reported in Table 2-2).

Similar iterations were carried out to obtain initial flow conditions of higher surge wave Froude number. Once flowrate was set, flume bed was raised in 0.05% to 0.1% increments. After water depth had stabilized, analytical solution was used to determine downstream water depth, celerity, and Fr_S. Iterations were performed until initial flow conditions for all the higher required Fr_S were documented (reported in Table 2-2).

Table 2-2. Initial flow conditions determined by the method of characteristics (MOC). This method is described in section 2.2.

	Flowrate, Q	d_1	u_1	d_2	c	Fr_S

Analytical condition	(m^3/hr)	(m^3/s)	(cm)	(cm/s)	(cm)	(cm/s)	
MOC-1	50	0.014	9.80	45.87	14.76	84.98	1.33
MOC-2	30	0.008	4.66	57.86	9.25	54.16	1.66
MOC-3	60	0.017	5.89	91.60	14.33	61.02	2.01
MOC-4	55	0.015	4.95	99.84	13.53	61.27	2.31
MOC-5	60	0.017	4.50	119.99	14.50	61.34	2.65
MOC-6	65	0.018	4.22	138.42	15.56	61.46	3.11

Table 2-3. Summary of experimental flow conditions and the required bed angle to obtain desired flow condition.

Experimental condition	Bed angle		Sensor height difference (mm)	Flowrate, Q		d_1 (cm)	u_1 (cm/s)	d_2 (cm)	c (cm/s)	Fr_s
	(%)	(°)		(m^3/hr)	(m^3/s)					
MOC-1	0	0	0	50	0.014	9.25 – 9.90	45.52 – 48.58	13.61 – 14.57	80.00 – 91.43	1.33 – 1.44
MOC-2	0	0	0	30	0.008	4.66 – 5.11	52.82 – 57.87	8.31 – 9.13	53.00 – 66.25	1.55 – 1.78
MOC-3	0.10	0.06	0.26	60	0.017	5.84 – 6.12	88.12 – 92.32	14.23 – 14.5	53.00 – 66.25	1.84 – 2.08
MOC-4	0.4	0.23	1.04	55	0.015	4.68 – 4.95	99.85 – 105.55	13.21 – 13.5	53.00 – 66.25	2.20 – 2.47
MOC-5	0.85	0.45	2.10	60	0.017	4.41 – 4.55	118.53 – 22.44	13.99 – 14.39	53.00 – 66.25	2.57 – 2.79
MOC-6	1.70	0.77	3.60	65	0.018	4.15 - 4.25	137.6 - 140.63	15.38 - 16.72	40.77 - 66.25	2.81 - 3.22

2.4 Post Processing

The video data obtained from experiments were in a MP4 video format. Frames were extracted from every video file. After extracting all the frames, a check was performed to ensure no frames were missing. For example, each experiment usually lasts roughly 5 s, since the recording was performed at 120 frames per seconds, the 5 s long video would yield approximately 600 frames.

There are two distinct types of distortions in photography: perspective distortion and optical distortion. Perspective distortion renders the object which significantly differs from what it would look like to a human eye and is a function of the distance from the camera to the subject and viewing angle. This type of distortion was reduced by having a sufficient distance between the camera and the object (interrogation area), and by positioning the camera in line with the interrogation area (perpendicular to the horizon line). Optical distortion is a result of lens design and lens profile, hence also referred as lens distortion. Almost all lenses introduce a certain level of optical distortion. As a result of the wide-angle lens used, minor barrel optical distortion (fisheye effect) was observed in the data (Figure 2-9a). Although the distortion was minor, it can still produce inaccurate particle velocities and trajectories, due to the inaccurate pixel per centimeter ratio. Therefore, this minor distortion was addressed in post-processing. Photoshop, the industry standard for graphic manipulation and editing, was used for correcting optical distortion (Figure 2-9b). A 2 cm checkerboard grid was added to the rear of the flume, allowing the grid to be visible by the camera. This calibration grid, along with the measurement marking on the flume was used as a reference for correcting distortion during post processing, (Figure 2-9b). Frames were rotated and leveled in post processing, along with distortion correction. Every time data had to be extracted, the camera was removed from the mount; this required readjustment in rotation and geometric distortion during post processing.

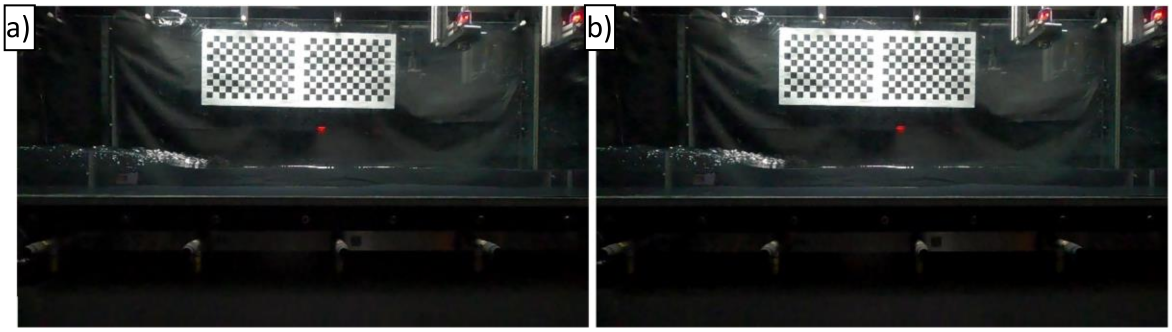

Figure 2-9. An example of optical distortion correction for a test run with a Fr_s = 1.70. a) original frame and b) frame rotated and corrected for optical distortion.

2.5 Particle Tracking Velocimetry

2.5.1 Introduction to flow visualization and measurement

Turbulent flow can be observed in daily life, both in urban and natural settings. Comprehending turbulence in water and air was partially responsible for allowing shipping vessels to travel through oceans with hundreds of thousands of tonnes and airplanes to fly at greater speeds and higher altitude. This concept has also contributed to understanding the human body. For example, in mild stenosis, which restricts blood flow out of the heart, turbulent kinetic energy is substantial, and turbulent viscosity is greater (Banks & Bressloff, 2007), thus increasing the energy required for blood flow. Turbulent flow through a prosthetic heart valve increases the stresses on cells (Quinlan & Dooley, 2007). Understanding the fundamentals of turbulence has been beneficial for the advancement of our society. This can be done through accurate measurement and visualization of turbulence. In early fluid dynamics, qualitative flow measurements were performed, and flow visualization dates back to as early as the 1400s (Gharib et al., 2002). Quantitative flow measurements were later possible with techniques such as point measurement, with pressure pitot tubes, vane anemometers, and laser Doppler velocimetry (Smith & Neal, 2016). Advancement in technology has opened doors for measurements and flow visualization using optical methods. Particle image velocimetry (PIV), developed in the 1970s, uses an optical measurement method to determine the velocity field of a flow region. This system employs a non-intrusive measurement method for determining the velocity field, which has an advantage over point measurement probes which are intrusive. In addition, PIV can be used for both flow measurements and 3D flow field visualization.

2.5.2 Tracker

Tracker, a 2D open-source particle tracking velocimetry platform developed by the Multiphase Flow Science at US Department of Energy, National Energy Technology Laboratory (2019a), was used for identifying and tracking the macroplastics. This continuously developed, tested, and verified PTV program was written in Python for tracking objects across a stack of images and videos (Weber et al., 2019). It uses tools such as SciPy, matplotlib, and numpy from Python libraries to identify the particles, and it utilizes opencv image processing for reading media (video and image) files (Weber et al., 2019).

Tracker is also equipped with image pre-processing where basic image manipulation can be performed, such as frame rotation and cropping. There are three background subtraction methods in Tracker: mean background subtraction provided by numpy, MOG2 and KNN, both of which are powered by opencv (US Department of Energy, National Energy Technology Laboratory, 2019b). The fundamental concept for detecting an object in motion is to take the difference between the current frame and the reference frame. The initial image, frame$_{i}$, is set to background, and the background is then subtracted from the next image in the sequence, frame$_{i+1}$. The foreground is obtained by applying a threshold to absolute difference. The pixel in frame$_{i+1}$ is identified as a background point when the absolute value (difference in colour intensity) of a pixel is less than the set threshold value (Chiu et al., 2018). The pixel value will be a foreground point if the difference is greater than the threshold (Chiu et al., 2018). The mean subtraction methods work in a similar manner, in which an array of images is built and updated, with the frames provided. This method takes an average of all the pixel values from the frames provided, and how many frames from the given frames to use for determining the moving mean for each pixel can be specified. In this array, each pixel value equates to the mean of all the pixels from a specific (x, y) coordinate across all the frames, and this moving mean is updated. The moving mean value exists for each pixel location throughout the entire image, and that moving mean pixel value is used as a background. This background value, similar to frame$_{i}$, is used as a reference (Figure 2-10 b), and the background is then subtracted from every image in the sequence, similar to frame$_{i+1}$, while the moving mean is constantly being updated (Figure 2-10 c). The difference in subtraction results in a foreground point and using that information a foreground image is created (Figure 2-10 d).

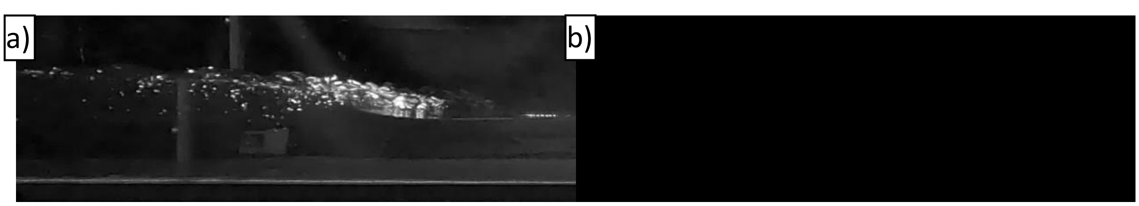

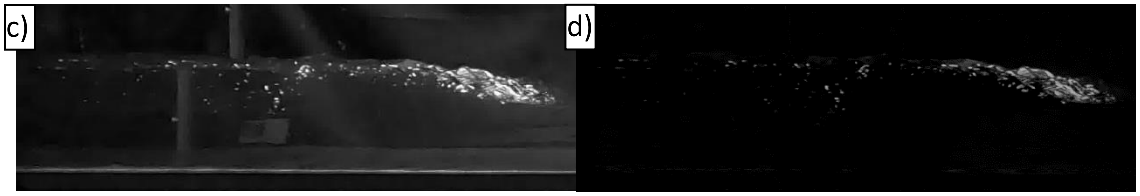

Figure 2-10. Mean background subtraction: a) surge wave in the initial frame (t = 0 s), b) initial frames used as background frame (t = 0 s), c) surge wave in the 30th frame (t = 0.25 s), and d) advancing surge wave detected as foreground in the 30th frame (t = 0.25 s).

Background subtraction was used to enhance the tracking process. Further tracking techniques were required for detecting the particle. Tracker offers three distinct particle detection methods: hough circles, label detection, and simple blob detection (US Department of Energy, National Energy Technology Laboratory, 2019b). Hough circles identifies circular objects in an image file, which would be perfect for the spherical macroplastics used in this experiment. However, hough circles is sensitive and requires the object to be fairly uniform, and with air entrainment present in the experiments the macroplastics will not appear uniform in the image (US Department of Energy, National, Energy Technology Laboratory, 2019b). Label object detection filter was not used to detect the macroplastics since this method offered no control for particle detection threshold. Therefore, simple blob detection was used for detecting the macroplastics in an image. A "blob" is a cluster of pixels in an image which have similar properties. This method identifies the center of all the blobs which differ from the surrounding region. Properties of a blob can be defined for optimal tracking. A range of area occupied by the particle, blob threshold, circularity, convexity, and inertia can also be altered; visual representation of these properties can be seen in Figure 2-11. Firstly, filter by blob area is based on the area where the area is determined based on macroplastics diameter (D = 2.54, 1.91, or 1.11 cm). Once the area for the macroplastics is calculated, an upper and a lower range of area occupied by the particle is defined, this is referred to as the blob area threshold. This is in terms of units of pixels, instead of a physical unit of measurement. Furthermore, blob colour is set based on how bright an object appears, in this case a macroplastic, with a grayscale value of 0 representing a complete black and 255 complete white. There may be a change in macroplastic's colour intensity when the particle goes from surface level to underwater during the entrainment in the surge wave. This filter requires fine tuning, and the range may differ in each test run. The next three parameters, blob circularity, inertia, and convexity, are used for describing a shape of a particle. Blob circularity is also a parameter for controlling particle shape. This variable measures how close a particle is to a circle, with 1 signifying max circularity (fully circular) and 0 describing minimum circularity (Mallick, 2015). Since macroplastics are fully circular, the range selected for circularity was kept very small to minimize outliers. In addition, blob inertia is also a parameter for measuring a shape of a particle, it represents how elongated a shape is, with 0 exhibiting an elongated shape and 1 denoting a circular shape (Mallick, 2015). The range specified for this variable was also small, however, some cases required a wider range. At last, convexity is also a parameter for shape, with 0 indicating minimum convexity and 1 representing maximum convexity (Mallick, 2015). Unlike previous parameters for shapes, this variable required a much wider range since macroplastics were constantly being covered by air entrainment.

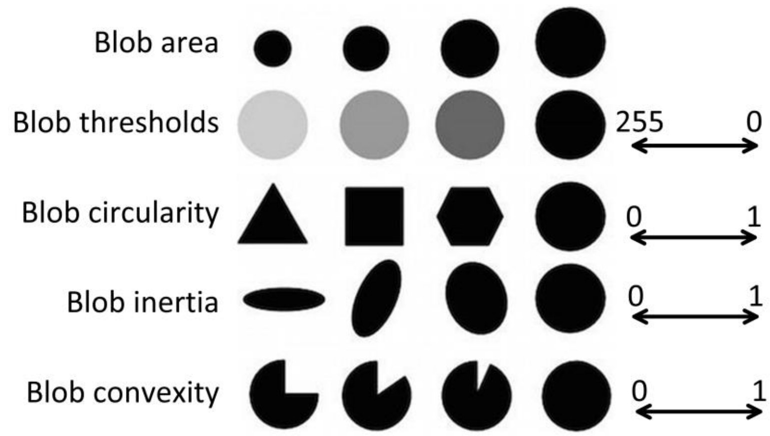

Figure 2-11. Simple explanation of simple blob detection using OpenCV (Mallick, 2015).

In the object detection process, particles were detected in multiple frames. However, the PTV platform, up to this process, was unable to find that same particle in a sequence of frames. Poly projection tracking technique was used to track particles across successive frames. This method predicts the location of an object, and if the same object is detected in successive frames within the specified tolerance, then the location of that object is documented to form a trajectory of that particle. The poly projection approach is described in Table 2-4.

Table 2-4. Poly projection algorithm for tracker obtained from US Department of Energy, National Energy Technology Laboratory (2019b).

Frame	Particle location	Velocity	Description
i	$(x,y)_i$		Plastic particle is located at (x,y), in frame (i).

$i+1$	$(x,y)_{\mathrm{i+1}}$	$v(i)$	That same plastic particle is located at (x,y) in frame $(i+1)$, within the initial search radius.
$i+2$	$(x,y)_{i+2}$	$v(i+1)$	Particle displacement is calculated based on the difference between $(x,y)_i$ and $(x,y)_{\mathrm{i+1}}$. Time difference between (i) and $(i+1)$ is 1/120 s since the recording was performed at 120 frames per seconds. Using this information, particle velocity, $v(i)$, is calculated. Using particle velocity, the particle location is predicted in the next frame, which is $prediction_{(i+2)} = (x,y)_i * v(i)$. The particle is then located near the projected position within the new search radius, $r_{search(i)} = max(v(i-1) * uncertainty, r_{min})$, where $uncertainty$ is a multiplier to calculate search radius, and r_{min} is the minimum search radius. In this step $r_{search} = v(i) * uncertainty$.
$i+3$	$(x,y)_{i+3}$	$v(i+2)$	Polynomial fit can be obtained at this point. Tracker allows the user to set polynomial degree and number of points to fit.
$i+n$	$(x,y)_{i+n}$	$v(i-1)$	Repeating step $i+3$ until the object is lost within the search radius or all the frames have been processed.

The initial step in the poly projection tracking is to set an initial search radius. The algorithm will try to find that object in the next frame, with the user specific radius tolerance (Figure 2-12). The search radius was typically set to about 5 to 10 times the polymer diameter, but would vary in some cases. The next step in the process was to define uncertainty. This is a multiplier on the velocity, which allows the search radius to fluctuate when there is change in velocity (US Department of Energy, National Energy Technology Laboratory, 2019b). This parameter would vary in each case, depending on the macroplastic's transport process in the surge wave. The last step is to define a minimum search radius, which would prevent the search radius from going to 0 with successive frames. This step also ensures objects are still tracked even if objects come to rest (US Department of Energy, National Energy Technology Laboratory, 2019b).

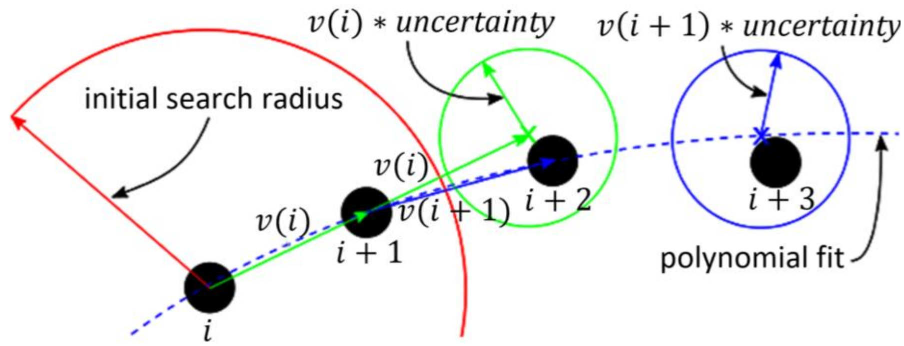

Figure 2-12. Schematic of poly projection method, modified from US Department of Energy, National Energy Technology Laboratory (2019b).

The final step in Tracker was to export object coordinates. Particle trajectories were determined based on pixel to unit cm ratio, and particle velocity was calculated using central differencing approximation (Eq. 2-6).

$$f'(x) \approx \frac{f(x+h) - f(x-h)}{2h} \qquad \text{Eq. 2-6.}$$

Despite controlling various parameters, Tracker occasionally identified several objects and air entrainment as particles, which were manually eliminated. In addition, the Tracker program had difficulty identifying and tracking the particle, when the particle was hidden behind air entrainment. The macroplastic in those frames was manually identified and tracked using ImageJ, developed by (Rasband, 1997). The manually tracked coordinates were exported from ImageJ and merged with the ones obtained from Tracker.

Chapter 3 – Surge Wave Mixing and Dynamics of Negatively Buoyant Macroplastics

In this chapter, the dynamics of surge wave and the transport of negatively buoyant macroplastics (i.e. ACR) are discussed. Firstly, flow parameters are discussed, followed by a brief introduction on air entrainment and the formation of mixing layer in surge waves. Furthermore, the transport of negatively buoyant macroplastics is discussed, which contains initial observations, impact of surge wave Froude number on ACR transport, and impact of macroplastics size.

3.1 Flow parameters

To accurately estimate the surge wave Froude number, flow parameters including flowrate, surge wave celerity, and water depth, were measured. Water depth before, after, and during the passage of the surge wave were measured using acoustic displacement sensors with a frequency of 15 Hz for the duration of the surge passage, between 0.40 to 0.80 s. As seen in Figure 1-3 and Figure 2-8, the displacement sensors are located at the upstream end of the interrogation window. Therefore, as shown in Figure 3-1, the displacement sensor initially reported the upstream water depth of d_1, and with wave passage, it displays, d_2. Displacement sensor $P\#2$ was located further upstream of the interrogation window, and therefore, displayed the passage of the surge wave with a time lag. Turbulent structures and environmental perturbations across the surge wave resulted in water depth fluctuation. Figure 3-1 also shows the analytical solution obtained by the Method of

Characteristics, as described by Eq. 2-1 to Eq. 2-5 in section 2.2. A sample progression of macroplastics in a surge wave is shown in Figure 3-2, and its position to the surge wave is depicted in Figure 3-1. The t_0 and t_1 timestamp shows the ACR, HDPE, and PP macroplastics position prior to impacting the surge wave. The timestamp t_2 was the impact point of ACR, HDPE, and PP macroplastic with the surge front. The timestamp t_3 and t_4 shows the ACR transport across the channel bed, and the engagement of HDPE and PP macroplastic in the surge wave roller (Figure 3-2). There were several challenges in reporting position and water depth values. Firstly, identifying the exact position of the surge wave using the profiles obtained from these sensors was challenging because the sensors measure water depth at a fixed location, while the surge wave is in motion. In addition, water depth fluctuation added another degree of difficulty in reporting the Froude number. Therefore, to minimize the variability in upstream and downstream water depth, and the influence of these parameters on the experimental results, an average water depth reading over a few seconds was used. Acoustic displacement sensors recording at 15 Hz reported 15 water depth readings per second. An average of water depth readings reported in the last 4.00 s were considered for the upstream water depth, the difference between water depth obtained from a 4.00 s average verses a 25.00 s average was insignificant. For the downstream water depth, 3.00 s water depth readings were averaged since the surge wave reaches the inlet after 3.00 s. Furthermore, the overall average of those two averaged upstream and downstream water depth readings were considered in the experimental calculations.

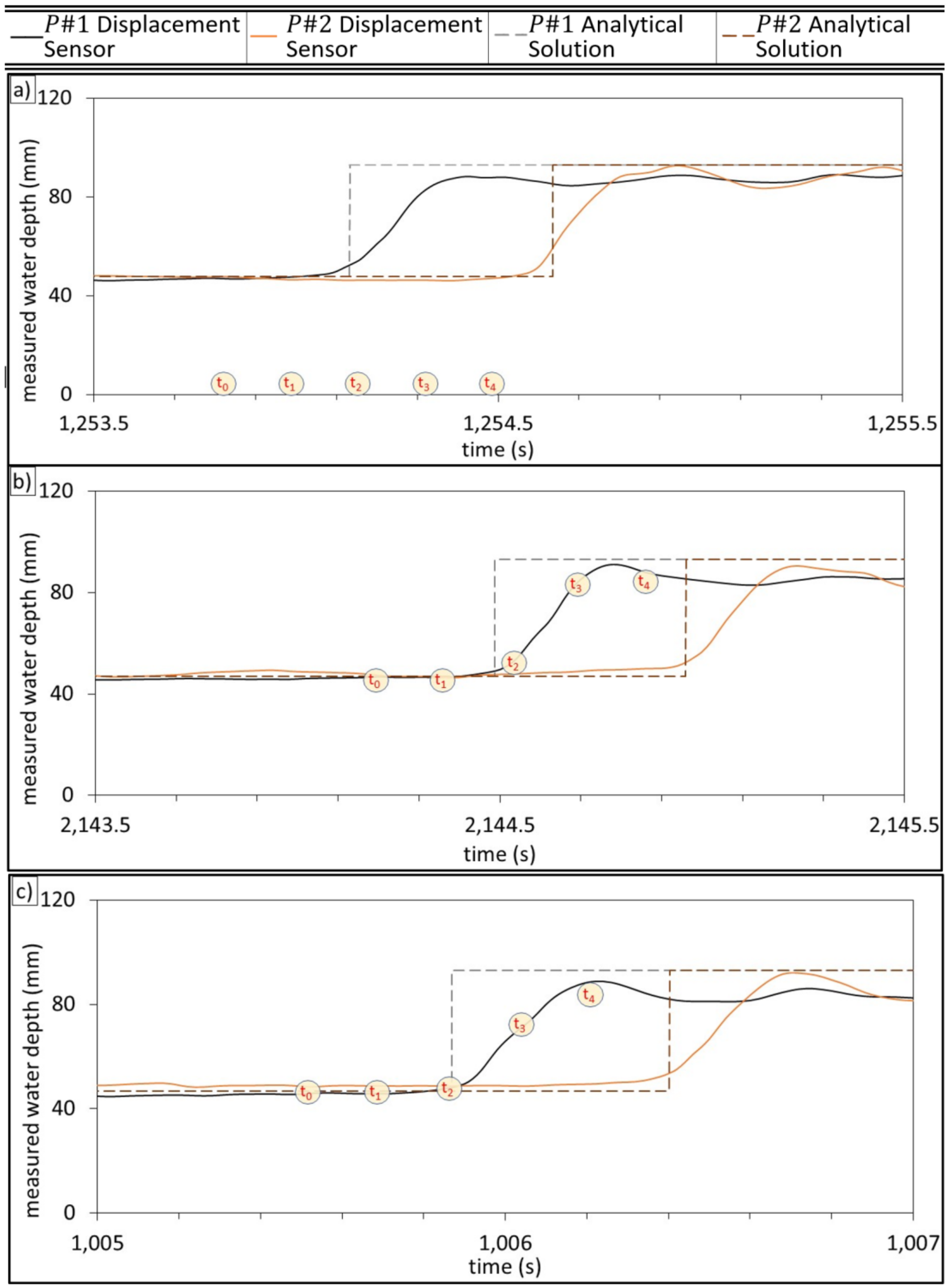

Figure 3-1. Water depth profile reported by two displacement sensors (P#1 and P#2) for: a) ACR, b) HDPE, and c) PP test runs. The experimental surge wave Froude number for ACR, HDPE, and PP experiments in all cases is 1.70.

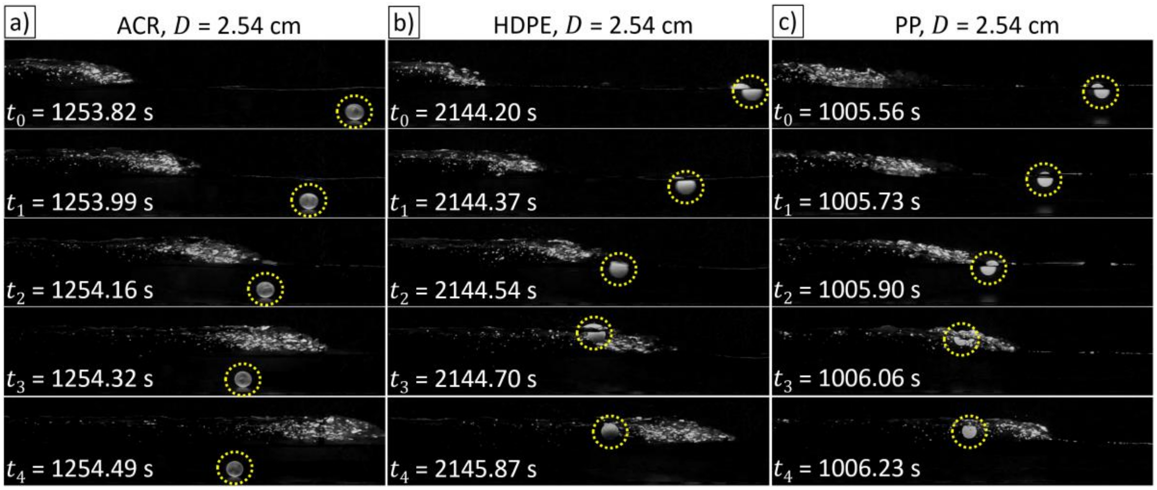

Figure 3-2 Movement of a) ACR, b) HDPE, and c) PP macroplastics in a surge wave, advancing upstream (left to right). Every timestamp represents a progression of 20 frames (0.17 s). Surge is wave advancing upstream (left to right). The positions of the macroplastics in t_0 to t_4 are displayed in Figure 3-1.

Using the averaged upstream water depth and the flowrate obtained from the flume programmable logic controller, upstream velocity was determined. The distance between acoustic displacement sensors and the time lag between the unexpected rise in the water depth due to the arriving surge, was used to calculate the experimental surge celerity, which was used to calculate the upstream water depth, upstream velocity, and experimental surge wave Froude number (Eq. 1-3). The analytical downstream water depth was obtained by rearranging and solving Eq. 2-4. With the available analytical downstream water depth, theoretical surge wave celerity was achieved by solving Eq. 2-2, and the analytical surge wave Froude number was achieved by solving Eq. 1-3, with analytical parameters.

3.2 Air entrainment

Substantial air entrainment occurs at the impingement point (shown in Figure 3-3). Two primary regions exist where the air entertainment is confined: advective diffusion region and breaking region. The breaking of the surface roller advects the aerated flow towards the impingement point (Figure 3-3). The air bubbles are then carried into the advective diffusion region (Takahashi & Ohtsu, 2017), also known as the mixing layer. Vortices with substantial aeration are produced near the impingement point and are advected downstream along the shear layer (Figure 3-3) (Wang & Chanson, 2015). The shear layer is established due to the velocity gradient formed at the toe, between the upstream velocity and downstream advective velocity. The strength of this shearing region depends on the magnitude of the velocity gradient at the toe (Karimpour & Chu, 2016, 2019). Once developed, air entrainment is reported to increase with an increase in the surge wave Froude number (Takahashi & Ohtsu, 2017). The high strength turbulent roller induced at greater surge wave Froude numbers, entraps large amounts of air bubbles. The stronger breaking of the surge wave roller advects large amount of air bubbles to the impingement point, and then the large amount of air bubbles move to the advective diffusion region.

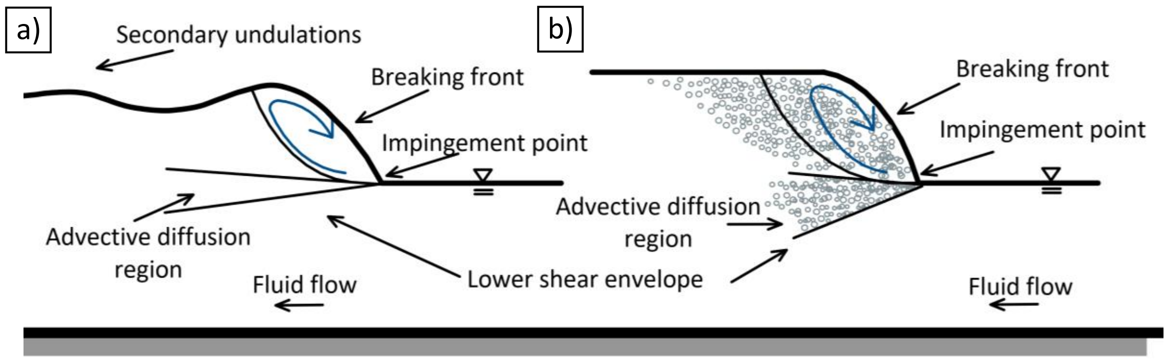

Figure 3-3. Formation of air entrainment in: a) an undular surge wave, and b) a breaking surge wave. Minor breaking front is observed in an undular surge wave when the surge front is at the threshold of undular and breaking surge.

The stronger breaking roller at higher surge wave Froude number, increases air entrainment (Figure 3-4). In addition, the aeration in the flow decreases in the longitudinal direction from the impingement point moving downstream, as shown in Figure 3-4.

3.3 Mixing layer envelope

According to the literature, the mixing layer envelope for an undular surge wave is gradual and the mixing length prolongates longitudinally from the impingement point. Conversely, for a breaking surge wave, the mixing layer envelope is much steeper and diminishes rapidly from the impingement point. Accordingly, as the surge wave Froude number increases, the mixing layer envelope angle increases, and the horizontal extension of the mixing length decreases. This implies that the formation of the mixing envelope and its length was a function of the surge wave Froude number (Figure 3-4). Mixing envelope of an undular surge wave and strong breaking surge wave can be seen in Figure 3-4 (a) and (b) and Figure 3-4 (m) and (n), respectively. The formation of the turbulent breaking front in the surge wave, leads to air entrainment. Air parcels are further mixed in depth by the mixing layer.

As seen in Figure 3-4, with increase in Froude number, the air entrainment increases, confirming the expansion of the lower envelope of the mixing layer. This phenomenon has been reported in the literature by Karimpour & Chu (2019). The developing mixing layer contributes to the generation of large turbulent stresses (Chanson, 2010b) and the formation of the shear layer is induced by the large velocity gradient behind the surge toe. In a undular surge wave, minimum velocities and pressure gradients less than hydrostatic were recorded underneath the wave crests, and maximum velocities and pressure gradients larger than hydrostatic were underneath the wave troughs (Chanson, 2010b). The largest Reynolds stresses and some velocity fluctuations are reported under the leading wave crest and the advancing waves (secondary wave undulations in an undular surge wave) (Chanson, 2011). Consequently, for an undular surge waves, the mixing layer length and the effect of wave undulations extends longitudinally from the impingement point. Conversely, for breaking surge waves, the maximum turbulent stresses are recorded in the vicinity of the roller, where velocity gradients are higher (Chanson, 2011). The longitudinal velocity indicated that the recirculation zone only persists in breaking surge wave (Chanson, 2010b), and the large upstream longitudinal velocities increase, with higher Fr_S.

3.4 Transport of negatively buoyant macroplastics

In this section, the influence of transient recirculation on negatively buoyant ACR macroplastics is explored. The initial and visual observations of ACR macroplastics in a surge wave is investigated in Section 3.4.1. Furthermore, the effect of surge wave Froude numbers on the transport of ACR macroplastics is discussed in the Section 3.4.2. Lastly, ACR macroplastics transport mechanism with varying macroplastic sizes is analyzed in Section 3.4.3.

3.4.1 Initial Observations

As shown in the literature, the strength of the mixing layer and the length of the lower shear envelope is a function of a surge wave Froude number. The ACR macroplastic exhibits a distinct transport mechanism in each surge wave Froude number. The interaction of surge waves and negatively buoyant ACR macroplastics is shown in Figure 3-4. The ACR macroplastics transport in Fr_s = 1.40 to 2.65 were analyzed using PTV software. Experimental setup was limited to surge waves with $Fr_s \leq 2.65$ since the experimental setup hindered PTV program from tracing ACR macroplastics. Therefore, visual analysis and discussion was made for the Fr_s = 2.90 and 4.90, using Figure 3-4 (k) to (n).

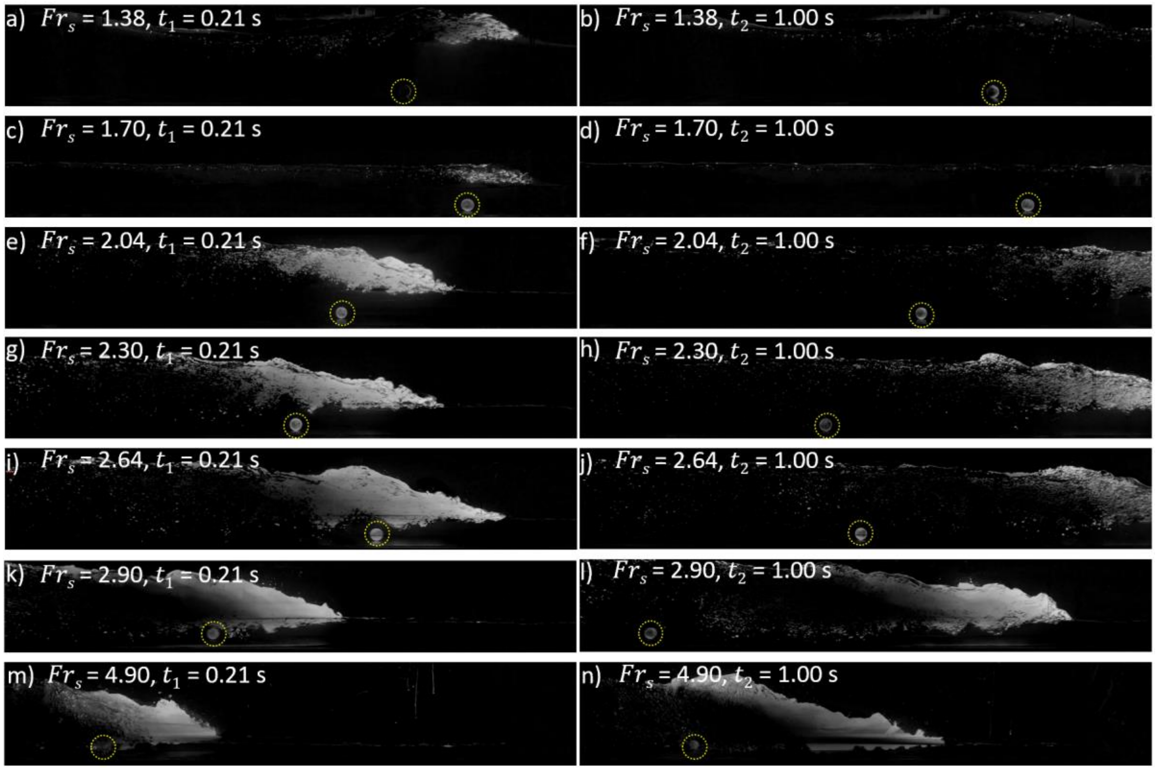

Figure 3-4. Sequence of images showing the influence of a surge wave advancing upstream (left to right) on a D = 2.54 cm ACR macroplastics (highlighted with a yellow marker). The left column and the right column show the position of an ACR macroplastic at 0.21 s and 1.00 s after impacting the surge wave, respectively.

In an undular surge wave (Fr_s = 1.40), and weak breaking surge wave (Fr_s = 1.70 and 2.00), there was little difference observed in the position of the ACR macroplastic 0.21 s and 1.00 s after the impact with the surge wave, as seen in Figure 3-4 (a) to (f). This indicates that there was no downstream motion of ACR macroplastics in undular or weak breaking surge waves. Conversely, in a breaking surge wave with a higher Fr_s = 2.30, 2.64, and 2.90, ACR macroplastics exhibit sustained downstream motion, as shown in Figure 3-4 (g) – (l).

3.4.2 Impact of Fr_s on the 2.54 cm ACR transport mechanism

Turbulent nature of the flow generates water depth fluctuation upstream, across, and downstream of the surge wave. The turbulent structure in a surge wave affects the ACR macroplastics in the streamwise direction and in depth. In this section, to understand the impact of surge waves on ACR particles, focus was initially given to only one macroplastics size, D = 2.54 cm. The velocity of the macroplastic, before its impact with the surge wave, was approximately the upstream velocity. The horizontal transport of ACR macroplastics is shown in Figure 3-5. Particle tracking was halted when the surge wave reached the inlet of the channel; at approximately 3.52 s for undular surge waves (Fr_s = 1.40) and 5.03 s for breaking surge waves (Fr_s = 1.70, 2.00, 2.30, and 2.65). This was done to avoid the effect of wave reflection on the interrogation window.

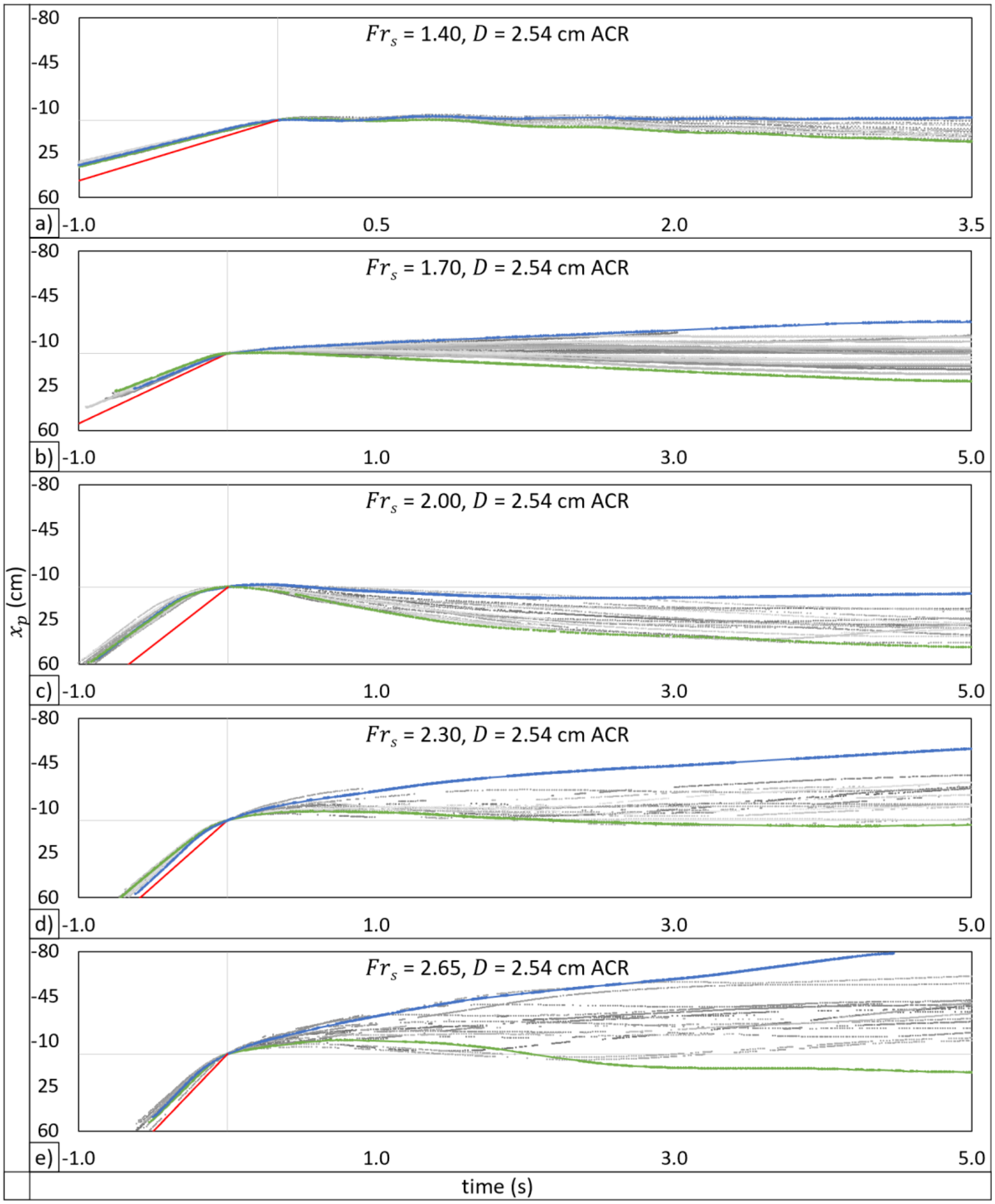

Figure 3-5. Horizontal trajectories of D = 2.54 cm ACR macroplastics. Negative and positive positions in the x-direction (x_p) translate to downstream and upstream movement of the macroplastic, respectively. The minimum and maximum horizontal upstream transport when the surge wave reaches the inlet is depicted by the blue and the green curve, respectively. The red line represents upstream velocity, while the grey curves represent the other 18 experiments.

The ACR macroplastics initial velocities, influenced by the upstream velocity, gradually decelerated after the macroplastics arrived at the surge front, and the macroplastics gradually moved upstream after the passage of the surge wave (Figure 3-5). Despite the weaker developing mixing layer in an undular surge wave, the ACR macroplastics had substantial transport in the horizontal direction, Figure 3-5 (a). After the passage of the undular surge wave roller, the ACR macroplastics started to deaccelerate and came to a halt. The ACR macroplastics then started propagating upstream and came to a halt after the effect of the surge wave roller was lessened. Furthermore, the ACR macroplastics started to move upstream as the secondary undulation waves arrived, (secondary undulations shown in Figure 3-3). As the effect of the secondary wave was reduced, the ACR macroplastics velocities towards the upstream direction gradually decreased. Moreover, as further secondary waves arrived, the ACR macroplastics velocities towards the upstream direction increased (Figure 3-6). The average D = 2.54 cm ACR macroplastics maximum upstream transport, $x_{p-upstream}$, was normalized with the time of occurrence, t_{op}, and surge wave celerity. The average horizontal transport of D = 2.54 cm ACR macroplastics towards the upstream direction in an undular surge wave were $(x_{p-upstream}/t_{op})/c$ = 0.03, from the surge-ACR impact point, as shown in Figure 3-7.

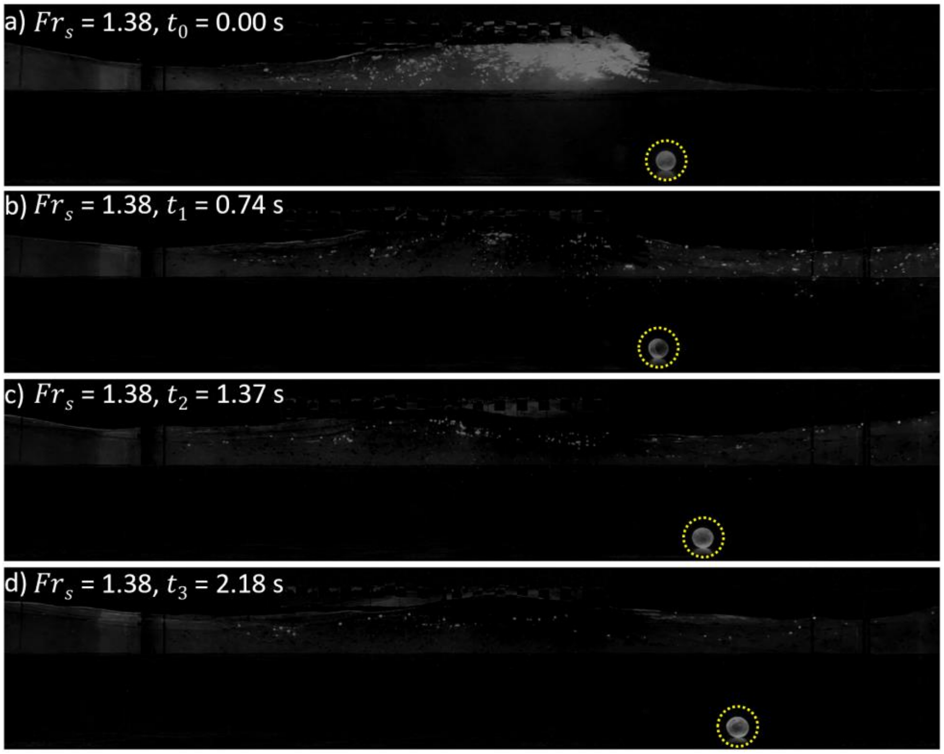

Figure 3-6. Successive frames depicting the interaction of D = 2.54 cm ACR macroplastic in Fr_s = 1.38, showing: a) surge-ACR impact, b) ACR macroplastic slowing down, c) upstream motion due to second undulation, and d) ACR macroplastic slowing down due to wave trough. Surge wave is advancing upstream (left to right). See supplementary file Figure 3-6 Fr1.38 D2.54cm ACR GX012032.

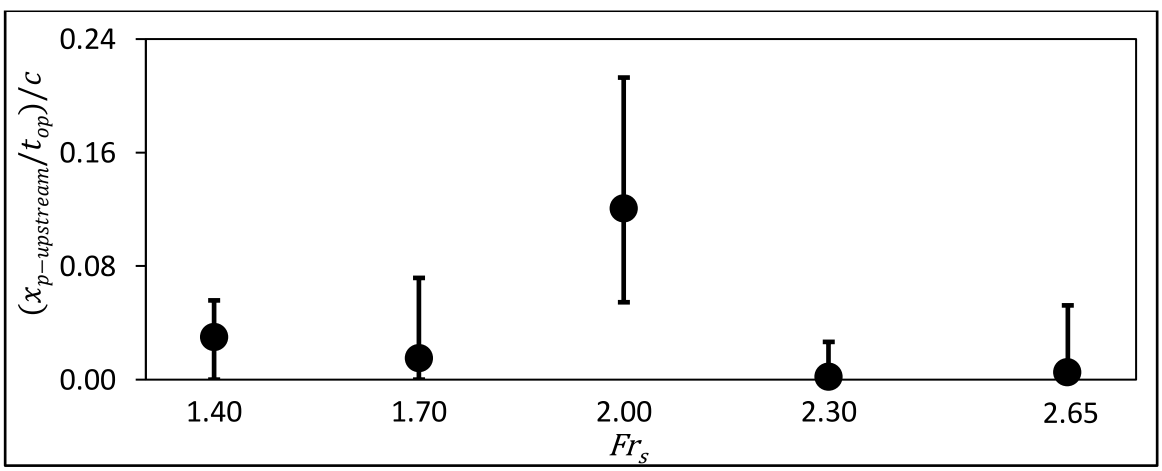

Figure 3-7. Average D = 2.54 cm ACR macroplastics maximum upstream transport, $x_{p-upstream}$, normalized with the time of occurrence, t_{op}, and surge wave celerity. The error bar line shows the minimum and the maximum transport from the surge-ACR impact point for the 20 runs.

A different transport mechanism was observed for the weak breaking surge waves with Fr_s = 1.70. In this case, the ACR macroplastics were influenced by the transient recirculation region, a region where longitudinal velocities are in the upstream direction. After the passage of the surge wave, ACR macroplastics came to a halt much quicker than those in an undular surge wave, and the macroplastics continued upstream as far as 0.07 from the surge-ACR impact point, as shown in Figure 3-8. In some cases, the ACR macroplastics continued downstream, however, most of the ACR macroplastics had sustained upstream transport with an average of 0.01 (Figure 3-7).

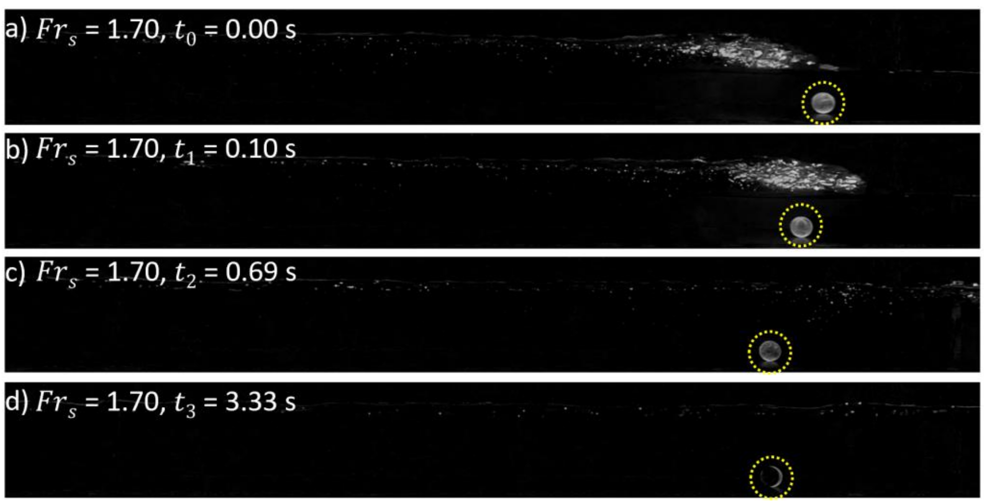

Figure 3-8. Successive frames depicting the interaction of D = 2.54 cm ACR macroplastic in Fr_s = 1.70, showing: a) surge-ACR impact, b) ACR macroplastic slowing down, c) ACR macroplastic is stationary, and d) upstream motion of ACR. Surge wave is advancing upstream (left to right).

Similar to the Fr_s = 1.70, ACR macroplastics in Fr_s = 2.00, also had continuous upstream motion. According to the literature, transient recirculation is higher in surge waves with higher surge wave Froude number. Due to stronger recirculation velocities, after the passage of the surge wave ACR macroplastics decelerated rapidly and started propagating upstream (Figure 3-9). Consequently, the ACR macroplastics with a D = 2.54 cm had an upstream transport of as much as 0.12 (Figure 3-7).

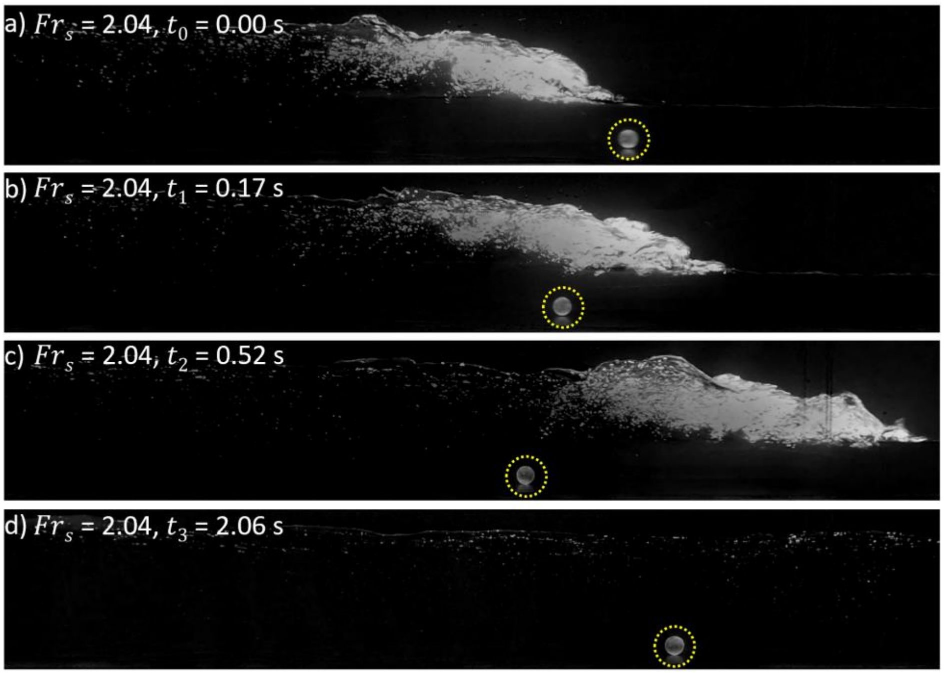

Figure 3-9. Successive frames depicting the interaction of D = 2.54 cm ACR macroplastic in Fr_s = 2.04, showing: a) surge-ACR impact, b) ACR macroplastic slowing down, c) ACR macroplastic is stationary, and d) upstream motion of ACR. Surge wave is advancing upstream (left to right). See supplementary file Figure 3-9 Fr2.04 D2.54cm ACR GX011178.

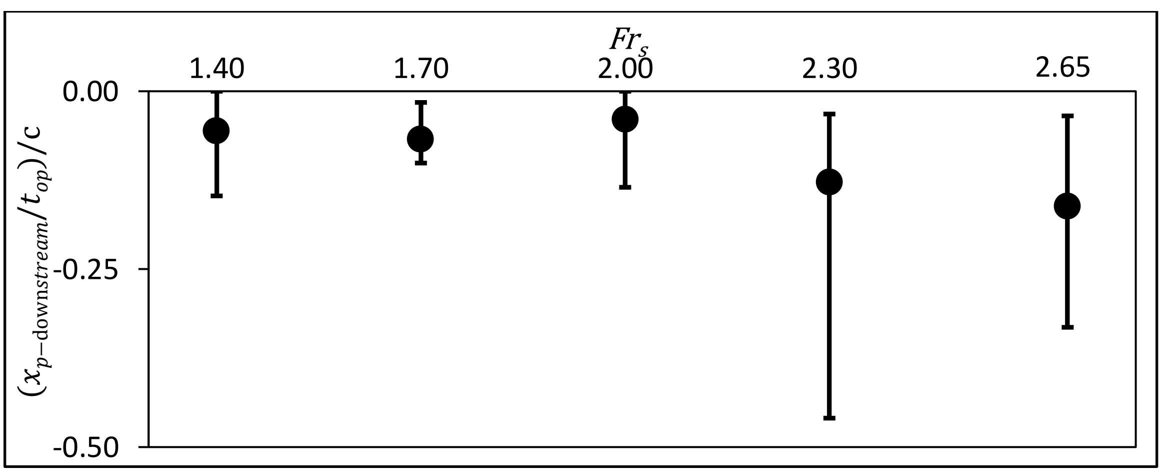

Figure 3-10. Average D = 2.54 cm ACR macroplastics maximum downstream transport, $x_{p-downstream}$, normalized with the time of occurrence, t_{op}, and surge wave celerity. The error bar

line shows the minimum and the maximum transport from the surge-ACR impact point for the 20 runs.

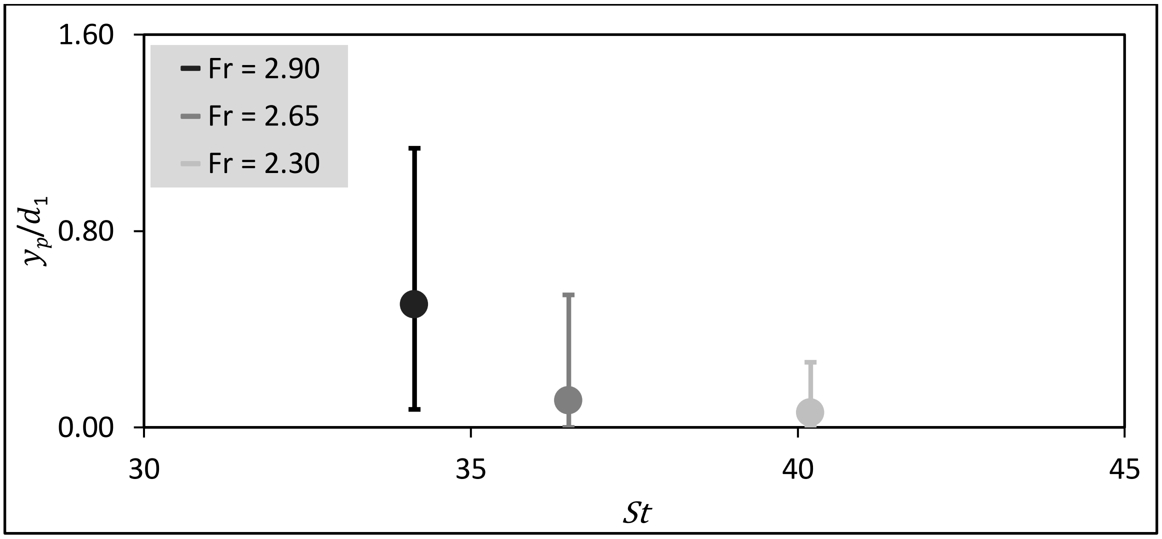

Figure 3-11. Average D = 2.54 cm ACR macroplastics vertical movement, y_p, normalized with d_1. The error bar line shows the minimum and the maximum vertical movement of the 20 runs.

Despite the higher transient recirculation forces in surge waves with higher Fr_s = 2.30, a distinct transport process was recorded. The D = 2.54 cm ACR macroplastics in these surge waves had prolonged motion in the downstream direction, between -0.46 to 0.03, as shown in Figure 3-5 (d). Few cases had slight upstream movement due to the stronger transient recirculation region. However, after the effect of transient recirculation was lessened, along with higher upstream velocity acting against the recirculation region, ACR macroplastics eventually continued downstream with an average transport of $(x_{p-downstream}/t_{op})/c$ = -0.13 due to the residual velocity (Figure 3-10). In addition, wave motion resulted in minimal vertical transport of y_p/d_1 = 0.06 (Figure 3-11), due to the turbulent mixing beneath the surge wave front (Figure 3-12). Heavier ACR macroplastics can be mobilized against gravity if the turbulent motion is greater, where the vertical drag force is greater than the weight of ACR macroplastics. Higher turbulent kinetic energy increases the vertical velocity, resulting in a greater opposing force. This transpires behind the surge wave toe, where according to Li et al. (2021) the turbulent kinetic energy is maximum.

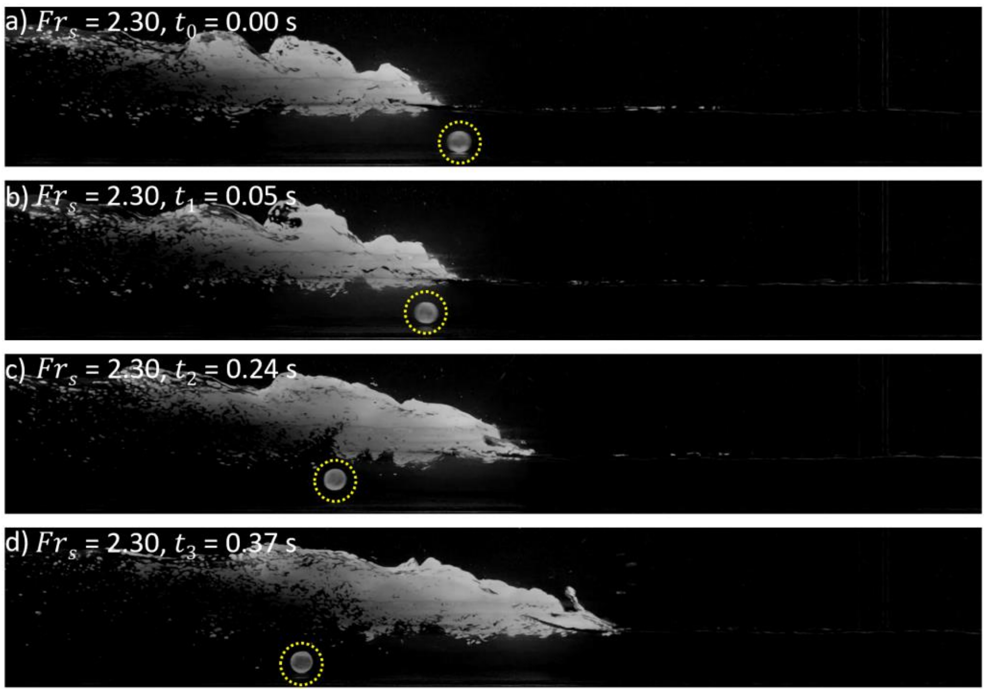

Figure 3-12. Successive frames depicting the interaction of D = 2.54 cm ACR macroplastic in Fr_s = 2.30, showing: a) surge-ACR impact, b) vertical transport initiated, c) peak vertical transport, and d) ACR on the flume bed. Surge wave is advancing upstream (left to right).

Macroplastics transport in Fr_s = 2.65 were comparable to that of those experimented in Fr_s = 2.30. For Fr_s = 2.65, the effect of transient recirculation was more evident as few D = 2.54 cm ACR macroplastics had visible upstream transport, as shown in Figure 3-5 (e). However, the upstream velocity acting in opposition to recirculation velocities, impeded ACR macroplastics transport in the upstream direction and carried them towards downstream. Almost all the D = 2.54 cm ACR macroplastics were decelerated by the recirculation zone, while continuing in the downstream direction. In addition, higher upstream velocity was associated with higher surge wave Froude number (Table 2-2), which resulted in higher initial velocity of the ACR macroplastics. Corresponding, higher initial momentum and greater escape force from the mixing region. The transport was between -0.33 to 0.05, as shown in Figure 3-5 (e), with an average downstream motion of -0.16 (Figure 3-10). At higher surge wave Froude number, the turbulent motion is higher, which can mobilize heavier ACR macroplastics against gravity. At Fr_S = 2.65 turbulent motion was higher than that of Fr_S = 2.30, and the vertical drag force was greater than the weight of ACR macroplastics. Furthermore, the ACR macroplastics Stokes number was lower, compared to the Stokes number at Fr_S = 2.30 (Figure 3-11), therefore lower particle relaxation time. Consequently, the average vertical transport was 0.11, greater than that of Fr_S = 2.30 (Figure 3-11). Overall, minimal vertical transport was visible at this surge wave Froude number (Figure 3-13). However, the advection of ACR macroplastics while in suspension had not occurred.

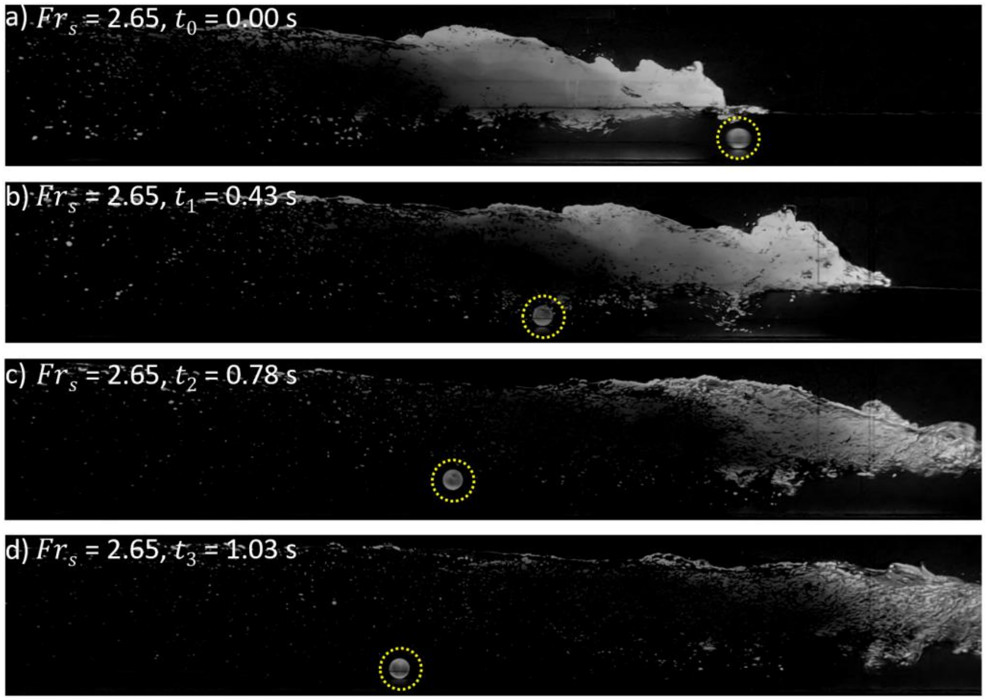

Figure 3-13. Successive frames depicting the interaction of D = 2.54 cm ACR macroplastic in Fr_s = 2.65, showing: a) surge-ACR impact, b) vertical transport began, c) peak vertical transport, and d) ACR on the flume bed. Surge wave is advancing upstream (left to right). See supplementary file Figure 3-13 Fr2.65 D2.54cm ACR GX011779.

For the Fr_s = 2.90, visual analysis was performed due to the limitations of the experimental setup. The D = 2.54 cm ACR macroplastics experimented in Fr_s = 2.90, also had prolonged downstream transport (Figure 3-4). The ACR macroplastics were decelerated, and some become stationary after the passage of the surge wave. However, most of the ACR macroplastics had continued moving in the downstream direction. At this surge wave Froude number, the turbulent motion was higher compared to Fr_s = 2.30 and 2.65, hence the vertical drag force was much greater than the ACR macroplastics. Moreover, the ACR macroplastics Stokes number was also lower compared to the Stokes number of ACR at Fr_s = 2.30 and 2.65 (Figure 3-11), resulting in a lower particle relaxation time. As a result, notable vertical transport was observed; the D = 2.54 cm ACR macroplastics were lifted with an average range of 0.50 in the vertical direction (Figure 3-11), the entrainment in highly aerated surge wave roller as shown in Figure 3-14 (c). However, transport towards the upstream direction, while in suspension, had not occurred.

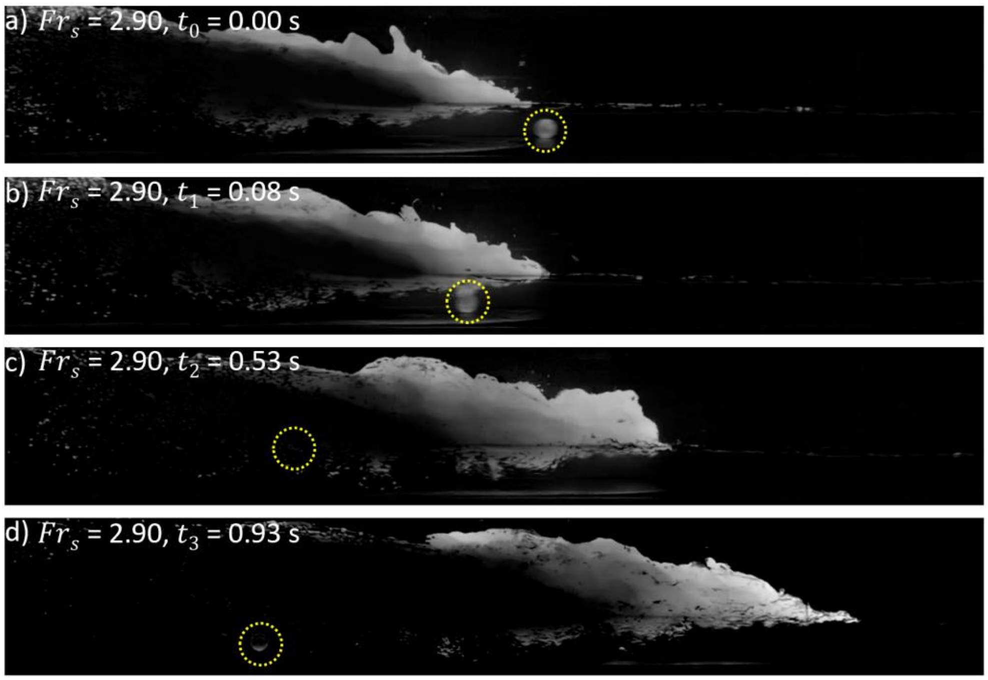

Figure 3-14. Successive frames depicting the interaction of D = 2.54 cm ACR macroplastic in Fr_s = 2.90, showing: a) surge-ACR impact, b) vertical transport initiated, c) peak vertical transport, and d) ACR on the flume bed. Surge wave is advancing upstream (left to right).

A similar transport process was observed at Fr_s = 4.90. The influence of transient recirculation was more notable than all the lower surge wave Froude numbers examined. Although the D = 2.54 cm ACR macroplastic had insignificant horizontal transport, as shown in Figure 3-4, intense turbulent mixing beneath the surge wave front displayed significant vertical transport. The ACR macroplastic was lifted vertically as far as 1.51 cm in the water column due to substantial turbulent wave motion (Figure 3-11). As surge wave Froude number increased, so did the vertical motion of D = 2.54 cm ACR macroplastics. For small sediment particles, Koch & Chanson (2008) have reported the influence of highly turbulent surge waves on the sediments, as bed erosion was initiated underneath the surge wave front where debris was suspended due to wave motion. This phenomenon was observed for D = 2.54 cm ACR macroplastics in Fr_s = 2.90 and 4.90. As previously discussed, stronger turbulent motion leads to greater vertical drag force on the ACR macroplastics, forcing them higher in the water column; farther downstream, away from the surge wave, the particle returns to flume bed, as turbulent intensity is lessened. This phenomenon was observed for Fr_s = 4.90, where turbulent motion was the strongest compared to all the previously examined surge wave Froude numbers. The D = 2.54 cm ACR macroplastic was entrained in the highly aerated surge wave roller, and was carried upstream with the surge wave, while it was suspended in the water column, as shown in Figure 3-15 (d). This was not observed with lower surge wave Froude numbers. As the effect of turbulent intensity lessened, the ACR macroplastic returned to the flume bed, as shown in Figure 3-15 (e).

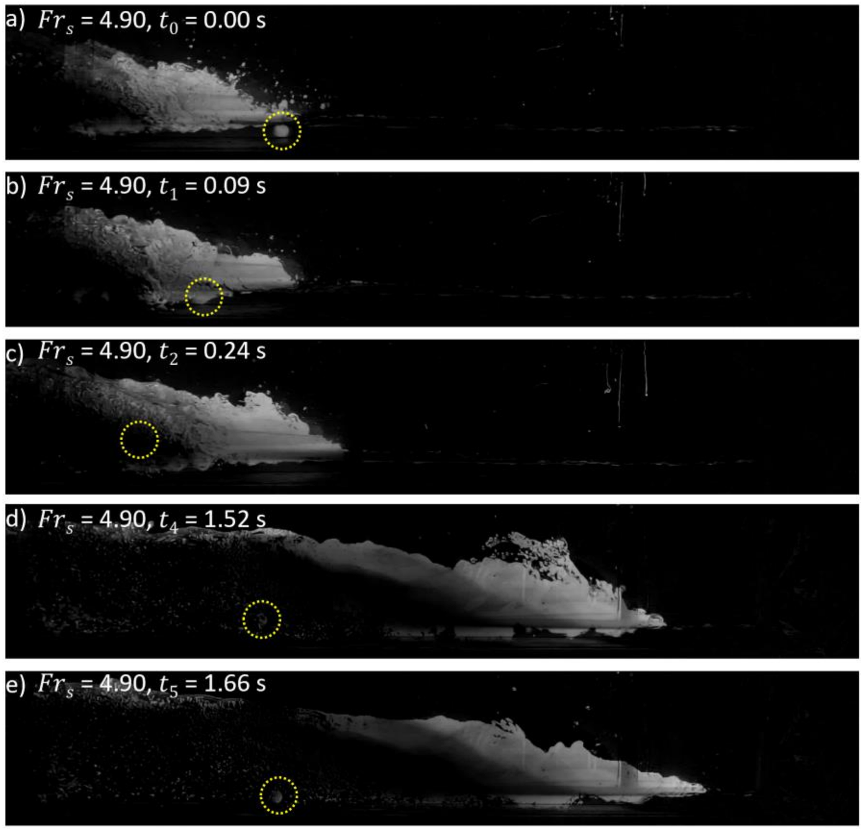

Figure 3-15. Successive frames depicting the interaction of D = 2.54 cm ACR macroplastic in Fr_s = 4.90, showing: a) is after the surge-ACR impact, b) is when the vertical transport was initiated, c) is peak vertical movement, d) entrainment in the surge wave roller, and e) ACR back to the flume bed. Surge wave is advancing upstream (left to right).

The negatively buoyant macroplastic horizontal transport can be justified by impulse. Impulse is a function of force exerted over a specific time. These two parameters affecting the impulse, played a crucial role in the negatively buoyant macroplastics transport. In a undular surge wave and weak breaking surge waves (Fr_s = 1.70 and 2.00), the extended mixing cone length decelerated the ACR macroplastic, changing the macroplastics's direction. The force exerted on the ACR macroplastic was over a longer time interval due to the prolonged mixing layer behind the surge wave, which contributed to a greater change in momentum. Furthermore, the upstream velocity, at lower surge wave

Froude number was smaller; consequently ACR macroplastics upstream velocity was lower, and the overall momentum was smaller. In an undular surge wave and weak breaking surge waves, the combination of lower initial momentum and the extended mixing cone length, provided adequate time to alter ACR macroplastics motion. In addition, transient recirculation was present at weak breaking surge waves, which further influenced the ACR macroplastics motion, and carried them further upstream. There was adequate balance between the lower momentum of the macroplastic and the mixing layer in weak breaking surge waves, which contributed to the maximum horizontal transport in the upstream direction.

The strength of the roller and transient recirculation were stronger at higher Fr_S = 2.30 and 2.65. Furthermore, the mixing layer envelope was also wider. Therefore, the time interval over which the force was applied was smaller. Greater forces applied over a smaller time interval resulted in a lower impulse. In addition, increased upstream velocity, resulted in higher upstream velocity of the ACR macroplastics. Hence, the ACR macroplastics moved rapidly from the undisturbed region to behind the surge wave, across the mixing layer. Greater ACR momentum, along with lower impulse due to shorter mixing layer length and smaller time interval, justified the sustained downstream motion at higher surge wave Froude numbers.

Despite the wider mixing layer envelope and shorter time interval, the intense turbulent mixing and transient recirculation beneath the surge wave front in Fr_S = 4.90, overpowered the ACR macroplastics initial momentum. Implying that substantial force was exerted on the D = 2.54 cm ACR macroplastic over a much shorter time interval, resulting in greater impulse, which carried the ACR macroplastic upstream while it was partially suspended.

As the surge wave Froude number increased, the turbulent kinetic energy increased. This increased the vertical drag on the ACR macroplastics, overpowering the weight and leading to higher vertical transport. Furthermore, as the surge wave Froude number increased, the Stokes number for D = 2.54 cm ACR macroplastics decreased (Table 3-1), and lower Stokes number indicates higher entrainment. As results have shown, vertical transport was initiated at Fr_s = 2.30. As the surge wave Froude number increased, higher vertical transport and greater entrainment of D = 2.54 cm ACR macroplastics was observed, due to strong turbulent motion behind the surge toe. Substantial turbulent motion can lift particles in the water column and transport them upstream while in suspension, which occurs behind the surge wave toe, where the turbulent kinetic energy is maximum. Horizontal transport of D = 2.54 cm ACR macroplastic while in suspension did not transpire even at Fr_s = 2.90 but was observed at Fr_s = 4.90, where turbulent kinetic energy was substantial.

Table 3-1. Particle Stokes number (St) for various sized ACR macroplastics.

Fr_s	$c + u_1$ (cm/s)			St		
	D = 2.54 cm	D = 1.91 cm	D = 1.11 cm	D = 2.54 cm	D = 1.91 cm	D = 1.11 cm
2.65	178.01	177.60	176.58	36.49	20.69	7.03
2.30	161.68	158.58	158.11	40.20	23.16	7.85
2.00	151.74	s150.07	153.62	42.83	24.49	8.08
1.70	116.15	115.15	112.86	55.93	31.90	10.99
1.40	133.05	132.12	132.17	48.81	27.80	9.38

3.4.3 ACR transport varying with macroplastic size

Macroplastic entrainment can be greatly influenced by the particle size, as described by the Stokes number. In this section, the impact of varying ACR macroplastic with D = 2.54, 1.91, and 1.11 cm is investigated. As described by the Stokes number, size is an important parameter since particle diameter have substantial influence on the particle's trajectory. The impact of size is reflected by the particle diameter being squared in the particle relaxation time, Eq. 1-1. This results in the Stokes number for D = 2.54 cm ACR macroplastic being more than times five larger than the D = 1.11 cm macroplastic. The ACR macroplastics with higher Stokes number are dominated by their inertia, and as particle Stokes number decreases, ACR macroplastics can exhibit a slightly different transport mechanism in which the dominance of their inertia is lessened.

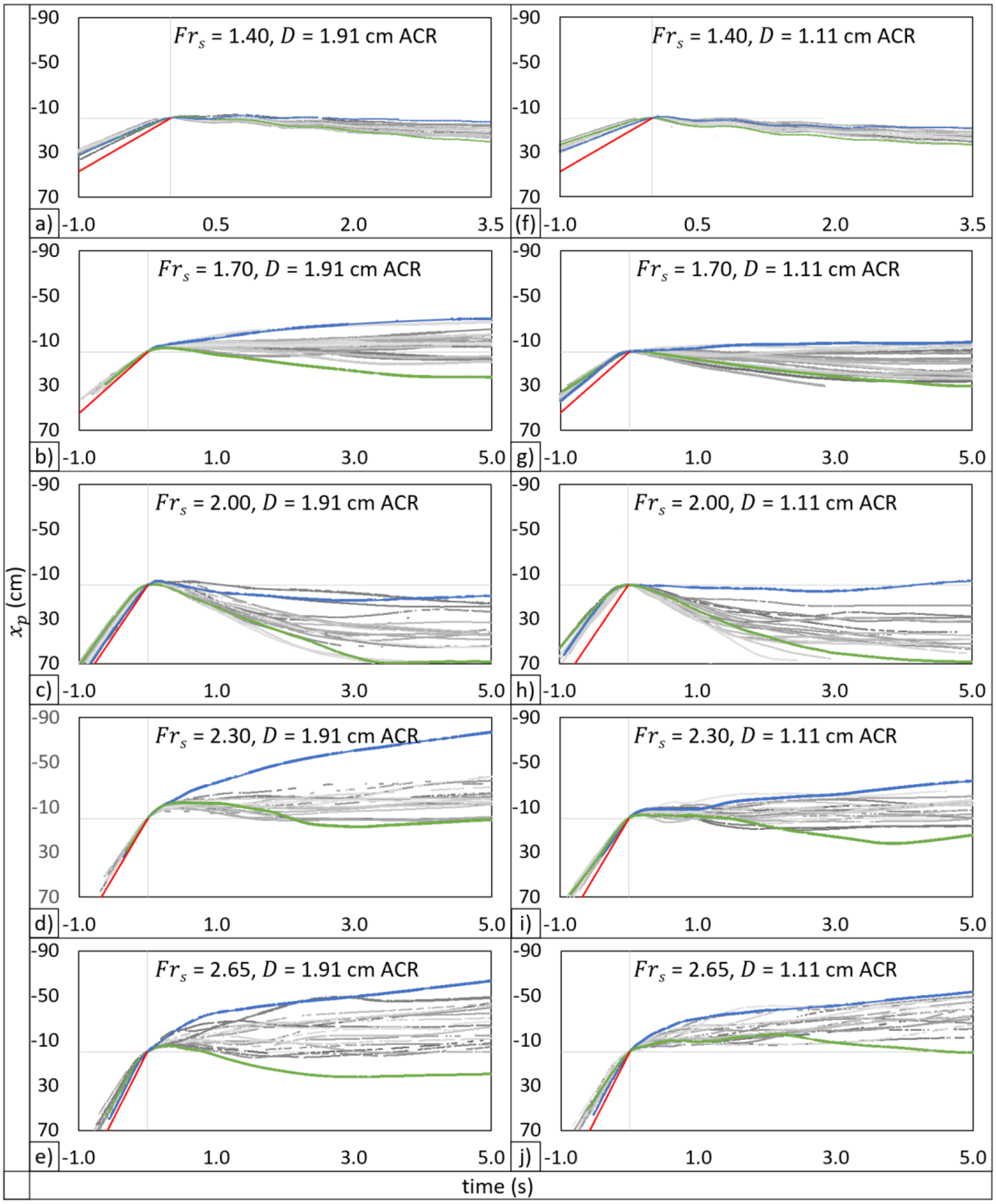

Figure 3-16. Trajectories of D = 1.91 and 1.11 cm ACR macroplastics. Negative and positive positions in the x-direction (x_p) translate to downstream and upstream movement of the macroplastic, respectively. The minimum and maximum horizontal upstream transport when the surge wave arrives at the inlet is highlighted by the blue and the green, respectively. The red line represents upstream velocity and the grey curves represent the other 18 experiments.

In an undular surge wave, the transport of the ACR macroplastics in the upstream direction increased, as the macroplastic size decreased, as illustrated in Figure 3-5 (a), Figure 3-16 (a) & (f), and Figure 3-17. After the passage of the undular surge wave roller, ACR macroplastics started deaccelerating and became stationary (Figure 3-16). The macroplastics then started propagating upstream as the train of secondary undulation waves arrived. As the effect of the secondary undulation waves was diminished, macroplastics upstream velocities gradually decreased. In Fr_s = 1.40, as the Stokes number decreased (Table 3-1) higher horizontal transport in the upstream direction was observed. The D = 2.54 cm ACR macroplastics had an average upstream motion of 0.03 in the upstream direction, from the surge-ACR impact point (Figure 3-7). While the average upstream transport reported for D = 1.91 cm ACR macroplastics was 0.04 (Figure 3-18), and for the smallest ACR macroplastics with a D = 1.11 cm, average upstream movement was 0.05 (Figure 3-18). As the macroplastics size decreased, greater horizontal transport was documented, since smaller ACR macroplastics had lower initial momentum; hence easier for the surge wave to overpower the initial momentum and transport smaller macroplastics further in the horizontal direction. At last, vertical transport of ACR macroplastics had not occurred, since the turbulent motion at Fr_s = 1.40 was not adequate to induce lift.

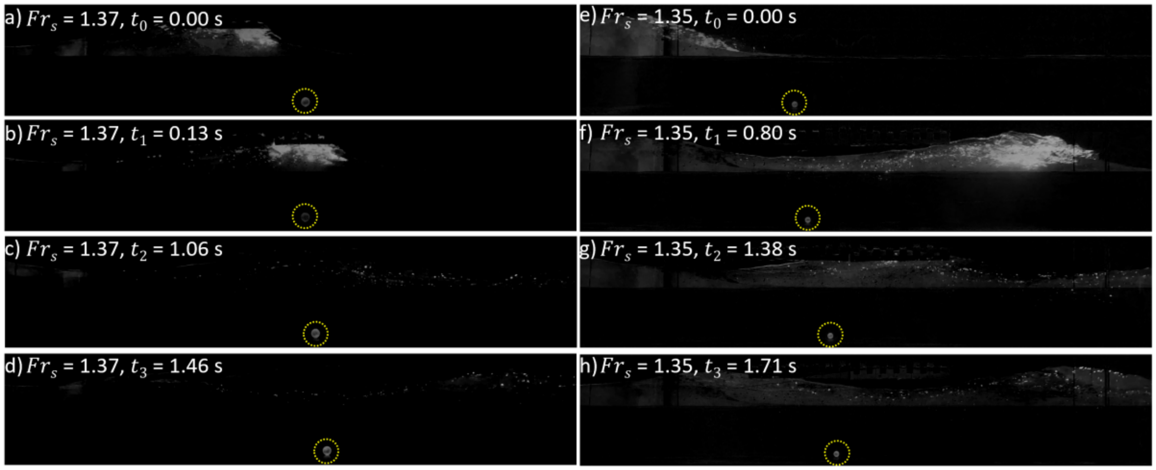

Figure 3-17. Sequence of images showing the interaction of: a) – d) D = 1.91 cm ACR macroplastics in Fr_s = 1.37, and e) – h) D = 1.11 cm ACR macroplastics in Fr_s = 1.35. Where: a) & e) surge-ACR impact, b) & f) ACR macroplastic slowing down, c) & g) upstream motion due second undulation, and d) & h) ACR macroplastic slowing down in wave trough. Surge wave is advancing upstream (left to right).

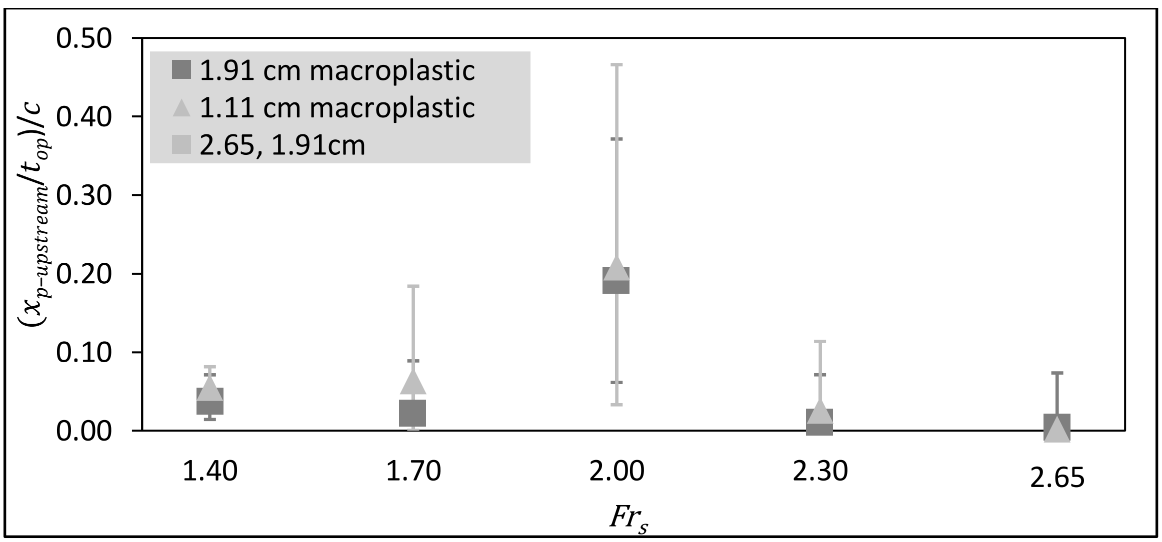

Figure 3-18. Average D = 1.91 and 1.11 cm ACR macroplastics maximum upstream transport, $x_{p-upstream}$, normalized with the time of occurrence, t_{op}, and surge wave celerity. The error bar line shows the minimum and the maximum transport from the surge-ACR impact point of the 20 runs.

Comparable transport was also observed for the weak breaking surge wave (Fr_s = 1.70). In this case, after the surge wave passage, ACR macroplastics advanced further upstream as the macroplastic size decreased. The D = 2.54 cm ACR macroplastics, with the highest relaxation time and Stokes number (Table 3-1), had an average upstream transport of 0.01, from the surge-ACR impact point (Figure 3-7). Furthermore, for D = 1.91 cm ACR macroplastics, the overall average transport increased in upstream direction (0.02), as shown in Figure 3-18 and Figure 3-19 (a) – (d). Following the trend for the D = 1.11 cm ACR macroplastics, the average upstream advancement was 0.06, as shown in Figure 3-18 and Figure 3-19 (e) – (h). There was an increase in the horizontal transport as the ACR macroplastics size decreased. This was due to smaller ACR macroplastics having a lower initial momentum; allowing the surge wave to overcome the initial momentum and carry smaller ACR macroplastics further upstream. The surge wave at Fr_s = 1.70 was a breaking surge wave, however, the turbulent motion was not sufficient to induce vertical motion.

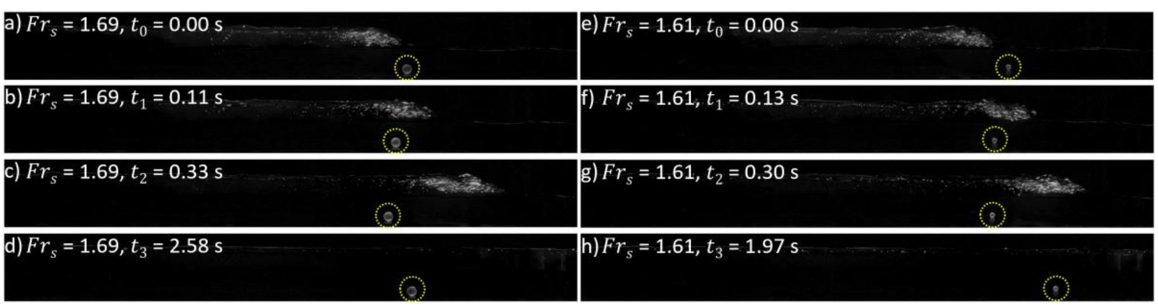

Figure 3-19. Sequential frames illustrating the engagement of: a) – d) D = 1.91 cm ACR macroplastics in Fr_s = 1.69, and e) – h) D = 1.11 cm ACR macroplastics in Fr_s = 1.61. Where: a) & e) surge-ACR impact, b) & f) ACR macroplastic slowing down due to recirculation region, c) & g) ACR macroplastic is stationary, and d) & h) upstream motion of ACR. Surge wave is advancing upstream (left to right).

Similar behaviour was reported for the ACR macroplastics in the surge waves with Fr_s = 2.00, where the average upstream propagation for D = 2.54, 1.91, and 1.11 cm ACR macroplastics increased to 0.12, 0.19, and 0.21, respectively, as shown in Figure 3-7, Figure

3-18, and Figure 3-16 (c) & (h). A slightly higher upstream transport had occurred for D = 1.91 cm ACR macroplastics in Fr_s = 2.00. However, the overall trajectories indicated that as the macroplastic size decreased, there was a rapid change in the ACR macroplastics transport after the surge wave passage, as shown by the slope of the trajectories in Figure 3-5, Figure 3-16, and Figure 3-20. As previously discussed, the increase in the horizontal transport as the macroplastic size decreased, is due smaller initial momentum. Which enabled the surge wave to overcome the ACR macroplastics initial momentum induced by the upstream velocity and move smaller ACR macroplastics further in horizontal direction. The breaking surge wave strength at Fr_s = 2.00 was adequate to transport ACR macroplastics upstream, however, the turbulent motion was not enough to induce lift for vertical transport.

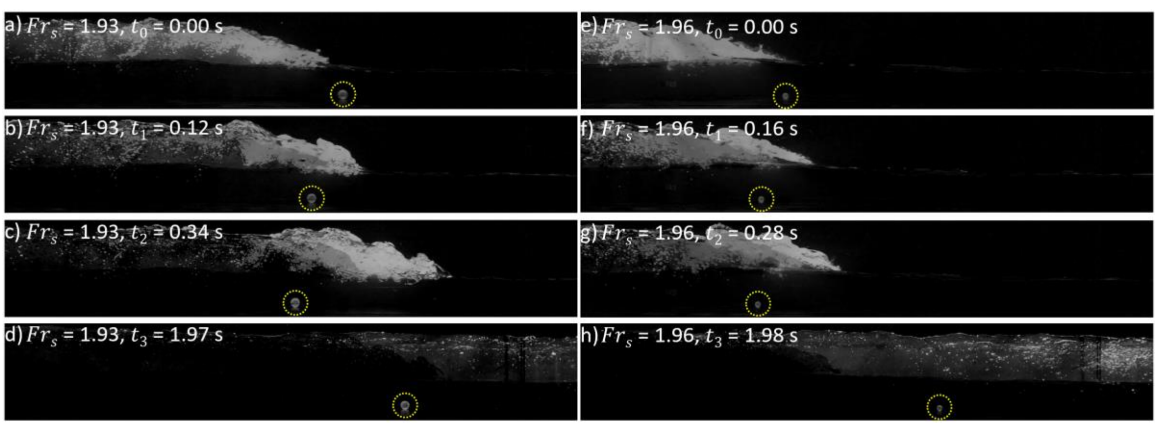

Figure 3-20. Subsequent frames showing the engagement of: a) – d) D = 1.91 cm ACR macroplastics in Fr_s = 1.93, and e) – h) D = 1.11 cm ACR macroplastics in Fr_s = 1.96. Where: a) & e) surge-ACR impact, b) & f) ACR macroplastic slowing down due to recirculation region, c) & g) ACR macroplastic is stationary, and d) & h) upstream motion of ACR. Surge wave is advancing upstream (left to right).

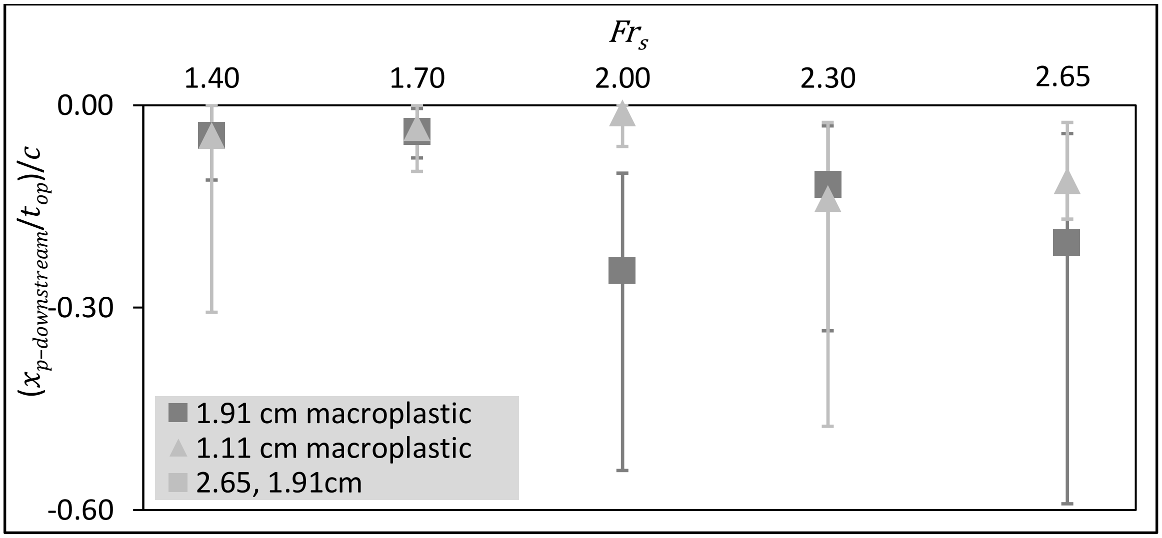

Figure 3-21. Average D = 1.91 and 1.11 cm ACR macroplastics maximum downstream transport, $x_{p-downstream}$, normalized with the time of occurrence, t_{op}, and surge wave celerity. The error bar line shows the minimum and the maximum transport from the surge-ACR impact point of the 20 runs.

Similar correlation between ACR macroplastic size and its transport was observed at higher surge wave Froude numbers (2.30). Due to the higher initial momentum, the D = 2.54 cm ACR macroplastics were less influenced by the surge wave and stayed on their original path toward the downstream, as shown in Figure 3-5 (d). There were a few cases where the D = 2.54, 1.91, and 1.11 cm ACR macroplastics were transported upstream for a fraction of a second after the passage of the surge wave, as shown in Figure 3-5 (d) and Figure 3-16 (d) & (i). However, the overall data shows that the smaller D = 1.91 and 1.11 cm ACR macroplastics continued downstream with an average transport of -0.12 and -0.14, respectively (Figure 3-21). As the macroplastic size decreased, the initial momentum was lower, implying possible upstream transport as the macroplastic size decreased. However, the initial momentum was considerably higher even for the smallest D = 1.11 cm ACR macroplastics. Furthermore, at Fr_s = 2.30 the strength of the roller was stronger, and the mixing layer envelope was wider. Consequently, the ACR macroplastics travelling at the upstream velocity, rapidly passed though the mixing layer cone and continued downstream. As a result, a reduction in the average downstream transport was observed as the macroplastic size decreased (Figure 3-10 and Figure 3-21), indicating it was easier for the smallest ACR macroplastics to be influenced. In addition, negatively buoyant ACR macroplastics are mobilized against gravity when the turbulent motion is substantial, where the vertical drag force is greater than the weight of ACR macroplastics. This occurs, since higher turbulent kinetic energy results in a higher vertical velocity and greater vertical drag, leading to a bigger opposing force. According to Li et al. (2021), turbulent kinetic energy is maximum behind the surge wave toe. Owing to the intense turbulent mixing underneath the surge wave front, wave motion led to vertical transport of D = 2.54, 1.91, and 1.11 cm ACR macroplastics (Figure 3-11, Figure 3-22, and Figure 3-23). Furthermore, the D = 1.91 and 1.11 cm ACR macroplastics had an average vertical transport of 0.06 and 0.07, respectively (Figure 3-23). As the Stokes number decreased (Table 3-1), higher entrainment was documented. Smaller ACR macroplastics have higher surface area and projected area, compared to volume. Since smaller ACR macroplastics have a lower volume, hence lower weight, it becomes easier for vertical drag force, induced by turbulent motion, to entrain smaller ACR macroplastics in the vertical direction. Since it was easier lift the smaller macroplastics, at Fr_s = 2.30, D = 1.11 cm ACR macroplastics had a slight upstream transport while in suspension, as shown in Figure 3-22 (f) & (g).

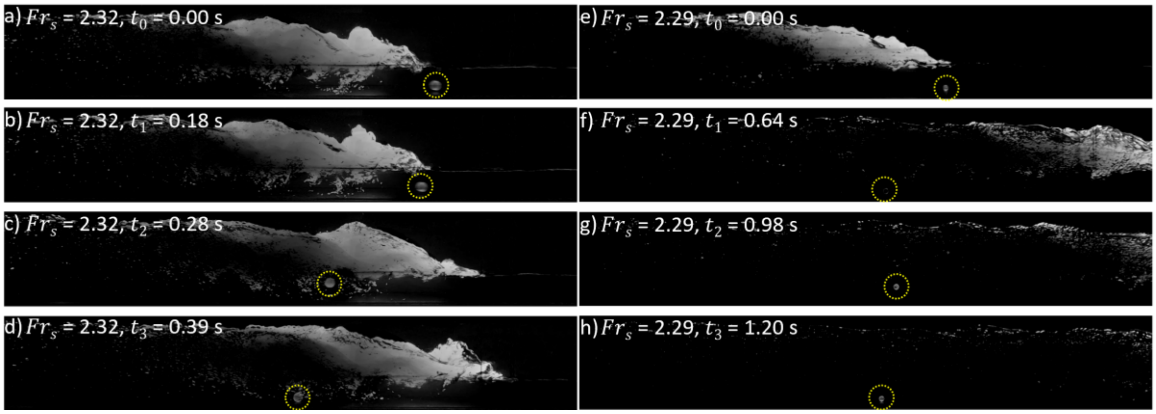

Figure 3-22. Successive frames showing the interaction of: a) – d) D = 1.91 cm ACR macroplastics in Fr_s =2.32, and e) – h) D = 1.11 cm ACR macroplastics in Fr_s = 2.29. Where: a) & e) surge-ACR impact, b) & f) initiation of vertical transport, c) & g) peak vertical transport, and d) & h) ACR on bed. Surge wave is advancing upstream (left to right).

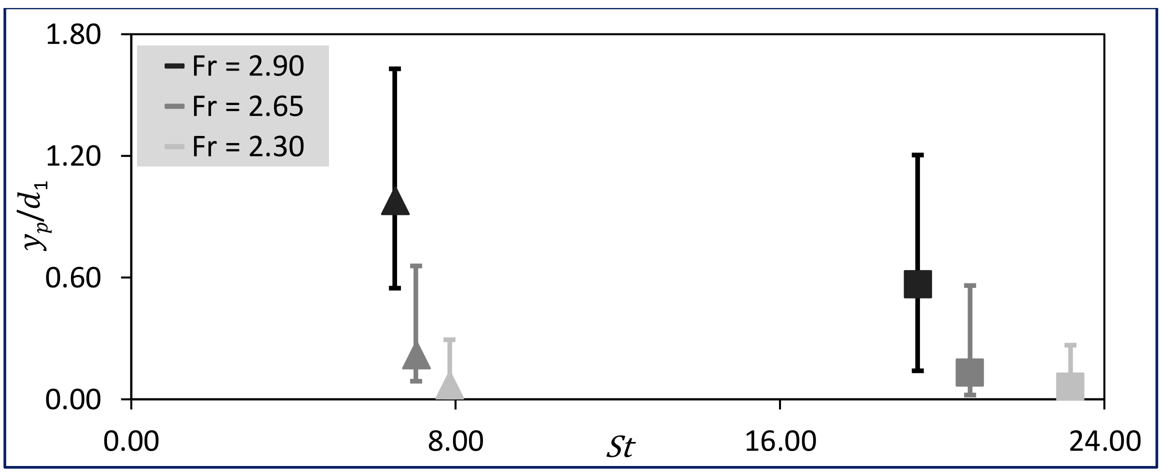

Figure 3-23. Average ACR macroplastics vertical movement, y_p, normalized with d_1. Square and triangle indicate D = 1.91 and 1.11 cm ACR macroplastics, respectively. The error bar line shows the minimum and the maximum of the 20 runs.

Similar trend was identified when ACR macroplastics were tested in a surge wave with Fr_s = 2.65. The D = 2.54 cm ACR macroplastics were carried downstream with an average of -0.16, from the surge-ACR impact point (Figure 3-10). As the macroplastic diameter decreased from 1.91 to 1.11 cm, the average transport towards the downstream region decreased from -0.20 to -0.11, respectively (Figure 3-21). Implying that particles with lower initial momentum will be more influenced by the surge wave, as demonstrated by the reduction in the overall downstream transport as the macroplastic size decreased (Figure 3-10 and Figure 3-21). As previously discussed, higher ACR macroplastics initial momentum, and wider mixing led to the sustained downstream motion of all ACR macroplastics. In addition, greater vertical entrainment was recorded as the ACR macroplastics size decreased. The ACR macroplastics were entrained in the developing mixing layer behind the surge wave, due to intense upwards wave motion. The smallest D = 1.11 cm ACR macroplastics displayed higher vertical displacement of 0.22, compared to D = 1.91 cm ACR macroplastics, which had an average vertical motion of 0.13 (Figure 3-23 and Figure 3-24). Vertical entrainment increased as the Stokes number decreased (Table 3-1). As previously discussed, smaller ACR macroplastics have lower volume, which allowed the turbulent motion to further entrain smaller ACR macroplastics in the vertical direction.

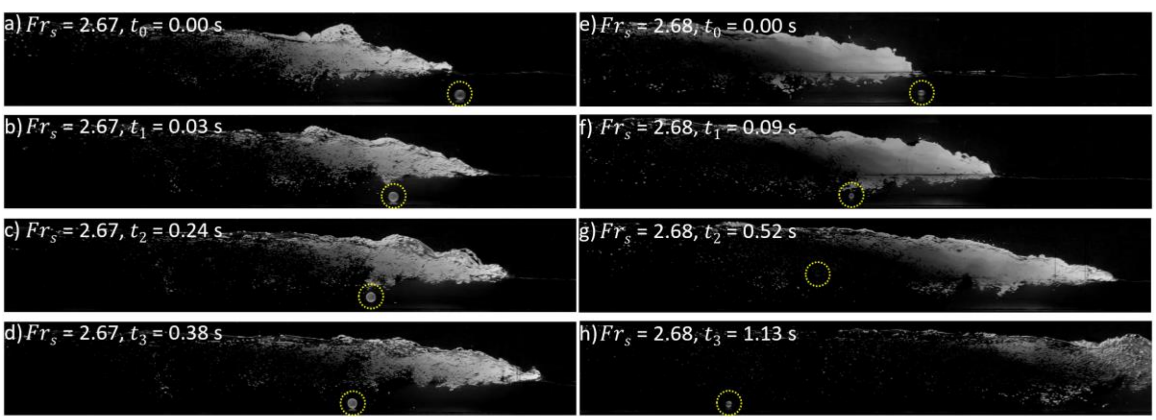

Figure 3-24. Sequential frames illustrating the engagement of: a) – d) D = 1.91 cm ACR macroplastics in Fr_s = 2.67, and e) – h) D = 1.11 cm ACR macroplastics in Fr_s = 2.68. Where: a) & e) surge-ACR impact, b) & f) initiation of vertical transport, c) & g) peak vertical transport, and d) & h) ACR on bed. Surge wave is advancing upstream (left to right).

At Fr_s = 2.90, horizontal transport was observed, but it was not quantified due to the limitations. However, the vertical transport was quantified. At this surge wave Froude number macroplastics were observed near the free surface. The D = 1.11 cm macroplastic was almost near the free surface, as shown in Figure 3-25 (g), while the D = 1.91 cm macroplastic was getting closer to the free surface, as shown in Figure 3-25 (c). The D = 2.54 cm ACR macroplastics had an average vertical motion of 0.50, while the smaller D = 1.91 and 1.11 cm macroplastics exhibited higher vertical translation of 0.57 and 0.98, respectively, as reported in Figure 3-11 and Figure 3-23. As previously discussed, smaller ACR macroplastics had higher vertical entertainment.

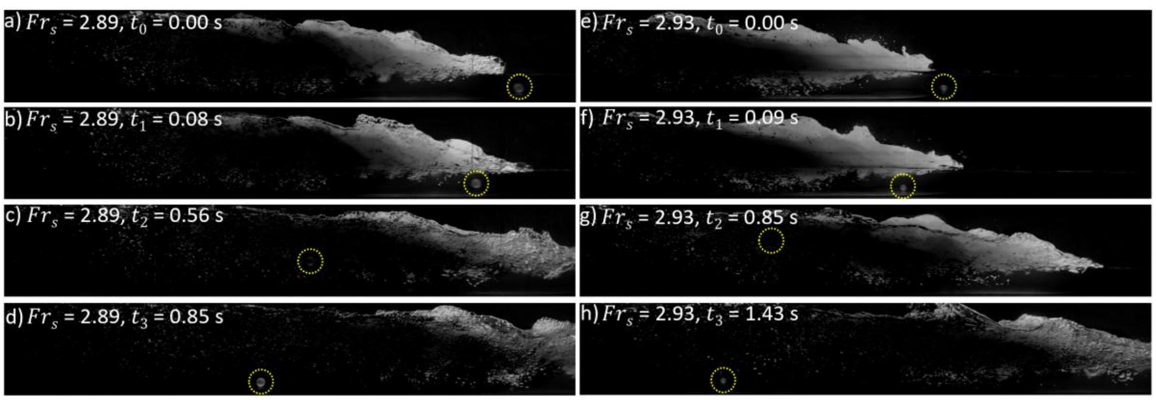

Figure 3-25. Sequence of images showing the interaction of: a) – d) D = 1.91 cm ACR macroplastics in Fr_s = 2.89, and e) – h) D = 1.11 cm ACR macroplastics in Fr_s = 2.93. Where: a) & e) surge-ACR impact, b) & f) initiation of vertical transport, c) & g) peak vertical transport, and d) & h) ACR on bed. Surge wave is advancing upstream (left to right).

At the Fr_s = 4.90, substantial vertical transport was observed (Figure 3-26). The D = 2.54 cm ACR macroplastic had vertical transport towards the upstream, with slight transport while in suspension (Figure 3-15), as discussed in Section 3.4.2. In addition to the upstream transport while in suspension, the D = 1.91 cm ACR macroplastic moved upstream due to the developing mixing layer and was rapidly advected downstream, while it was fully suspended, as shown in Figure 3-26 (a) – (e). Moreover, the D = 1.91 cm macroplastic was lifted as far as the water-surface. The smallest ACR macroplastic displayed additional transport. The D = 1.11 cm negatively buoyant macroplastic was lifted to the developing mixing layer, from there the macroplastic was convected upwards to the free surface, while moving upstream, as shown in Figure 3-26 (f) – (i). The transport process of D = 1.11 cm ACR occurred while the negatively buoyant macroplastic was in suspension, and the transport was that of a positively buoyant macroplastic.

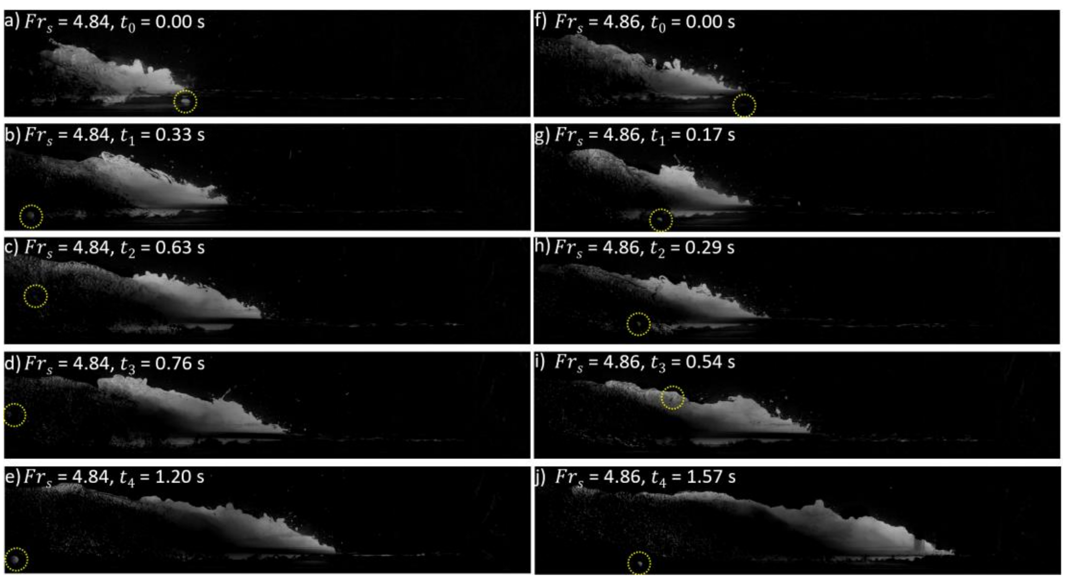

Figure 3-26. Sequence of images showing the entrainment of: a) – e) D = 1.91 cm ACR macroplastics in Fr_s of 4.84, and f) – j) D = 1.11 cm ACR macroplastics in Fr_s of 4.86, where: a) & f) surge-ACR impact, b) & g) vertical transport began, c) & i) peak vertical transport, d) & h) entrainment in the surge wave roller, and d) & j) ACR on bed. Surge wave is advancing upstream (left to right).

The change in horizontal transport of negatively buoyant macroplastics was evident with smaller macroplastics. At Fr_s = 1.40, 1.70, and 2.00, as the macroplastics size decreased, horizontal transport in the upstream direction increased. Since smaller ACR macroplastics had lower initial momentum, allowing the surge wave to overpower the initial momentum and transport smaller ACR macroplastics upstream. Furthermore, at lower surge wave Froude numbers, the mixing cone length was narrower and extended further downstream, away from the surge wave toe. The combination of lower initial momentum, as the ACR macroplastics size decreased, and the extended mixing cone length provided sufficient time to mobilize the ACR macroplastics in the upstream direction. Consequently, smaller ACR macroplastics had greater transport in the upstream direction.

At Fr_s = 2.30 and 2.65, the turbulent motion wave greater compared to lower surge wave Froude numbers. However, the upstream velocity at higher surge wave Froude number was also significant. Furthermore, the mixing cone formed behind the surge wave was much wider and shorter, resulting in a lower time interval to influence ACR macroplastics. The adequate balance provided enough momentum to ACR macroplastics across all the sizes to excel through the energy intensive turbulent motion, resulting in a sustained downstream motion. The D = 2.54 cm ACR macroplastics travelled further downstream, and as the ACR macroplastics size decreased, transport in the downstream direction decreased. Implying that as the ACR macroplastics size decreased, the influence of the surge wave on ACR macroplastics increased.

The rapid velocity redistributions, correlated with the long-lasting turbulent wave motion, scour bed debris, advect the material upwards, and contribute to upstream transport. Higher transverse velocities and flow separation scour and erode bed material, as reviewed by Chanson & Lubin (2013). The materials present in the water column are then mixed in the developing mixing layer behind the surge wave. As surge wave Froude number increased, turbulent mixing beneath the surge wave roller was higher, subsequently there was flow separation and large transverse velocities. This resulted in upward advection of ACR macroplastics in the developing mixing layer. It was speculated in the literature, that the bed debris was convected upwards to free surface (Chanson & Lubin, 2013). Higher turbulent wave motion is produced behind the surge wave toe as the surge wave Froude number increases. Such a phenomenon can generate higher turbulent kinetic energy, resulting in a higher vertical drag, which can lift negatively buoyant macroplastics against gravity. Vertical entrainment of ACR macroplastics was initiated at Fr_s = 2.30. Where the smallest, D = 1.11 cm ACR macroplastics had minor vertical entrainment, while the other two sizes examined did not. As higher surge wave Foude number were examined, vertical entrainment for D = 1.91 cm ACR macroplastics followed by D = 2.54 cm ACR macroplastics was documented. As discussed, higher surge wave Froude number led to higher vertical entrainment. As a result, the smallest ACR macroplastics eventually reached the free surface after the passage of the surge wave roller. At last, as the surge wave Froude number increased, the considerable turbulent mixing was able to transport ACR macroplastics in the horizontal direction towards upstream, while the macroplastics were suspended due to wave motion. This was first observed for D = 1.11 cm ACR macroplastics. Overall results indicate that greater vertical entrainment had occurred as the ACR macroplastics size decreased, since it was easier to mobilize smaller ACR macroplastics with lower particle relaxation time.

Chapter 4 – Surge Wave Mixing and Dynamics of Positively Buoyant Macroplastics

This chapter presents and discusses the transport of positively buoyant macroplastics. In this chapter visual observations are discussed first in Section 4.1. Moreover, the impact that surge waves with different surge wave Froude numbers have on positively buoyant macroplastics, is investigated in Section 4.2. Lastly, the effects of particle size on transport of HDPE and PP macroplastics are discussed in Section 4.3.

For microplastics, Cózar et al. (2014) reported that the smaller debris are mainly found in water column and deep-sea sediment. This has been linked to biofouling and in-depth entrainment of micro-sized plastic debris (Shamskhany et al., 2021). As demonstrated in Chanson (2010b) and as shown in Figure 3-3, the turbulent intensity across breaking surge waves is very high. In the presence of such highly turbulent flow, it is hypothesized that meso and macro-sized plastic debris also get entrained. This section investigates the transport and entrainment of HDPE and PP macroplastics, in such turbulent flow. Both these polymers in aquatic systems are positively buoyant as have densities marginally smaller than freshwater.

4.1 Initial Observations

The entrainment and transport of positively buoyant macroplastics are affected by several factors. These include particle and flow characteristics. In this section, initial observations of positively buoyant macroplastic's interaction with the surge wave are presented.

Positively buoyant, HDPE (ρ_p = 0.94 to 0.97 g/cm^3) and PP (ρ_p = 0.90 to 0.93 g/cm^3) macroplastics displayed different transport mechanisms due to their density and with varying surge wave Froude numbers. Interaction of D = 2.54 cm HDPE and PP macroplastics in an undular and breaking surge wave are shown in Figure 4-1. In Figure 4-2, the position of D = 2.54 cm HDPE and PP macroplastics in the *x* and *y* directions, x_p and y_p, are plotted. Figure 4-2 shows the horizontal and vertical transport of both HDPE and PP macroplastics; horizontal and vertical transport is analyzed in the sections below. In an undular surge wave with Fr_s = 1.40, surge wave front was gradual, while in a breaking surge wave with Fr_s = 1.70, the surge wave front was a bit steeper. Turbulent structures are initiated due to pressure and velocity gradient. Higher turbulent structures at higher surge wave Froude number have the potential to mobilize HDPE and PP macroplastics against their buoyancy. Positively buoyant macroplastics were near the free surface before and after the surge wave. However, both the HDPE and PP macroplastics were engaged in the surge wave roller and mobilized opposite to their buoyancy (Figure 4-1). As anticipated, HDPE and PP macroplastics were partially masked by the aeration in the surge wave roller; higher surge wave Froude number led to greater aeration at the surge wave front (Figure 4-1). The impact of relative density in the particle relaxation time played a crucial role. The horizontal transport increased as smaller macroplastics were tested.

For positively buoyant macroplastics, as the particles are mainly positioned closer to the free surface, their position was further masked by the aeration. Owing to the limitation of the PTV program as it is purely based on the image analysis, positively buoyant macroplastics in surge wave with Fr_s > 1.70 were not analyzed. However, visual observations and analysis were performed for both HDPE and PP macroplastics.

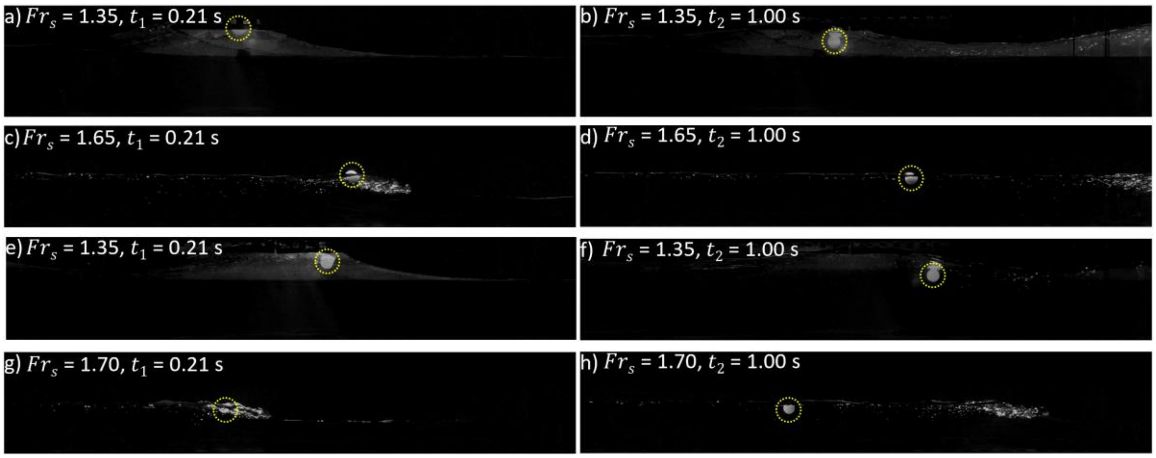

Figure 4-1. Successive frames showing the interaction of D = 2.54 cm: a) & b) HDPE macroplastic in Fr_s = 1.35, c) & d) HDPE macroplastic in Fr_s = 1.65, e) & f) PP macroplastic in Fr_s = 1.35, and g) & h) PP macroplastic in Fr_s = 1.70. The left column and the right column show the position of a positively buoyant macroplastic at 0.21 s and 1.00 s after impacting the surge wave front, respectively. Surge wave is advancing upstream (left to right).

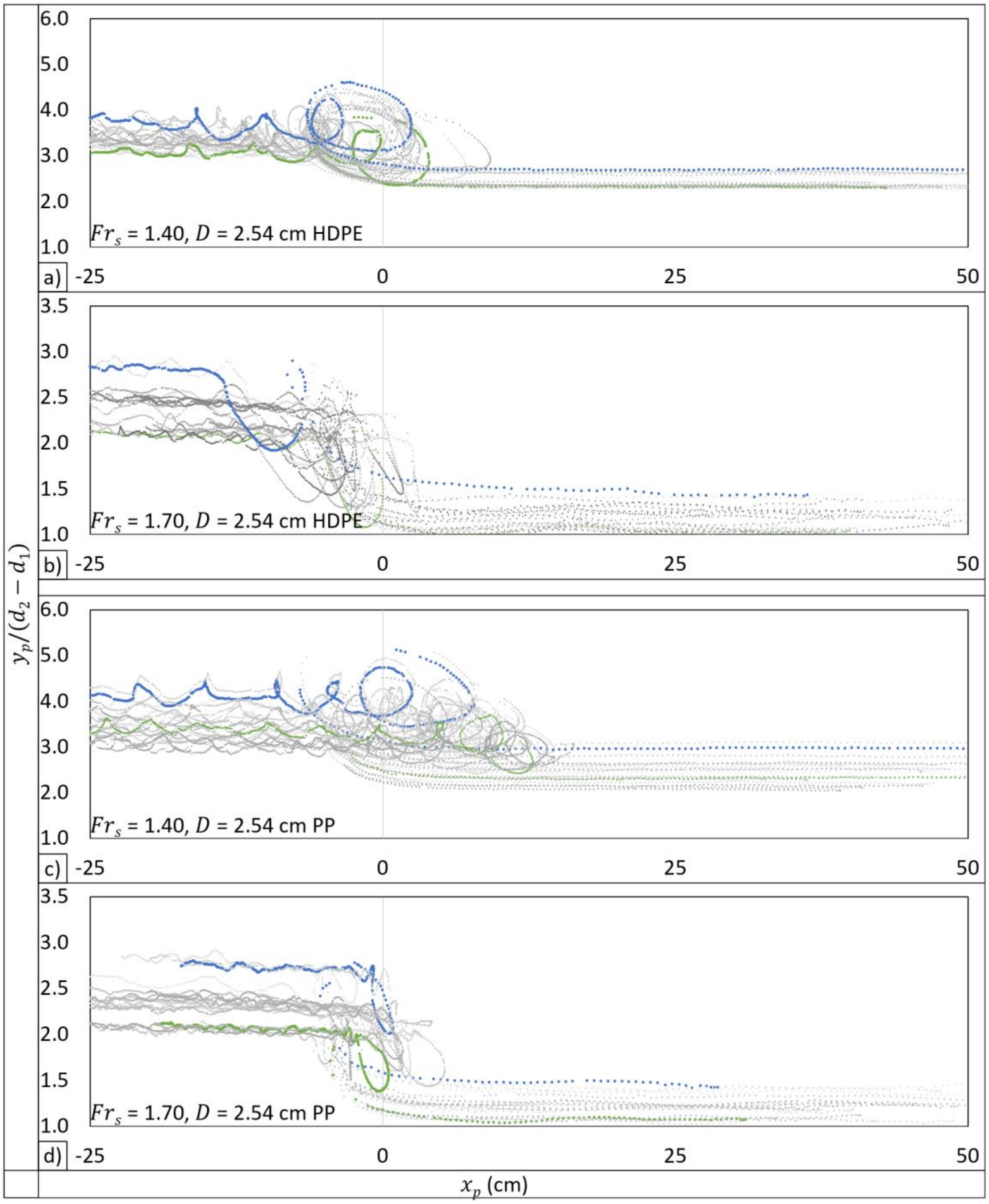

Figure 4-2. Trajectories of D = 2.54 cm HDPE and PP macroplastics. The vertical translation is normalized by surge wave height, $d_2 - d_1$. The x_p represents the horizontal position, which is along the flume bed. Here in each figure, plots of different runs with similar initial condition and macroplastics properties are presented with different colored dashed lines. The coordinates (0, 1) represent the surge-buoyant macroplastic impact point. The minimum and the maximum vertical transport are denoted by green and blue, respectively. The grey curves represent the other 18 experiments.

4.2 Influence of Fr_s on the transport of HDPE and PP macroplastics

The strength of the surge wave roller in a breaking surge wave governs the entrainment of positively buoyant debris. In this section, the impact of surge wave Froude number on positively buoyant macroplastics is studied. To investigate this, HDPE and PP macroplastics with a D = 2.54 cm were analyzed in surge wave with Fr_s = 1.40 and 1.70, and visual analysis was performed for macroplastics in Fr_s = 2.00 and 2.30.

The particle Stokes number (Eq. 1-2) can explain the entrainment of positively buoyant HDPE and PP macroplastics. Smaller difference between the macroplastic density and the density of the ambient fluid results in a lower relaxation time and therefore a lower Stokes number. Macroplastics with lower Stokes number can be more entertained in the flow. The transport of HDPE and PP macroplastics is analyzed for Fr_s = 1.40 and 1.70, and visual analysis is performed for Fr_s = 2.00 and 2.30.

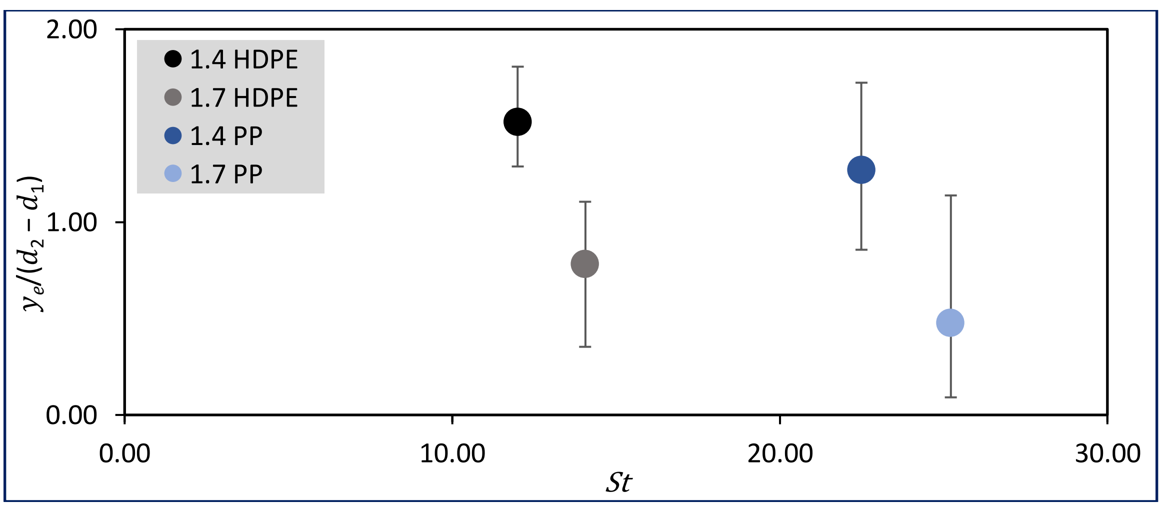

Figure 4-3. Average D = 2.54 cm HDPE and PP macroplastics vertical entrainment range, y_e, normalized by surge height, $d_2 - d_1$. The error bar line shows the minimum and the maximum vertical movement of the 20 runs.

The macroplastics vertical entrainment range, y_e, is determined based on the height difference between the macroplastics minimum position around the surge-buoyant impact point and the maximum vertical position during the entertainment. For an undular surge wave, the maximum position would occur at the primary wave crest, and for breaking surge wave, it would occur behind the surge wave roller. As shown in Figure 4-3, both HDPE and PP macroplastics were staying near the free surface during the entire transport for an undular surge wave with Fr_s = 1.40, and the higher difference in wave crest and tough results in higher vertical transport range. Since the macroplastics follow the free surface, the transport away from the free surface in the vertical direction was minimal, indicating minor transport in undular surge waves for both HDPE and PP macroplastics across all the sizes examined.

In an undular, both HDPE and PP macroplastics were slightly entrained in the roller. In the Fr_s = 1.40, the D = 2.54 cm HDPE macroplastics had an average vertical transport range of 1.52, whereas PP macroplastics had marginally less vertical transport range, with an average of 1.27, as shown in Figure 4-3. The transport range of HDPE was indicating marginally higher entrainment, than PP macroplastics; since PP was lighter, which resulted in less entrainment, as suggested by Stokes number (Figure 4-3). In an undular surge wave, the strength of the surge wave front was not significant to force positively buoyant macroplastics against its tendency to float. Therefore, both the HDPE and PP macroplastics were near the free surface and were closely following the free surface undulations (Figure 4-4). Consequently, indicating that the Stokes number played a major role in macroplastics vertical transport at Fr_s = 1.40. Furthermore, the lighter PP macroplastics were carried further in horizontal direction with the surge wave celerity, whereas the HDPE macroplastics had moderate impact by the surge wave celerity, as shown in Figure 4-2 (a) & (c). In addition, the secondary wave undulations led to the undulations in the trajectories, as shown in Figure 4-2 (a) & (c). The overall macroplastics trajectory in an undular surge wave was marginally influenced by the surge wave Froude number, and primarily governed by the surge wave celerity and free surface behaviour.

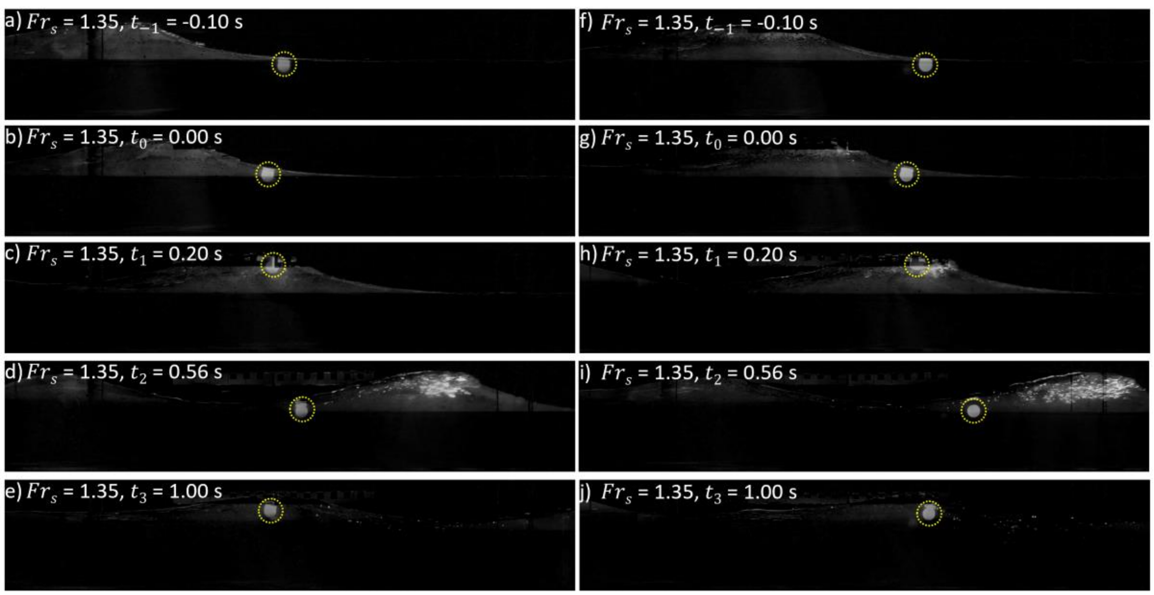

Figure 4-4. Sequence of image illustrating the interaction of D = 2.54 cm: a) – e) HDPE macroplastic in Fr_s = 1.35, and f) – j) PP macroplastic in Fr_s = 1.35. $t = 0$ identifies the surge-buoyant macroplastic impact (moving towards right in these images), and the macroplastics (initially moving towards left with u_1). Where a) & f) prior to impact, b) & g) surge-buoyant macroplastic impact, c) & h) macroplastic in the undular roller, d) & i) macroplastic at the first trough, and e) & j) macroplastic at the crest of the first secondary wave. Surge wave is advancing upstream (left to right). See supplementary file Figure 4-4 Fr1.35 D2.54cm HDPE GX012123.

The engagement of HDPE and PP macroplastics increased when macroplastics were tested in a weak breaking surge wave (Fr_s = 1.70). The D = 2.54 cm HDPE macroplastics had higher average vertical translation range ($y_e/(d_2 - d_1)$ = 0.78), compared to D = 2.54 cm PP macroplastics (0.48), as shown in Figure 4-2 (b) & (d) and Figure 4-3. The vertical transport range of HDPE was greater than that of PP macroplastics; since HDPE had lower marginal density, resulting in a lower particle relaxation time and greater entrainment, as indicated by Stokes number (Figure 4-3). Therefore, suggesting that at Fr_s = 1.70 the Stokes number was a primary factor in macroplastics vertical transport. At Fr_s = 1.70, the breaking of the surge wave front was slightly adequate to force the positively buoyant macroplastics against their buoyancy. However, the positively buoyant macroplastics were only mobilized against their buoyancy for a fraction of a second. Resulting in a different entrainment process at Fr_s = 1.70, compared to Fr_s = 1.40. Where occasionally the HDPE and PP macroplastics were more entrainment in the surge wave. Both the HDPE and PP macroplastics were carried along the mixing layer. This can be seen in Figure 4-5 (b) & (g), where the macroplastics reach the lowest depth. From there the macroplastics moved to the free surface, and then the macroplastics moved upstream as they were entrained in the surge wave roller, behind the surge wave front. As the effect of the surge wave roller was decreased, macroplastics gradually decelerated and started moving downstream (Figure 4-5). Moreover, the horizontal transport of both HDPE and PP in horizontal direction in Fr_s = 1.40 was greater than that of Fr_s = 1.70 (Figure 4-2). Since the higher surge wave celerity at Fr_s = 1.40 and the wave undulations exerted a higher horizontal force in the upstream direction.

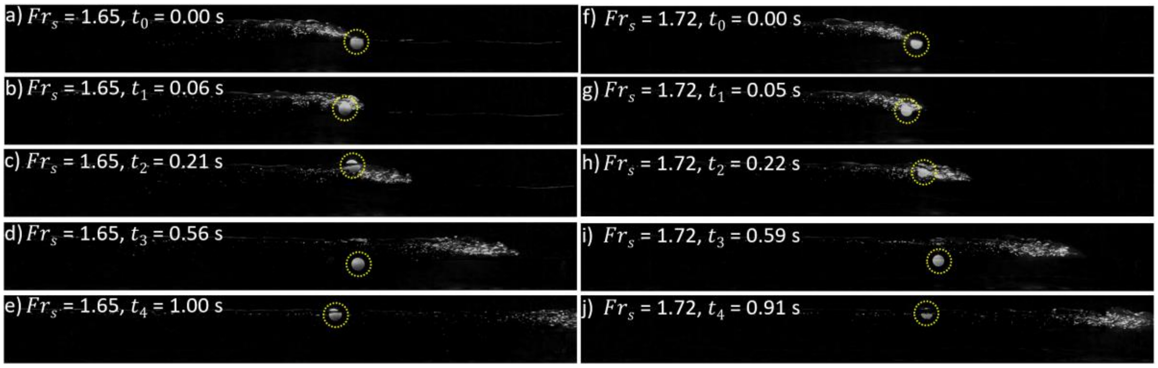

Figure 4-5. Successive frames showing the engagement of D = 2.54 cm: a) – e) HDPE macroplastic in Fr_s = 1.65, and f) – j) PP macroplastic in Fr_s = 1.72. Where a) & f) surge-buoyant macroplastic impact, b) & g), macroplastic along the developing mixing layer, c) & h) macroplastic entrained in the roller, d) & i) macroplastic forced down the water column, and e) & j) macroplastic rising to free surface. Surge wave is advancing upstream (left to right). See supplementary file Figure 4-5 Fr1.65 D2.54cm HDPE GX010567.

4.2.1 Entrainment at high Froude numbers

A marginally different entrainment was observed for a weak breaking surge wave in a Fr_s = 2.00. Vertical translation was not quantified. However, visual observations confirm that the entrainment for both HDPE and PP macroplastics in aerated surge wave roller was higher, when compared to the Fr_s = 1.40 and 1.70 (Figure 4-4, Figure 4-5, and Figure 4-6). In addition, the transport across the surge wave, where the macroplastics tend to follow its original path of staying near the free surface, similar to that of Fr_s = 1.40 and most of 1.70, were not observed. Instead, at this surge wave Froude number: a) the HDPE and PP macroplastics were being carried along the developing mixing layer, b) rising to free surface, c) entrained behind the surge wave, and d) continuing downstream after the effect of surge wave roller decreased, as shown in Figure 4-6. Implying that Fr_s = 2.00 had the ability to mobilize HDPE and PP macroplastics in opposition to their buoyancy for a slightly extended period (Figure 4-6).

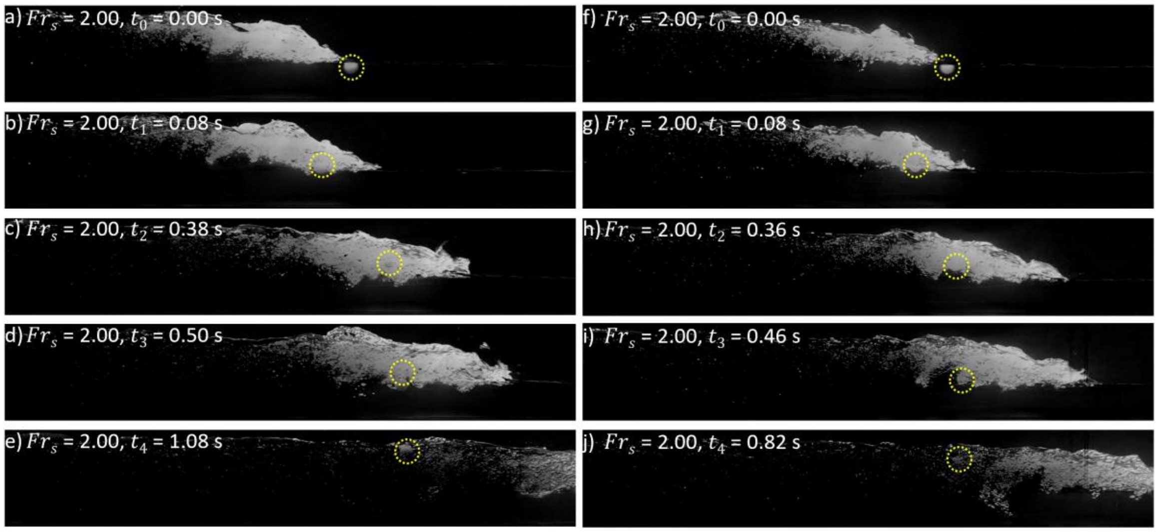

Figure 4-6. Sequential frames depicting the interaction of D = 2.54 cm: a) – e) HDPE macroplastic in Fr_s = 2.00, and f) – j) PP macroplastic in Fr_s = 2.00. Where a) & f) surge-buoyant macroplastic impact, b) & g), macroplastic along the developing mixing layer, c) & h) macroplastic entrained in the roller, d) & i) macroplastic forced down the water column, and e) & j) macroplastic rising to free surface. Surge wave is advancing upstream (left to right).

The next surge wave Froude number examined (Fr_s = 2.30) displayed intense turbulent structures. At this surge wave Froude number, both HDPE and PP macroplastics were considerably entrained in the highly aerated surge wave roller. The macroplastics were no longer staying near the free surface and were pushed down the water column due to the breaking of the surge wave roller, unlike the lower surge wave Froude numbers tested. From the surge-buoyant impact point, the macroplastic would travel along the lower shear envelope and rise behind the surge front, closer to the free surface, some distance behind the surge front. However, the effect of the turbulent surge wave roller was still present and the macroplastic would be entrained in the roller. The surge wave roller overpowered the buoyancy and forced the macroplastic towards the upstream direction, behind the surge front. For this Froude number, two distinct transport mechanisms were observed at this point onwards in the entrainment process. Firstly, the macroplastic would continue to be entrained behind the surge wave, until the effect of the turbulent surge wave roller was weakened. In this range of Froude number Li et al. (2021) also reported sustained mixing behind the surge wave. This was associated with stronger shear layer formation at higher Froude numbers. As the surge wave propagated upstream, the influence of the turbulent structure behind the surge front was reduced, and the buoyancy of the macroplastic gradually regulated its position in the water column (Figure 4-7). For the second entrainment process, the breaking of the roller phenomenon carried the macroplastic closer to the impingement point. The breaking of the roller transported the macroplastic as far as the lower shear envelope and occasionally to the flume bed, all against the macroplastic's natural tendency to float. In the meantime, the surge wave had advanced upstream with its celerity, and the effect of the roller was lessened. Consequently, the macroplastic gradually started rising in the water column, eventually to the free surface, as its buoyancy started to govern its position in the water column (Figure 4-7). Moreover, slight horizontal transport (upstream bound) was observed as the macroplastic rose back to the free surface after escaping the surge wave roller, as shown in Figure 4-7 (e) & (k). Suggesting that the macroplastic may get entrained in the roller once again and repeat the second half of the second entrainment process in surge waves with Froude number of greater than 2.30. The first entrainment process is vaguely similar to the one observed in weak breaking surge waves. However, the second entrainment process was only observed starting from larger surge wave Froude numbers (> 2.30). In addition, HDPE and PP macroplastics were considerably involved in the second entrainment process, which resulted in higher vertical transport.

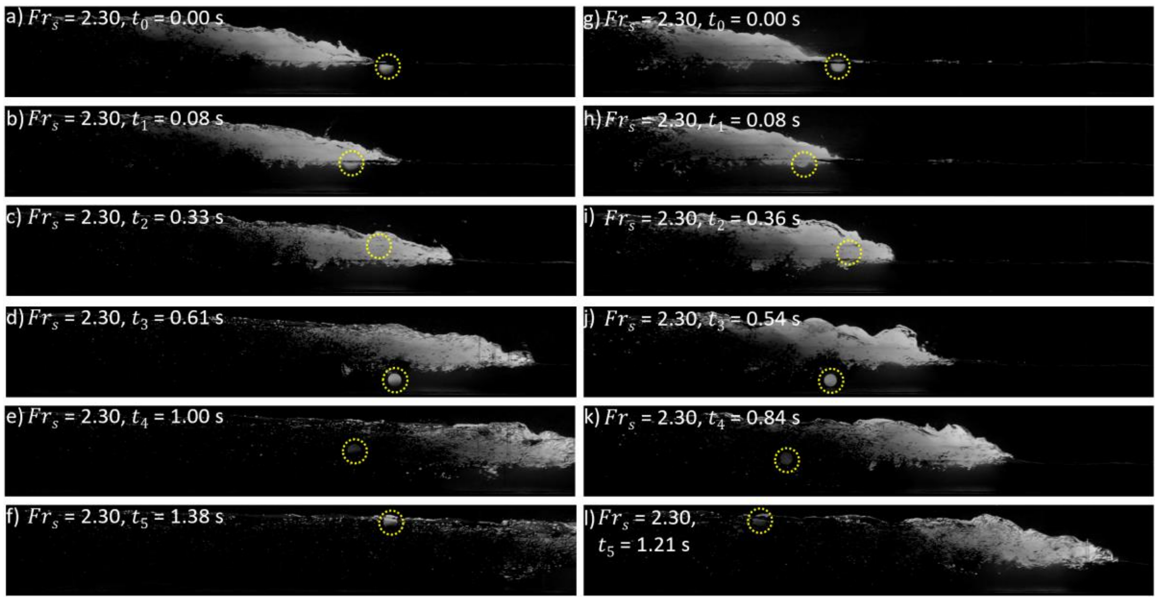

Figure 4-7. Series of frames illustrating the engagement of D = 2.54 cm: a) – f) HDPE macroplastic in Fr_s = 2.30, and g) – l) PP macroplastic in Fr_s = 2.30. Where a) & f) surge-buoyant macroplastic impact, b) & h), macroplastic along the developing mixing layer, c) & i) macroplastic entrained in the roller, d) & j) macroplastic forced down the water column, e) & k) macroplastic rising to free surface with influence of the surge wave roller, f) & l) macroplastic at the free surface. Surge wave is advancing upstream (left to right). See supplementary file Figure 4-7 Fr2.30 D2.54cm HDPE GX011536.

The results indicated that as the surge wave Froude number increased, entrainment of the D = 2.54 cm positively buoyant macroplastics in the surge wave increased. Stokes number was a governing factor in D = 2.54 cm macroplastics vertical entrainment; HDPE with a lower Stokes number exhibited greater vertical transport than PP. In an undular surge wave, the density of the macroplastic mainly regulated its transport across the surge wave. As the surge wave Froude number increased, the effect of D = 2.54 cm macroplastic buoyancy was lessened across the surge wave, and the roller strength dominated the macroplastic's transport process. Subsequently the macroplastic's buoyancy dominated its position in the water column. At higher surge wave Froude number, a different entrainment process was observed, where the D = 2.54 cm macroplastics were forced to mobilize against its buoyancy. In some cases, macroplastics were pushed as far as the lower shear envelope and occasionally to the flume bed, all against their natural tendency to float. The D = 2.54 cm HDPE macroplastics were easy to mobilize since they were less buoyant than PP macroplastics. The HDPE and PP macroplastics were then carried along the lower shear envelope, while escaping the surge wave roller and rising to the free surface after the passage of the surge wave, where the effect of the surge wave roller is lessened. Overall, as the surge wave strength increased, the entertainment of D = 2.54 cm positively buoyant macroplastics in the surge wave roller increased.

4.3 Transport of HDPE and PP varying with macroplastic size

Along with particle density, particle size also plays a crucial role in the transport of the positively buoyant macroplastics. In this section the impact of positively buoyant macroplastic size is explored. To examine this, HDPE and PP macroplastics with a D = 2.54, 1.91, and 1.11 cm were tested in surge wave with Fr_s = 1.40 and 1.70, and visual analysis was performed for macroplastics in Fr_s = 2.00 and 2.30. All the HDPE and PP macroplastics were, to a certain extent, entrained and engaged in the surge wave roller, and demonstrated some degree of vertical motion.

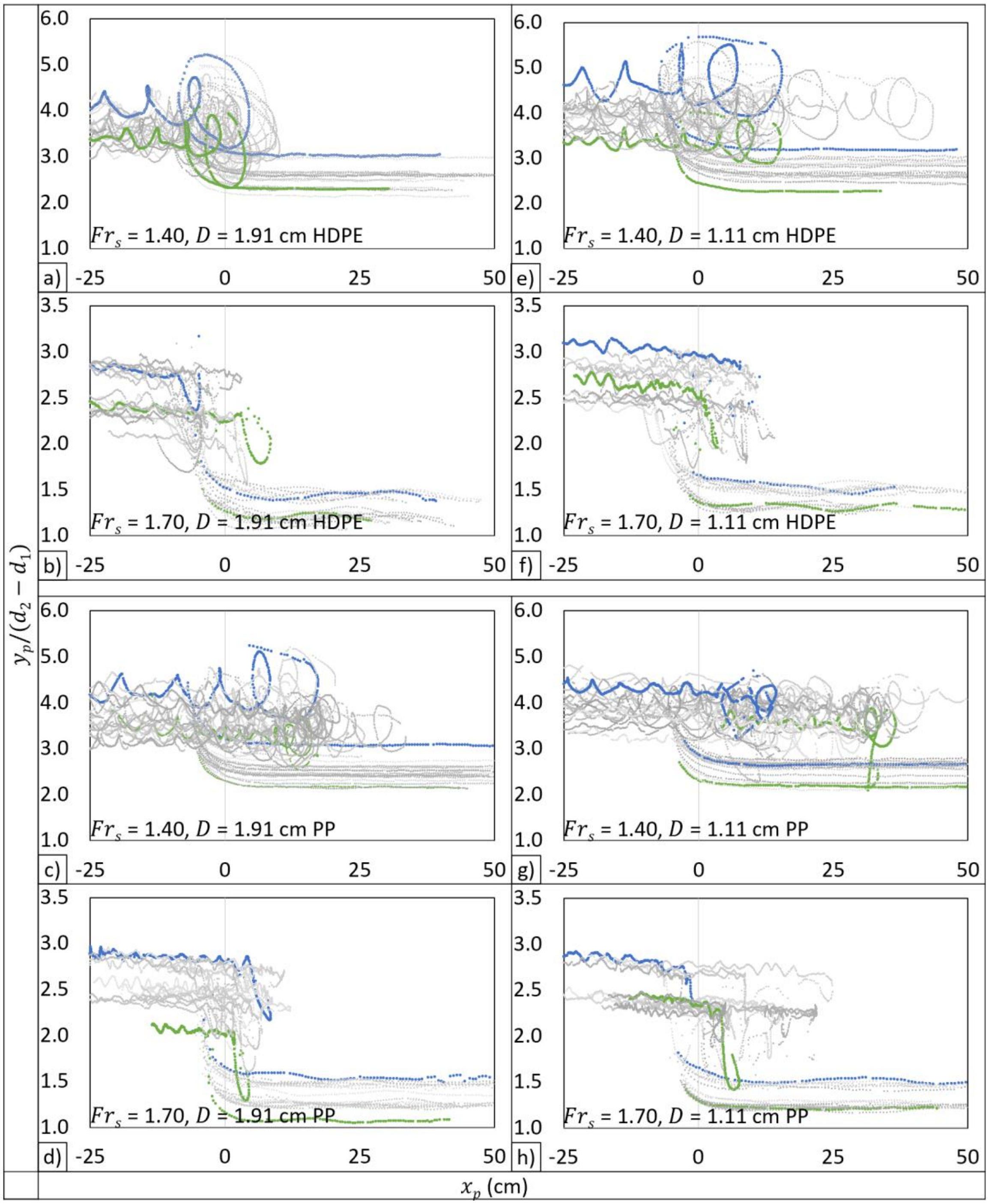

Figure 4-8. Trajectories of D = 1.91 and 1.11 cm HDPE and PP macroplastics. The vertical translation is normalized by surge wave height, $d_2 - d_1$. The x_p represents the horizontal position, which is along the flume bed. The coordinates (0, 1) represent the surge-buoyant macroplastic impact point. The minimum and the maximum vertical transport are denoted by green and blue, respectively. The grey curves represent the other 18 experiments.

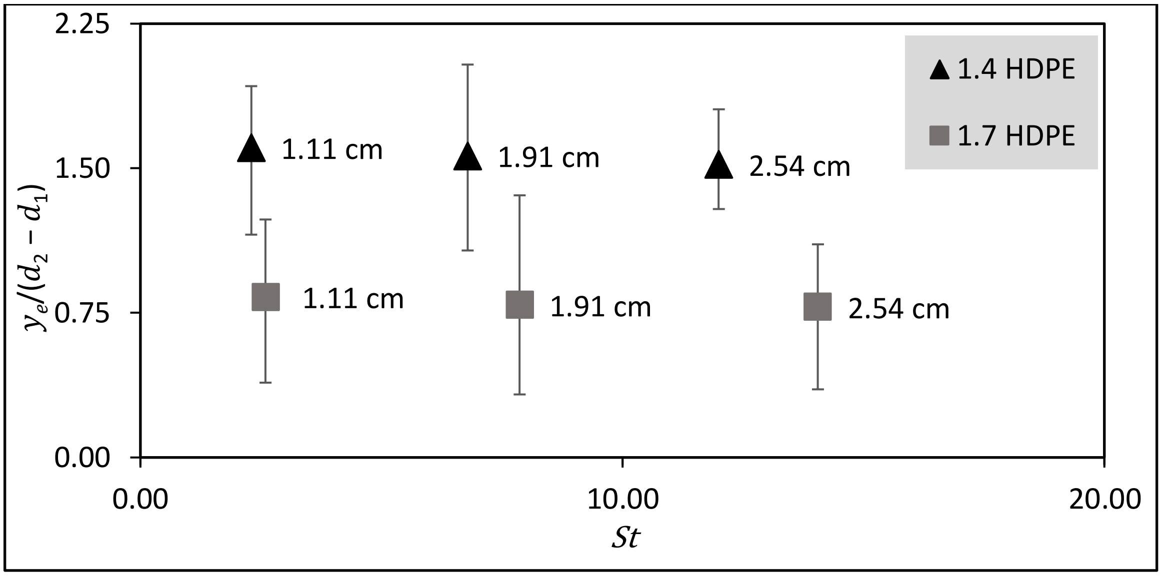

Figure 4-9. Average HDPE macroplastics vertical entrainment range, y_e, normalized by surge height, $d_2 - d_1$. The error bar line shows the minimum and the maximum vertical movement of the 20 runs.

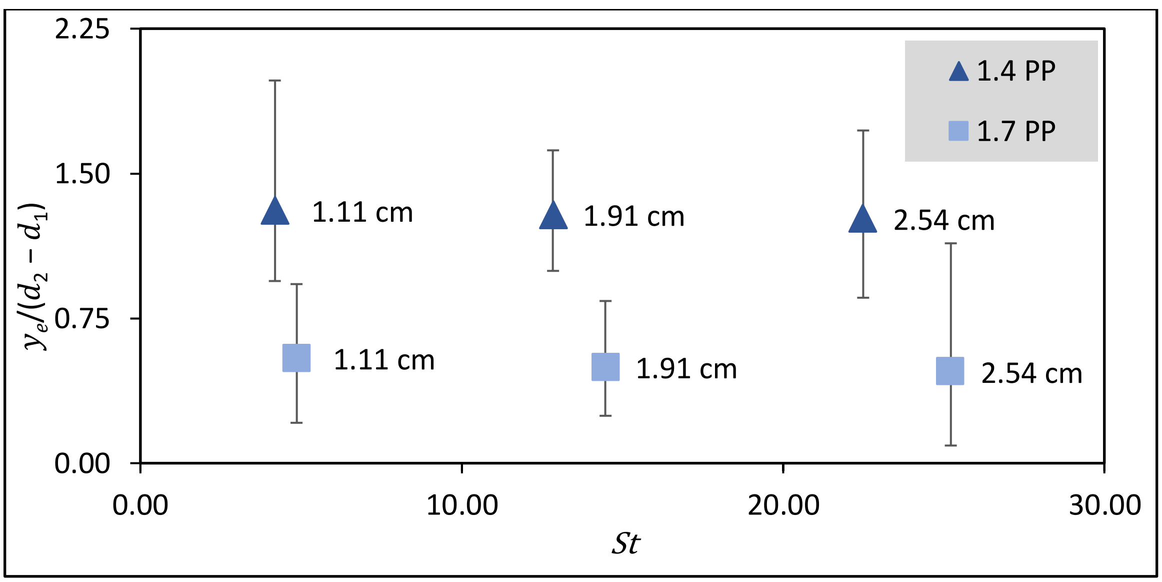

Figure 4-10. Average PP macroplastics vertical entrainment range, y_e, normalized by surge height, $d_2 - d_1$. The error bar line shows the minimum and the maximum vertical movement of the 20 runs.

The undular surge wave had impacted both HDPE and PP macroplastics vertical and horizontal transport. The average vertical translation range of D = 2.54, 1.91, and 1.11 cm

HDPE macroplastics were 1.52, 1.57, and 1.61, respectively (Figure 4-9). The PP macroplastics displayed a similar trend, where the D = 2.54, 1.91, and 1.11 cm macroplastics had an average vertical transport range of 1.27, 1.29, and 1.31, respectively (Figure 4-10). The vertical translation range of both HDPE and PP macroplastics were increasing, as the macroplastics diameter were decreasing, since smaller macroplastics have lower Stokes number (Figure 4-9 and Figure 4-10). Furthermore, all the HDPE macroplastic sizes examined had a higher vertical transport than the corresponding PP macroplastics. Since HDPE macroplastics had lower marginal density than PP, hence lower particle relaxation time and greater entrainment, as suggested by the Stokes number (Figure 4-9 and Figure 4-10). A greater horizontal transport in the upstream direction had occurred as the HDPE macroplastic size decreased, as shown in Figure 4-2 (a) and Figure 4-8 (a) & (e). Correspondingly, as PP macroplastic size was reduced, there was an increase in the horizontal transport in the upstream direction, as shown in Figure 4-2 (c) and Figure 4-8 (c) & (g). In addition to the D = 2.54 cm HDPE and PP macroplastics, the D = 1.91 and 1.11 cm HDPE and PP macroplastics were also closely following the free surface before, across, and after the surge wave (Figure 4-11). Furthermore, the heavier D = 2.54, 1.91, and 1.11 cm HDPE macroplastics had a lower transport in the horizontal direction, compared to PP macroplastics. This was the case since it was easier to transport the lighter PP macroplastics in the upstream direction, as shown in Figure 4-2 (a) & (c), and Figure 4-8 (a), (c), (e), & (g). The overall results show that the macroplastics transport in an undular surge wave was mainly dominated by the Stokes number and free surface behaviour, and marginally influenced by the surge wave. Overall, as the macroplastic size decreased, higher vertical motion range and horizontal transport was observed.

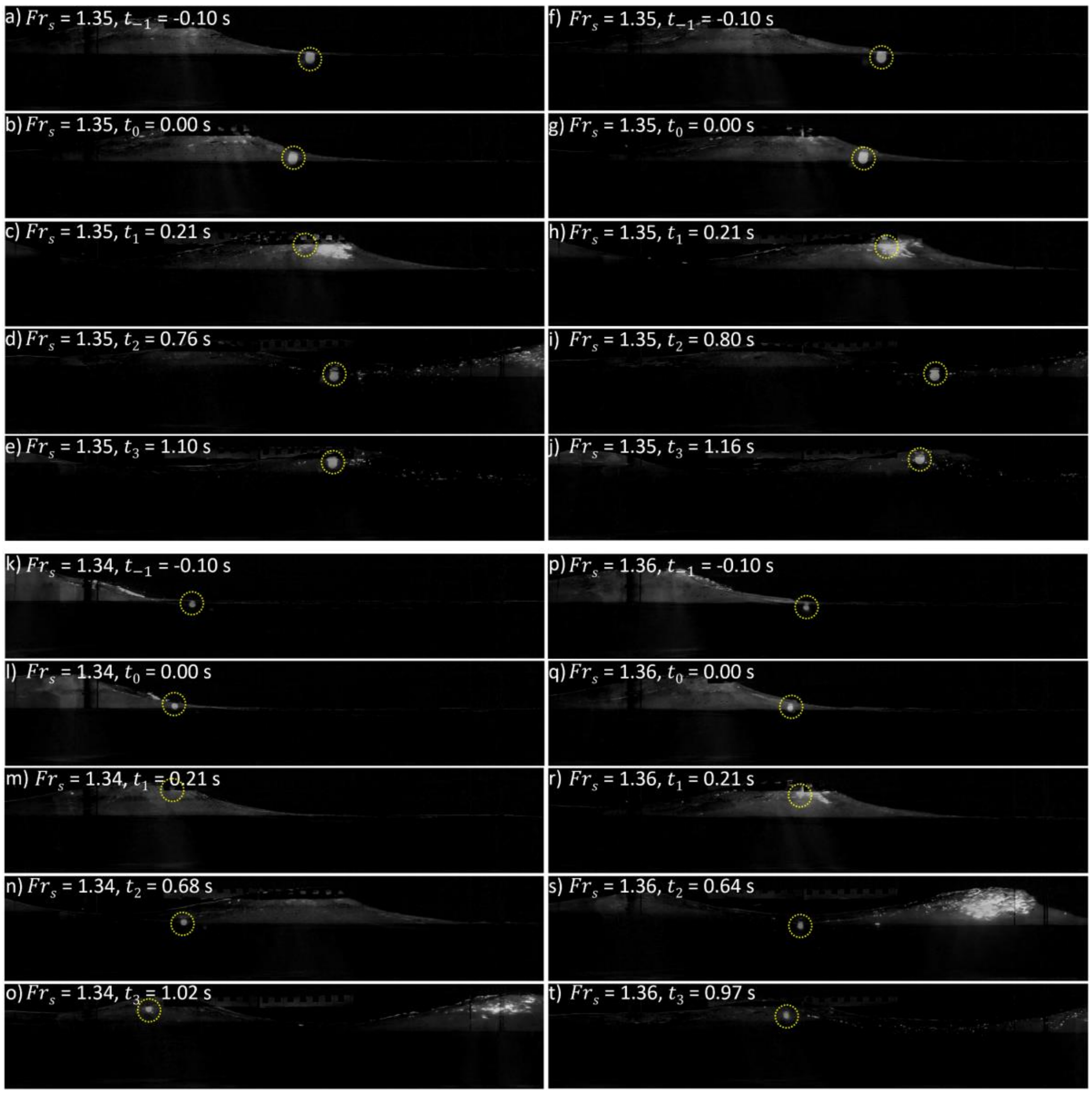

Figure 4-11. Successive frames showing the interaction of: a) – e) D = 1.91 cm HDPE macroplastic in Fr_s = 1.35, f) – j) D = 1.91 cm PP macroplastic in Fr_s = 1.35, k) – o) D = 1.11 cm HDPE macroplastic in Fr_s = 1.34, and p) – t) D = 1.11 cm PP macroplastic in Fr_s = 1.36. Where a), f), k), & p) prior to impact, b), g), l), & q) surge-buoyant macroplastic impact, c), h), m), & r) macroplastic in the undular roller, d), i), n), & s) macroplastic at the first trough, and e), j), o), & t) macroplastic at the crest of the first secondary wave. Surge wave is advancing upstream (left to right).

A similar trend was documented when HDPE and PP macroplastics were studied in Fr_s = 1.70. The average vertical translation range of D = 2.54, 1.91, and 1.11 cm HDPE macroplastics were 0.78, 0.79, and 0.83, respectively (Figure 4-9). Correspondingly, PP macroplastics with a D = 2.54, 1.91, and 1.11 cm moved 0.48, 0.50, and 0.55 in the vertical direction, respectively (Figure 4-10). As macroplastics diameter were decreasing, the vertical transport range for both HDPE and PP macroplastics were increasing, as smaller macroplastics have smaller particle relaxation time and lower Stokes number (Figure 4-9 and Figure 4-10). Similar trend was reported, were the HDPE macroplastics had a greater vertical transport range than the corresponding PP macroplastics, since the lower marginal density of HDPE macroplastics led to a lower particle relaxation time and greater entrainment, as implied by the Stokes number (Figure 4-9 and Figure 4-10). Higher horizontal transport in the upstream direction was observed as the HDPE macroplastics size decreased, as shown in Figure 4-2 (b) and Figure 4-8 (b) & (f). Similarly, PP macroplastics horizontal transport towards the upstream direction also increased, as the macroplastic size decreased, as shown in Figure 4-2 (d) and Figure 4-8 (d) & (h). Additionally, the lighter D = 2.54, 1.91, and 1.11 cm PP macroplastics had a greater transport towards the upstream direction, compared to HDPE macroplastics. Since the higher surge wave celerity was easily able to influence the lighter PP macroplastics in the upstream direction, as shown in Figure 4-2 (b) & (d), and Figure 4-8 (b), (d), (f), & (h). Overall, the occurrence of HDPE and PP macroplastics entrainment across the surge wave, where the macroplastics travel along the developing shear layer, rises to free surface, and then gets entrained behind the surge front was higher (Figure 4-12). Overall, as the macroplastic size decreased, there was an increase in the vertical transport range and in the horizontal transport.

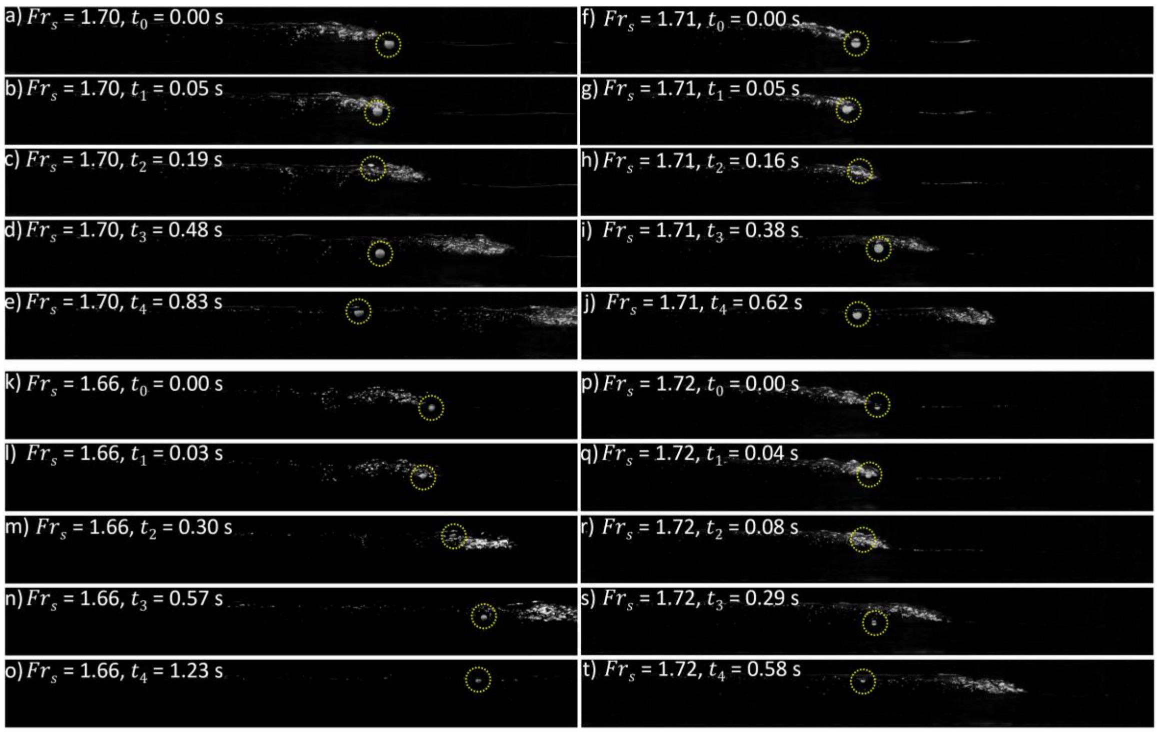

Figure 4-12. Sequential images illustrating the engagement of: a) – e) D = 1.91 cm HDPE macroplastic in Fr_s = 1.70, f) – j) D = 1.91 cm PP macroplastic in Fr_s = 1.71, k) – o) D = 1.11 cm HDPE macroplastic in Fr_s = 1.66, and p) – t) D = 1.11 cm PP macroplastic in Fr_s = 1.72. Where a), f), k), & p) surge-buoyant macroplastic impact, b), g), l), & q) macroplastic along the developing roller, c), h), m), & r) macroplastic entrained in the roller, d), i), n), & s) macroplastic forced down the water column, and e), j), o), & t) macroplastic at free surface. Surge wave is advancing upstream (left to right).

Visual observations were performed for positively buoyant macroplastics when introduced in surge waves with Fr_s = 2.00. As previously observed in the undular surge wave and weak breaking surge wave (Fr_s = 1.40 and 1.70), both HDPE and PP macroplastics were no longer influenced by their buoyancy when engaged in the surge wave. Instead, HDPE and PP macroplastics were moving from the developing mixing layer to entrainment behind the surge front. In addition, the second entrainment process (discussed in the

Section 4.2 for Fr_S = 2.30) was also observed for D = 1.91 and 1.11 cm HDPE and PP macroplastics; where the macroplastics were forced as far as the lower mixing envelope due to the intense breaking of the roller (Figure 4-13). However, the D = 2.54 cm HDPE and PP macroplastics were not carried to the lower mixing envelope, due to the higher initial momentum and the surge wave roller did not have the adequate strength to mobilize larger macroplastics against their buoyancy (Figure 4-6). In addition, as the macroplastic size decreased, higher horizontal transport in the upstream direction was observed.

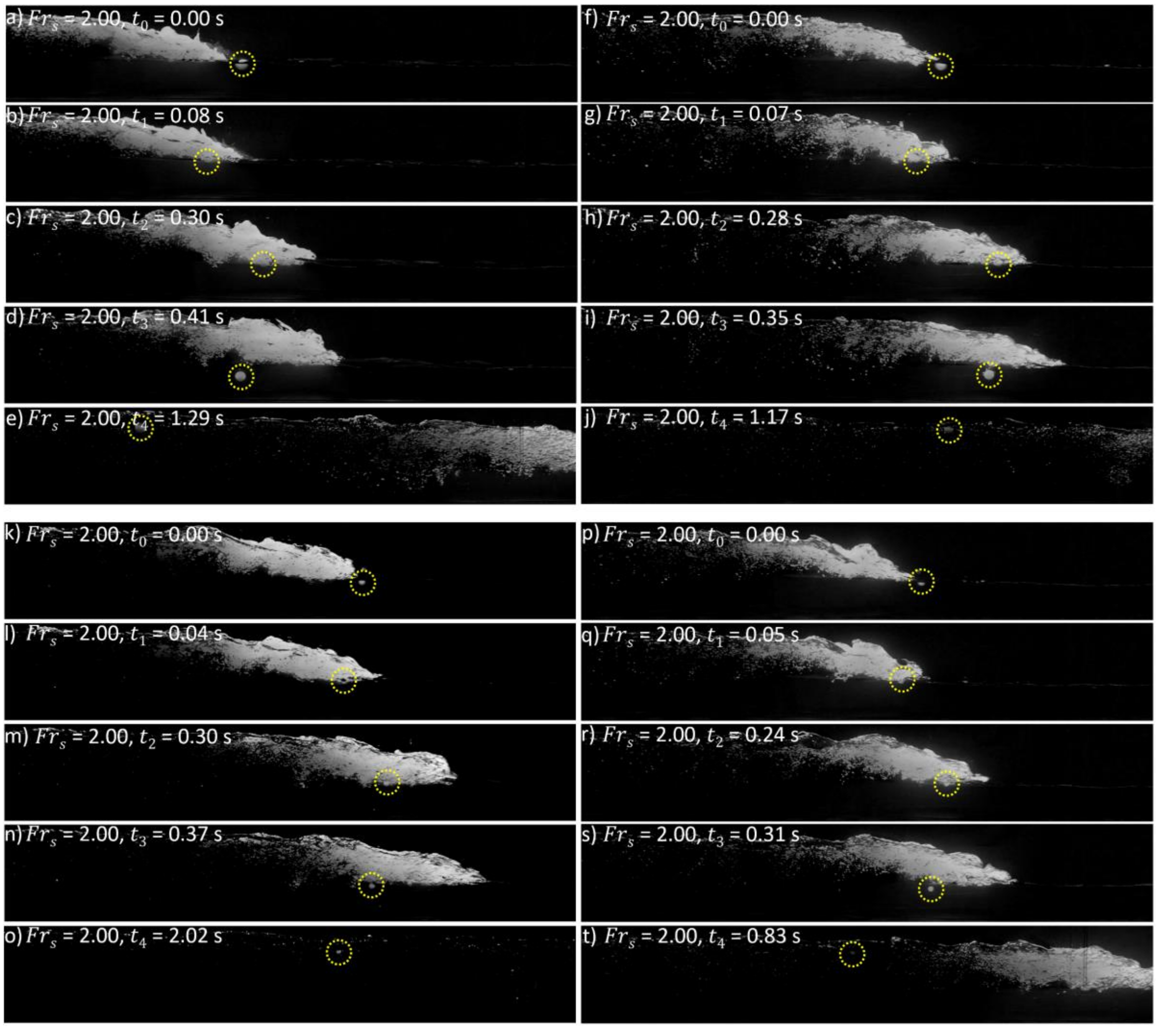

Figure 4-13. Series of frames depicting the transport process of: a) – e) D = 1.91 cm HDPE macroplastic in Fr_s = 2.00, f) – j) D = 1.91 cm PP macroplastic in Fr_s = 2.00, k) – o) D = 1.11 cm HDPE macroplastic in Fr_s = 2.00, and p) – t) D = 1.11 cm PP macroplastic in Fr_s = 2.00. Where a), f), k), & p) surge-buoyant macroplastic impact, b), g), l), & q) macroplastic along the developing roller, c), h), m), & r) macroplastic entrained in the roller, d), i), n), & s) macroplastic forced down the water column, and e), j), o), & t) macroplastic at free surface. Surge wave is advancing upstream (left to right).

At the Fr_s = 2.30, the D = 2.54, 1.91, and 1.11 cm HDPE and PP macroplastics were highly entrained in the aerated roller (Figure 4-7 and Figure 4-14). In all the previously analyzed surge waves with lower surge wave Froude number, Fr_s = 1.40, 1.70, and 2.00, the surge wave roller strength was insufficient in carrying the D = 2.54 cm positively buoyant macroplastics to the lower mixing envelope. However, in addition to D = 1.91, and 1.11 cm macroplastics, the highly turbulent breaking surge wave roller at Fr_s = 2.30, also carried D = 2.54 cm macroplastics to the lower mixing envelope, and in some cases as far to the flume bed (Figure 4-7 & Figure 4-14). Overall, the results suggest that as the strength of the surge wave roller increased, the roller was able to mobilize all the macroplastics against their natural buoyancy and alter its original course. Furthermore, at this surge wave Froude number (2.30), the smaller D = 1.91 and 1.11 cm macroplastics were undergoing the second entrainment process, discussed in the Section 4.2, twice before continuing downstream. This resulted in slight upstream transport when the macroplastics were rising to the free surface behind the sure wave, as shown in Figure 4-14 (e), (k), (q), and (w). Greater horizontal transport towards the upstream direction was observed as the macroplastic size decreased. Higher surge wave strength at this surge wave Froude number can explain the greater transport of macroplastics in the horizontal direction.

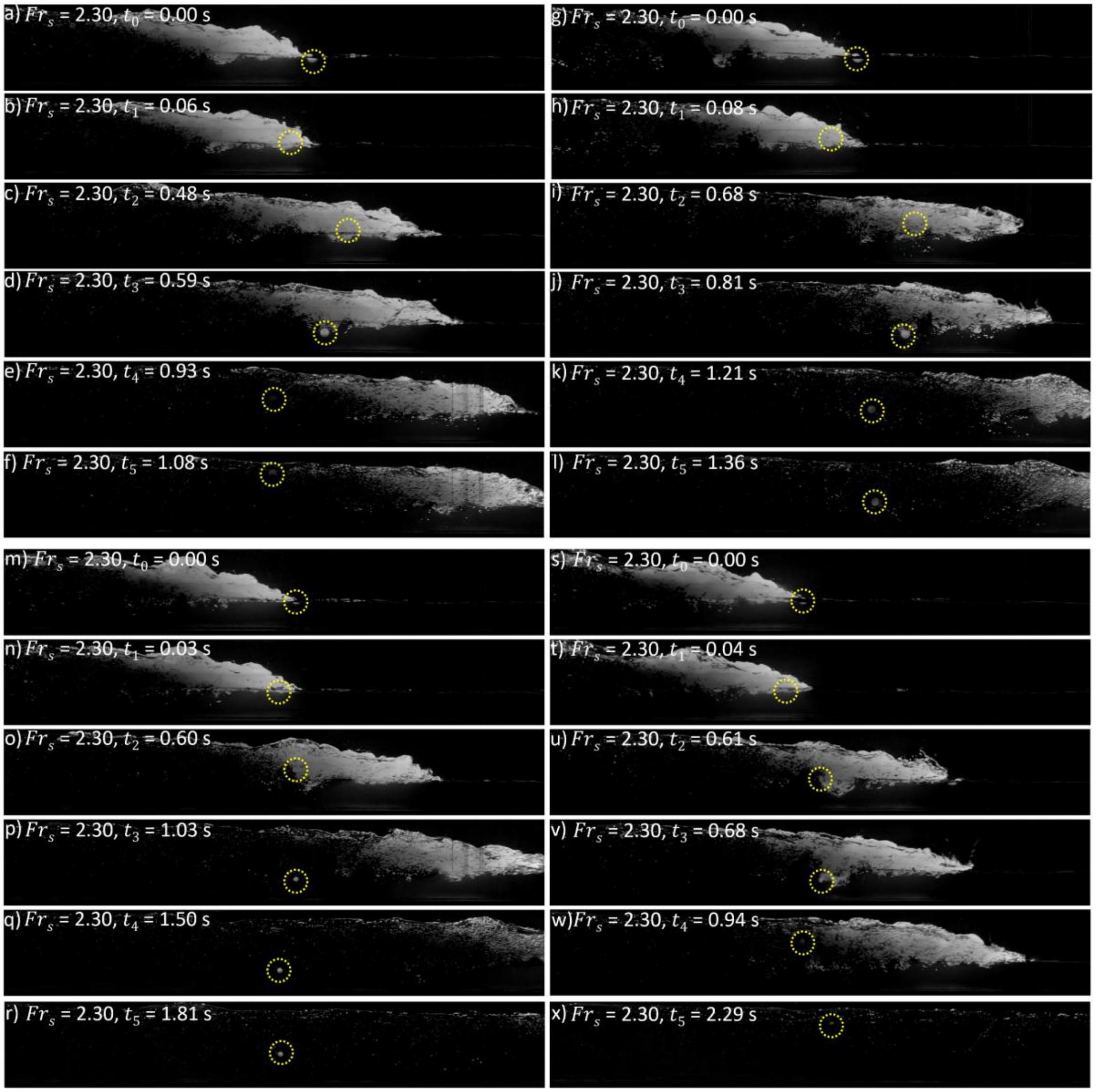

Figure 4-14. Successive frames showing the entrainment of: a) – f) D = 1.91 cm HDPE macroplastic in Fr_s = 2.30, g) – l) D = 1.91 cm PP macroplastic in Fr_s = 2.30, m) – r) D = 1.11 cm HDPE macroplastic in Fr_s = 2.30, and s) – x) D = 1.11 cm PP macroplastic in Fr_s = 2.30. Where a), g), m), & s) surge-buoyant macroplastic impact, b), h), n), & t) macroplastic along the developing mixing layer, c), i), o), & u) macroplastic entrained in the roller, d), j), p), & v) macroplastic forced down the water column, e), k), q), & w) macroplastic advected upstream while rising to the free surface, and f), l), r), & x) macroplastic at free surface. Surge wave is advancing upstream (left to right).

The transport of positively buoyant debris is greatly influenced by the particle size and density. The ability of the surge wave roller to mobilize floating debris against their buoyancy was more evident as the macroplastic size decreased. For undular surge waves (Fr_s = 1.40), the macroplastics transport process was largely dominated by their density and size, since the macroplastics were transported mainly along the free surface. As the surge wave Froude number increased, both HDPE and PP macroplastics had slight entrainment in the surge wave roller, and the smaller macroplastics were more engaged in the surge wave roller. In weak breaking surge waves (Fr_s = 1.70), the influence of the surge wave roller on the transport of HDPE and PP macroplastics was partial, since the macroplastics density also impacted their transport; however, the impact of the surge wave roller was more evident for smaller macroplastics. At the highest surge wave Froude number examined (Fr_s = 2.30), the intense turbulent mixing had considerable impact on the transport of the HDPE and PP macroplastics, across all the macroplastic sizes considered in this study. Both HDPE and PP macroplastics were considerably involved in the breaking of the surge wave roller, and the smallest macroplastics were more influenced by this phenomenon, due to lower particle relaxation time and lower momentum. Indicating that the smaller the debris, easier it was for the surge wave to mobilize them in opposition to their original trajectory. Overall, the velocity perturbation at the surge wave front mobilized positively buoyant HDPE and PP macroplastics, against their natural tendency to float. Stokes number was also a governing factor in the positively buoyant macroplastics vertical entrainment; PP macroplastics with a lower particle relaxation time displayed a lower vertical transport than HDPE macroplastics. In addition, the HDPE and PP macroplastics horizontal transport in the upstream direction also increased as the macroplastics size decreased, due to lower the force required to overcome macroplastics momentum. At last, the HDPE macroplastics had a lower horizontal transport towards the upstream direction, compared to PP macroplastics. As it was easier for the surge wave celerity to move the lighter PP macroplastics in the upstream direction, compared to HDPE macroplastics.

Chapter 5 – Conclusion and Recommendations

5.1 Conclusions

The transport mechanism of negatively buoyant ACR macroplastics and positively buoyant HDPE and PP macroplastics during a surge wave have been investigated. The motive of this thesis was to comprehend and approximate the transport of marine waste in rivers, based on surge wave properties and physical properties of marine waste. The horizontal and vertical transport of various macroplastics have been explored with respect to two parameters: a surge wave Froude number and macroplastic size. The macroplastics polymers considered in this study are amongst the most common polymer types produced worldwide, which have densities marginally lower or higher than the density of ambient fresh water. Results showed that marginal density difference can lead to higher entrainment, while macroplastics with significant density difference may be dominated by their buoyancy.

Stokes number is a dimensionless parameter which defines the ratio of the particle relaxation time to the time scale. The correlation between macroplastics size and density, fluid viscosity, and the density of the ambient fluid was defined by the particle relaxation time. A dimensionless number was used to describe macroplastics behaviour in the flow. Macroplastics with smaller Stokes number have higher time scales or lower particle relaxation times, indicating that the macroplastic will easily be influenced by the flow. Whereas a larger macroplastic with higher Stokes number is associated with lower time scale or greater particle relaxation time, implying that the macroplastic will be less influenced by the flow. Stokes number was also used to define vertical transport of negatively and positively buoyant macroplastics.

A slight reduction and an increase in the horizontal and vertical transport of negatively buoyant macroplastics was observed as the surge wave Froude number, macroplastic size, and Stokes number changed. The horizontal transport of ACR macroplastics was influenced by impulse, mixing cone, and their initial momentum. The force from the surge wave applied on ACR macroplastics occurred over a longer time interval due to the extended mixing cone length behind the surge wave. This resulted in the deceleration of ACR macroplastics and changed their direction. For Fr_S = 1.40, 1.70, and 2.00, the combination of prolonged mixing cone length and lower initial momentum of ACR macroplastics allowed sufficient time to alter ACR macroplastics horizontal transport, across all sizes. Conversely, the surge wave strength at Fr_S = 2.30 and 2.65 led to a higher initial momentum of ACR macroplastics, stronger transient recirculation, and much a wider mixing layer envelope and shorter mixing cone length, which resulted in sustained downstream transport of ACR macroplastics. An overall decrease in macroplastics size resulted in higher horizontal transport in the upstream direction for Fr_S = 1.40, 1.70, and 2.00, and lower horizontal transport in the downstream direction for Fr_S = 2.30 and 2.65. As it was easier to mobilize smaller macroplastics due to lower initial momentum. Macroplastics size and surge wave strength also influenced the vertical transport of ACR macroplastics. Higher surge wave Froude number led to greater turbulent kinetic energy, which increased the vertical drag on the ACR macroplastics, overpowering the gravitational force; resulting in higher vertical transport as surge wave Froude number increased, and further vertical transport as macroplastics size decreased.

Similar to negatively buoyant macroplastics (i.e. ACR), a change in the horizontal and vertical movement of positively buoyant macroplastics (i.e. PP and HDPE) was documented as the surge wave Froude number, macroplastic size, and Stokes number changed. The transport of positively buoyant macroplastics were influenced by celerity, free surface behaviour, and vertical drag on macroplastics. When Fr_S = 1.40, positively buoyant macroplastics trajectory were marginally influenced by the surge wave roller strength, and largely dominated by the surge wave celerity and free surface behaviour. This led to higher horizontal transport of HDPE and PP macroplastics in the upstream direction when compared to Fr_S = 1.70. Furthermore, repetitive upstream bound motion due to the secondary wave undulations at Fr_S = 1.40 also contributed to higher upstream transport. Additionally, as the macroplastics size decreased, higher horizontal transport was observed, since smaller macroplastics are easier to mobilize. The vertical drag on both the HDPE and PP macroplastics resulted in considerable entrainment at the surge wave roller and macroplastics were carried along the water column, all against their natural tendency to float. The entrainment of HDPE and PP macroplastics increased as surge wave Froude number increased, resulting in higher vertical transport. The vertical transport range for both HDPE and PP macroplastics increased as the macroplastics size decreased, since macroplastics with lower Stokes number are easily entrained in the flow. Moreover, all the

HDPE macroplastic sizes examined displayed higher vertical transport than the corresponding PP macroplastics. Since HDPE macroplastics had lower marginal density than that of PP, leading to a lower particle relaxation time or higher time scale, increasing the entrainment of HDPE macroplastics.

5.2 Contributions

This research expanded the current state of knowledge on the transport of macroplastics, surge wave capacity, and implementation of particle tracking velocimetry (PTV). Contributions from this research to the state of knowledge include:

1. This is the first study to investigate surge capacity and macroplastics transport in surge waves based on numerous parameters (i.e., surge wave height, surge wave Froude number, surge wave celerity, and macroplastics properties) using particle tracking velocimetry.
2. The effect of macroplastics size and density was studied for a wide range of Froude numbers. The results highlight the differences and similarities in macroplastics horizontal and vertical transport across surge wave with a wide range of surge wave Froude number (undular, weak, and breaking surge waves).
3. The vertical transport of negatively buoyant macroplastics results provide insight into how negatively buoyant macroplastics behave compared with positively buoyant macroplastics at higher surge wave Froude number.

4. Entrainment of positively buoyant macroplastics have been observed and quantified. This research presented the first evidence of two distinct process of how positively buoyant macroplastics escape the highly turbulent surge wave.
5. This research also greatly contributes to the implementation of inexpensive in-house experimental setup of open-source PTV platform. The novelty of this experimental procedure may encourage the exploration and adoption of in-house PTV program, to evaluate particles' transport and trajectories. Furthermore, this study will also motivate the limitations of open-source PTV platforms to be addressed.

5.3 Recommendations for future work

This section discusses recommendations to improve and expand upon the contributions of this thesis.

Experimental limitations

Several experimental limitations should be considered in future studies: a wider range of macroplastic size and shapes, digitalising gate closure and macroplastics release mechanism for repeatability, interaction of several macroplastics in a surge wave, the effect of bed friction, and a wider range of surge wave Froude number.

Image processing

The macroplastics entrainment in the surge wave occurs in a 3D space. However, in the current experiments a camera with a 2D standard lens was used to capture the transport. A multi-camera setup up or a secondary camera, mounted on top of the flume should consider the 3D aspect of macroplastic transport.

Particle tracking velocimetry

Particle tracking was solely based on image processing. Significant aeration induced at higher surge wave Froude number masked macroplastics, and hindered PTV platform from tracking. A new method of tracking should be established to minimize these limitations. For example, deploying 3D position tracking, where retroreflective markers are applied on the macroplastics, and cameras are employed which can track retroreflective markers would be a useful addition to this work. Improved tracking methods can facilitate in tracking all shapes of macroplastics in 3D.

Post processing and calculations

Automating the calculation of surge wave Froude number from the acoustic displacement sensors, and the process of linking each test run with its corresponding surge wave Froude number could be improved. Furthermore, macroplastics density should be experimentally determined since an average density range was used in this study. Finally, a second camera on the top of the flume should be considered for investigating macroplastics transport along the channel width.

References

Adimey, N. M., Hudak, C. A., Powell, J. R., Bassos-Hull, K., Foley, A., Farmer, N. A., White, L., & Minch, K. (2014). Fishery gear interactions from stranded bottlenose dolphins, Florida manatees and sea turtles in Florida, U.S.A. *Marine Pollution Bulletin*, *81*(1), 103–115. https://doi.org/10.1016/j.marpolbul.2014.02.008

Aksit, M., Zhao, C., Klose, B., Kreger, K., Schmidt, H. W., & Altstädt, V. (2019). Extruded polystyrene foams with enhanced insulation and mechanical properties by a benzene-trisamide-based additive. *Polymers*, *11*(2), 268. https://doi.org/10.3390/polym11020268

Al-Zawaidah, H., Ravazzolo, D., & Friedrich, H. (2021). Macroplastics in rivers: Present knowledge, issues and challenges. *Environmental Science: Processes and Impacts*, *23(4)*, 535–552. https://doi.org/10.1039/d0em00517g

Athapaththu, A. M. A. I. K., Thushari, G. G. N., Dias, P. C. B., Abeygunawardena, A. P., Egodauyana, K. P. U. T., Liyanage, N. P. P., Pitawala, H. M. J. C., & Senevirathna, J. D. M. (2020). Plastics in surface water of southern coastal belt of Sri Lanka (Northern Indian Ocean): Distribution and characterization by FTIR. *Marine Pollution Bulletin*, *161*(A), 111750. https://doi.org/10.1016/j.marpolbul.2020.111750

Banks, J., & Bressloff, N. W. (2007). Turbulence modeling in three-dimensional stenosed arterial bifurcations. *Journal of Biomechanical Engineering*, *129*(1), 40–50. https://doi.org/10.1115/1.2401182

Barnes, D. K. A., Walters, A., & Gonçalves, L. (2010). Macroplastics at sea around Antarctica. *Marine Environmental Research*, *70*(2), 250–252. https://doi.org/10.1016/j.marenvres.2010.05.006

Benjamins, S., Ledwell, W., Huntington, J., & Davidson, A. R. (2012). Assessing changes in numbers and distribution of large whale entanglements in Newfoundland and Labrador, Canada. *Marine Mammal Science*, *28*(3), 579-601. https://doi.org/10.1111/j.1748-7692.2011.00511.x

Bergmann, M., Wirzberger, V., Krumpen, T., Lorenz, C., Primpke, S., Tekman, M. B., & Gerdts, G. (2017). High Quantities of Microplastic in Arctic Deep-Sea Sediments from the HAUSGARTEN Observatory. *Environmental Science and Technology*, *51*(19), 11000–11010. https://doi.org/10.1021/acs.est.7b03331

Besseling, E., Foekema, E. M., van Franeker, J. A., Leopold, M. F., Kühn, S., Bravo Rebolledo, E. L., Heße, E., Mielke, L., IJzer, J., Kamminga, P., & Koelmans, A. A. (2015). Microplastic in a macro filter feeder: Humpback whale Megaptera novaeangliae. *Marine Pollution Bulletin*, *95*(1), 248–252. https://doi.org/10.1016/j.marpolbul.2015.04.007

Bjerregaard, M. (2010). *MSB/UNDP Debris Management Guidelines, Disaster Waste Recovery*. Swedish International Development Cooperated Agency, Lebanon. Retrieved November 1, 2021, from https://www.sheltercluster.org/sites/default/files/docs/Debris%20Management%20Guidelines%202010.pdf

Blettler, M. C. M., Garello, N., Ginon, L., Abrial, E., Espinola, L. A., & Wantzen, K. M. (2019). Massive plastic pollution in a mega-river of a developing country: Sediment deposition and ingestion by fish (Prochilodus lineatus). *Environmental Pollution*, *255*, 113348. https://doi.org/10.1016/j.envpol.2019.113348

Blettler, M. C. M., Ulla, M. A., Rabuffetti, A. P., & Garello, N. (2017). Plastic pollution in freshwater ecosystems: macro-, meso-, and microplastic debris in a floodplain lake. *Environmental Monitoring and Assessment*, *189*(11), 1–13. https://doi.org/10.1007/s10661-017-6305-8

Boerger, C. M., Lattin, G. L., Moore, S. L., & Moore, C. J. (2010). Plastic ingestion by planktivorous fishes in the North Pacific Central Gyre. *Marine Pollution Bulletin*, *60*(12), 2275–2278. https://doi.org/10.1016/j.marpolbul.2010.08.007

Bond, A. L., Provencher, J. F., Elliot, R. D., Ryan, P. C., Rowe, S., Jones, I. L., Robertson, G. J., & Wilhelm, S. I. (2013). Ingestion of plastic marine debris by Common and Thick-billed Murres in the northwestern Atlantic from 1985 to 2012. *Marine Pollution Bulletin*, *77*(1–2), 192–195. https://doi.org/10.1016/j.marpolbul.2013.10.005

Bravo Rebolledo, E. L., van Franeker, J. A., Jansen, O. E., & Brasseur, S. M. J. M. (2013). Plastic ingestion by harbour seals (Phoca vitulina) in The Netherlands. *Marine Pollution Bulletin*, *67*(1–2), 200–202. https://doi.org/10.1016/j.marpolbul.2012.11.035

Britannica. (2021). Indian Ocean tsunami of 2004. In *Encyclopedia Britannica*. Retrieved March 27, 2021, from https://www.britannica.com/event/Indian-Ocean-tsunami-of-2004

Browne, M. A., Dissanayake, A., Galloway, T. S., Lowe, D. M., & Thompson, R. C. (2008). Ingested microscopic plastic translocates to the circulatory system of the mussel, Mytilus edulis (L.). *Environmental Science and Technology*, *42*(13), 5026–5031. https://doi.org/10.1021/es800249a

Bugoni, L., Â Gia Krause, L., & VIRGI Â NIA PETRYà, M. (2001). Marine Debris and Human Impacts on Sea Turtles in Southern Brazil. *Marine Pollution Bulletin*, *42*(12), 1330–1334. https://doi.org/10.1016/S0025-326X(01)00147-3

Chanson, H. (2010a). Undular tidal bores: Basic theory and free-surface characteristics. *Journal of Hydraulic Engineering*, *136*(11), 940–944. https://doi.org/10.1061/(ASCE)HY.1943-7900.0000264

Chanson, H. (2010b). Unsteady turbulence in tidal bores: Effects of bed roughness. *Journal of Waterway, Port, Coastal and Ocean Engineering*, *136*(5), 247–256. https://doi.org/10.1061/(ASCE)WW.1943-5460.0000048

Chanson, H. (2011). Turbulent shear stresses in hydraulic jumps, bores and decelerating surges. *Earth Surface Processes and Landforms*, *36*(2), 180–189. https://doi.org/10.1002/esp.2031

Chanson, H., & Lubin, P. (2013). Mixing and Sediment Processes induced by Tsunamis propagating Upriver. In *Tsunamis: Economic Impact, Disaster Management and Future Challenges*, 65–102. Nova Science Publishers.

Chiu, S. Y., Chiu, C. C., & Xu, S. S. D. (2018). A background subtraction algorithm in complex environments based on category entropy analysis. *Applied Sciences*, *8*(6), 885. https://doi.org/10.3390/app8060885

Choy, C. A., Robison, B. H., Gagne, T. O., Erwin, B., Firl, E., Halden, R. U., Hamilton, J. A., Katija, K., Lisin, S. E., Rolsky, C., & S. Van Houtan, K. (2019). The vertical distribution and biological transport of marine microplastics across the epipelagic and mesopelagic water column. *Scientific Reports*, *9*(1), 1–9. https://doi.org/10.1038/s41598-019-44117-2

Chua, E. M., Shimeta, J., Nugegoda, D., Morrison, P. D., & Clarke, B. O. (2014). Assimilation of polybrominated diphenyl ethers from microplastics by the marine amphipod, allorchestes compressa. *Environmental Science and Technology*, *48*(14), 8127–8134. https://doi.org/10.1021/es405717z

Chubarenko, I., Bagaev, A., Zobkov, M., & Esiukova, E. (2016). On some physical and dynamical properties of microplastic particles in marine environment. *Marine Pollution Bulletin*, *108*(1–2), 105–112. https://doi.org/10.1016/j.marpolbul.2016.04.048

Colabuono, F. I., Barquete, V., Domingues, B. S., & Montone, R. C. (2009). Plastic ingestion by Procellariiformes in Southern Brazil. *Marine Pollution Bulletin*, *58*(1), 93–96. https://doi.org/10.1016/j.marpolbul.2008.08.020

Cózar, A., Echevarría, F., González-Gordillo, J. I., Irigoien, X., Úbeda, B., Hernández-León, S., Palma, Á. T., Navarro, S., García-de-Lomas, J., Ruiz, A., Fernández-de-Puelles, M. L., & Duarte, C. M. (2014). Plastic debris in the open ocean. *Proceedings of the National Academy of Sciences of the United States of America*, *111*(28), 10239–10244. https://doi.org/10.1073/pnas.1314705111

Cózar, A., Martí, E., Duarte, C. M., García-De-Lomas, J., van Sebille, E., Ballatore, T. J., Eguíluz, V. M., González-Gordillo, J. I., Pedrotti, M. L., Echevarría, F., Troublè, R., & Irigoien, X. (2017). The Arctic Ocean as a dead end for floating plastics in the North Atlantic branch of the Thermohaline Circulation. *Science Advances*, *3*(4). https://doi.org/10.1126/sciadv.1600582

Dalu, T., Malesa, B., & Cuthbert, R. N. (2019). Assessing factors driving the distribution and characteristics of shoreline macroplastics in a subtropical reservoir. *The Science of the Total Environment*, *696*, 133992. https://doi.org/10.1016/j.scitotenv.2019.133992

Davison, P., & Asch, R. G. (2011). Plastic ingestion by mesopelagic fishes in the North Pacific Subtropical Gyre. *Marine Ecology Progress Series*, *432*, 173–180. https://doi.org/10.3354/meps09142

Derraik, B. (2002). The pollution of the marine environment by plastic debris: a review. *Marine Pollution Bulletin*, *44*(9), 842–852. https://doi.org/https://doi.org/10.1016/S0025-326X(02)00220-5

Dey, S., Ali, S. Z., & Padhi, E. (2019). Terminal fall velocity: The legacy of Stokes from the perspective of fluvial hydraulics. *Proceedings of the Royal Society A*, *475*(2228). https://doi.org/10.1098/rspa.2019.0277

Di-Méglio, N., & Campana, I. (2017). Floating macro-litter along the Mediterranean French coast: Composition, density, distribution and overlap with cetacean range. *Marine Pollution Bulletin*, *118*(1–2), 155–166. https://doi.org/10.1016/j.marpolbul.2017.02.026

Ellen MacArthur Foundation. (2016). *The New Plastics Economy: Rethinking the future of plastics*. The World Economic Forum. Retrieved June 30, 2020, from https://www3.weforum.org/docs/WEF_The_New_Plastics_Economy.pdf

Eriksen, M., Lebreton, L. C. M., Carson, H. S., Thiel, M., Moore, C. J., Borerro, J. C., Galgani, F., Ryan, P. G., & Reisser, J. (2014). Plastic Pollution in the World's Oceans: More than 5 Trillion Plastic Pieces Weighing over 250,000 Tons Afloat at Sea. *PLoS ONE*, *9*(12), e111913. https://doi.org/10.1371/journal.pone.0111913

Erni-Cassola, G., Zadjelovic, V., Gibson, M. I., & Christie-Oleza, J. A. (2019). Distribution of plastic polymer types in the marine environment; A meta-analysis. *Journal of Hazardous Materials*, *369*, 691–698. https://doi.org/10.1016/j.jhazmat.2019.02.067

Forrest, A. K., & Hindell, M. (2018). Ingestion of plastic by fish destined for human consumption in remote South Pacific Islands. *Australian Journal of Maritime and Ocean Affairs*, *10*(2), 81–97. https://doi.org/10.1080/18366503.2018.1460945

Fuji TV official. (2013). *"The Untold Stories of the Tsunami in Japan -March 11, 2011-"wins Peabody Awards 2012 [Video]*. YouTube. https://www.youtube.com/watch?v=ULCheNmNxYI

Gasperi, J., Dris, R., Bonin, T., Rocher, V., & Tassin, B. (2014). Assessment of floating plastic debris in surface water along the Seine River. *Environmental Pollution*, *195*, 163–166. https://doi.org/10.1016/j.envpol.2014.09.001

GESAMP. (2016). *Sources, fate and effects of microplastics in the marine environment: part 2 of a global assessment.* Reports and Studies 93 IMO/FAO/Unesco-IOC/WMO/IAEA/UN/UNEP Joint Group of Experts on the Scientific Aspects of Marine Environmental Protection. Retrieved June 30, 2020, from *http://www.gesamp.org/site/assets/files/1275/sources-fate-and-effects-of-microplastics-in-the-marine-environment-part-2-of-a-global-assessment-en.pdf*

Geyer, R., Jambeck, J. R., & Law, K. L. (2017). Production, use, and fate of all plastics ever made. *Science Advances*, *3*(7), 25–29. https://doi.org/10.1126/sciadv.1700782

Gharib, M., Kremers, D., Koochesfahani, M., & Kemp, M. (2002). Leonardo's vision of flow visualization. *Experiments in Fluids*, *33*(1), 219–223. https://doi.org/10.1007/s00348-002-0478-8

Gómez, V., Pozo, K., Nuñez, D., Přibylová, P., Audy, O., Baini, M., Fossi, M. C., & Klánová, J. (2020). Marine plastic debris in Central Chile: Characterization and abundance of macroplastics and burden of persistent organic pollutants (POPs). *Marine Pollution Bulletin*, *152*, 110881. https://doi.org/10.1016/j.marpolbul.2019.110881

Greg Hofmeyr, G. J., Bester, M. N., Kirkman, S. P., Lydersen, C., & Kovacs, K. M. (2006). Entanglement of Antarctic fur seals at Bouvetøya, Southern Ocean. *Marine Pollution Bulletin*, *52*(9), 1077–1080. https://doi.org/10.1016/j.marpolbul.2006.05.003

Gregory, M. R. (2009). Environmental implications of plastic debris in marine settings-entanglement, ingestion, smothering, hangers-on, hitch-hiking and alien invasions. *Philosophical Transactions of the Royal Society B: Biological Sciences*, *364*(1526), 2013–2025. https://doi.org/10.1098/rstb.2008.0265

Gregory, M. R., & Ryan, P. G. (1997). Pelagic Plastics and Other Seaborne Persistent Synthetic Debris: A Review of Southern Hemisphere Perspectives. In J.M. Coe, & D.B. Rogers (eds), *Marine debris*, 49–66. Springer Series on Environmental Management. Springer. https://doi.org/https://doi.org/10.1007/978-1-4613-8486-1_6

Harper, C. A., & Petrie, E. M. (2003). *Plastics materials and processes: a concise encyclopedia*. John Wiley & Sons. https://doi.org/10.1002/0471459216

Hartmann, N. B., Hüffer, T., Thompson, R. C., Hassellöv, M., Verschoor, A., Daugaard, A. E., Rist, S., Karlsson, T., Brennholt, N., Cole, M., Herrling, M. P., Hess, M. C., Ivleva, N. P., Lusher, A. L., & Wagner, M. (2019). Are We Speaking the Same Language? Recommendations for a Definition and Categorization Framework for Plastic Debris.

Environmental Science and Technology, *53*(3), 1039–1047. https://doi.org/10.1021/acs.est.8b05297

Isobe, A., Kubo, K., Tamura, Y., Kako, S., Nakashima, E., & Fujii, N. (2014). Selective transport of microplastics and mesoplastics by drifting in coastal waters. *Marine Pollution Bulletin*, *89*(1–2), 324–330. https://doi.org/10.1016/j.marpolbul.2014.09.041

Jambeck, J. R., Geyer, R., Wilcox, C., Siegler, T. R., Perryman, M., Andrady, A., Narayan, R., & Law, K. L. (2015). Plastic waste inputs from land into the ocean. *Science*, *347*(6223), 768–771. https://doi.org/10.1126/science.1260352

Jiménez, S., Domingo, A., Brazeiro, A., Defeo, O., & Phillips, R. A. (2015). Marine debris ingestion by albatrosses in the southwest Atlantic Ocean. *Marine Pollution Bulletin*, *96*(1–2), 149–154. https://doi.org/10.1016/j.marpolbul.2015.05.034

John P. Rafferty, & Kenneth Pletcher. (2021). Japan earthquake and tsunami of 2011. In *Encyclopedia Britannica*. Retrieved November 1, 2021, from https://www.britannica.com/event/Japan-earthquake-and-tsunami-of-2011

Kane, I. A., & Clare, M. A. (2019). Dispersion, accumulation, and the ultimate fate of microplastics in deep-marine environments: A review and future directions. *Frontiers in Earth Science*, *7*, 80. https://doi.org/10.3389/feart.2019.00080

Kane, I. A., Clare, M. A., Miramontes, E., Wogelius, R., Rothwell, J. J., Garreau, P., & Pohl, F. (2020). Seafloor microplastic hotspots controlled by deep-sea circulation. *Science*, *368*(6495), 1140–1145. https://doi.org/10.1126/science.aba5899

Karimpour, S., & Chu, V. H. (2016). Instability of unbounded transverse mixing layer in shallow waters. *Canadian Journal of Civil Engineering*, *43*(6), 504–510. https://doi.org/https://doi.org/10.1139/cjce-2016-0018

Karimpour, S., & Chu, V. H. (2019). The role of waves on mixing in shallow waters. *Canadian Journal of Civil Engineering*, *46*(2), 134–147. https://doi.org/10.1139/cjce-2017-0311

Kawanisi, K., & Shiozaki, R. (2008). Turbulent Effects on the Settling Velocity of Suspended Sediment. *Journal of Hydraulic Engineering*, *134*(2), 261–266. https://doi.org/10.1061/ASCE0733-94292008134:2261

Knoblauch, H. (1999). *Overview of density flows and turbidity currents*. Water Resources Research Laboratory, United States Bureau of Reclamation. Retrieved October 21, 2020, from https://www.usbr.gov/tsc/techreferences/hydraulics_lab/pubs/PAP/PAP-0816.pdf

Knowlton, A. R., Hamilton, P. K., Marx, M. K., Pettis, H. M., & Kraus, S. D. (2012). Monitoring North Atlantic right whale Eubalaena glacialis entanglement rates: A 30 yr retrospective. *Marine Ecology Progress Series*, *466*, 293–302. https://doi.org/10.3354/meps09923

Koch, C., & Chanson, H. (2008). Turbulent Mixing beneath an Undular Bore Front. *Journal of Coastal Research*, *24*(4), 999–1007. https://doi.org/10.2112/06-0688.1

Koelmans, A. A., Kooi, M., Law, K. L., & van Sebille, E. (2017). All is not lost: Deriving a top-down mass budget of plastic at sea. *Environmental Research Letters*, *12*(11), 114028. https://doi.org/10.1088/1748-9326/aa9500

Kooi, M., van Nes, E. H., Scheffer, M., & Koelmans, A. A. (2017). Ups and Downs in the Ocean: Effects of Biofouling on Vertical Transport of Microplastics. *Environmental Science and Technology*, *51*(14), 7963–7971. https://doi.org/10.1021/acs.est.6b04702

Kornei, K. (2017). Plastic makes up nearly 70% of all ocean litter. *Science*. https://doi.org/10.1126/science.aal0998

Kosuth, M., Mason, S. A., & Wattenberg, E. v. (2018). Anthropogenic contamination of tap water, beer, and sea salt. *PLoS ONE*, *13*(4), 1–18. https://doi.org/10.1371/journal.pone.0194970

Kühn, S., Bravo Rebolledo, E. L., & van Franeker, J. A. (2015). Deleterious Effects of Litter on Marine Life. In M. Bergmann, L. Gutow, & M. Klages (Eds.), *Marine Anthropogenic Litter*, 76–116. Springer, Cham https://doi.org/DOI 10.1007/978-3-319-16510-3_4

Lahens, L., Strady, E., Kieu-Le, T. C., Dris, R., Boukerma, K., Rinnert, E., Gasperi, J., & Tassin, B. (2018). Macroplastic and microplastic contamination assessment of a tropical river (Saigon River, Vietnam) transversed by a developing megacity. *Environmental Pollution*, *236*, 661–671. https://doi.org/10.1016/j.envpol.2018.02.005

Laist, D. W. (1997). Impacts of Marine Debris: Entanglement of Marine Life in Marine Debris Including a Comprehensive List of Species with Entanglement and Ingestion

Records. In J.M. Coe, & D.B. Rogers (eds), *Marine debris*, 99–139. Springer Series on Environmental Management. Springer. https://doi.org/10.1007/978-1-4613-8486-1_10

Law, K. L., Morét-Ferguson, S., Maximenko, N. A., Proskurowski, G., Peacock, E. E., Hafner, J., & Reddy, C. M. (2010). Plastic Accumulation in the North Atlantic Subtropical Gyre. *Science*, *329*(5996), 1185–1188. https://www.science.org/doi/10.1126/science.1192321

Lebreton, L. C. M., van der Zwet, J., Damsteeg, J. W., Slat, B., Andrady, A., & Reisser, J. (2017). River plastic emissions to the world's oceans. *Nature Communications*, *8*(1), 1–10. https://doi.org/10.1038/ncomms15611

Lebreton, L., Slat, B., Ferrari, F., Sainte-Rose, B., Aitken, J., Marthouse, R., Hajbane, S., Cunsolo, S., Schwarz, A., Levivier, A., Noble, K., Debeljak, P., Maral, H., Schoeneich-Argent, R., Brambini, R., & Reisser, J. (2018). Evidence that the Great Pacific Garbage Patch is rapidly accumulating plastic. *Scientific Reports*, *8*(1), 1–15. https://doi.org/10.1038/s41598-018-22939-w

Lechthaler, S., Waldschläger, K., Stauch, G., & Schüttrumpf, H. (2020). The way of macroplastic through the environment. *Environments*, *7*(10), 73. https://doi.org/10.3390/environments7100073

Lenzi, J., Burgues, M. F., Carrizo, D., Machín, E., & Teixeira-de Mello, F. (2016). Plastic ingestion by a generalist seabird on the coast of Uruguay. *Marine Pollution Bulletin*, *107*(1), 71–76. https://doi.org/10.1016/j.marpolbul.2016.04.016

Li, Z., Venkateshwaran, A., & Karimpour, S. (2021). Turbulent characteristics and air entrainment patterns in breaking surge waves. *Fluids*, *6*(12), 422. https://doi.org/10.3390/fluids6120422

Liang, J. H., Wan, X., Rose, K. A., Sullivan, P. P., & McWilliams, J. C. (2018). Horizontal dispersion of buoyant materials in the ocean surface boundary layer. *Journal of Physical Oceanography*, *48*(9), 2103–2125. https://doi.org/10.1175/JPO-D-18-0020.1

Lusher, A. L., Hernandez-Milian, G., O'Brien, J., Berrow, S., O'Connor, I., & Officer, R. (2015). Microplastic and macroplastic ingestion by a deep diving, oceanic cetacean: The True's beaked whale Mesoplodon mirus. *Environmental Pollution*, *199*, 185–191. https://doi.org/10.1016/j.envpol.2015.01.023

Maharana, D., Saha, M., Dar, J. Y., Rathore, C., Sreepada, R. A., Xu, X. R., Koongolla, J. B., & Li, H. X. (2020). Assessment of micro and macroplastics along the west coast of India: Abundance, distribution, polymer type and toxicity. *Chemosphere*, *246*, 125708. https://doi.org/10.1016/j.chemosphere.2019.125708

Mallick, S. (2015). Blob Detection Using OpenCV (Python, C++). *LearnOpenCV*. Retrieved June 15, 2020, from https://learnopencv.com/blob-detection-using-opencv-python-c/

Mason, S. A., Kammin, L., Eriksen, M., Aleid, G., Wilson, S., Box, C., Williamson, N., & Riley, A. (2016). Pelagic plastic pollution within the surface waters of Lake Michigan, USA. *Journal of Great Lakes Research*, *42*(4), 753–759. https://doi.org/10.1016/j.jglr.2016.05.009

Matsuoka, T., Nakashima, T., & Nagasawa, N. (2005). A review of ghost fishing: scientific approaches to evaluation and solutions. *Fisheries Science, 71*(4), 691-702. https://link.springer.com/article/10.1111/j.1444-2906.2005.01019.x

Maximenko, N., Hafner, J., & Niiler, P. (2012). Pathways of marine debris derived from trajectories of Lagrangian drifters. *Marine Pollution Bulletin*, *65*(1–3), 51–62. https://doi.org/10.1016/j.marpolbul.2011.04.016

McGoran, A. R., Maclaine, J. S., Clark, P. F., & Morritt, D. (2021). Synthetic and Semi-Synthetic Microplastic Ingestion by Mesopelagic Fishes From Tristan da Cunha and St Helena, South Atlantic. *Frontiers in Marine Science*, *8*, 78. https://doi.org/10.3389/fmars.2021.633478

Meijer, L. J. J., van Emmerik, T., van der Ent, R., Schmidt, C., & Lebreton, L. (2021). More than 1000 rivers account for 80% of global riverine plastic emissions into the ocean. *Science Advances*, *7*(18), eaaz5803. https://doi.org/10.1126/sciadv.aaz5803

Ministry of the Environment, Japan. (2012). *Estimated total amount of debris washed out by the Great East Japan Earthquake*. Retrieved June 25, 2020, from http://www.env.go.jp/en/focus/docs/files/20120901-57.pdf

Mizukawa, K., Takada, H., Takeuchi, I., Ikemoto, T., Omori, K., & Tsuchiya, K. (2009). Bioconcentration and biomagnification of polybrominated diphenyl ethers (PBDEs) through lower-trophic-level coastal marine food web. *Marine Pollution Bulletin*, *58*(8), 1217–1224. https://doi.org/10.1016/j.marpolbul.2009.03.008

Moore, E., Lyday, S., Roletto, J., Litle, K., Parrish, J. K., Nevins, H., Harvey, J., Mortenson, J., Greig, D., Piazza, M., Hermance, A., Lee, D., Adams, D., Allen, S., & Kell, S. (2009). Entanglements of marine mammals and seabirds in central California and the north-west coast of the United States 2001-2005. *Marine Pollution Bulletin*, *58*(7), 1045–1051. https://doi.org/10.1016/j.marpolbul.2009.02.006

Moore, M., Andrews, R., Austin, T., Bailey, J., Costidis, A., George, C., Jackson, K., Pitchford, T., Landry, S., Ligon, A., Mclellan, W., Morin, D., Smith, J., Rotstein, D., Rowles, T., Slay, C., & Walsh, M. (2013). Rope trauma, sedation, disentanglement, and monitoring-tag associated lesions in a terminally entangled North Atlantic right whale (Eubalaena glacialis). *Marine Mammal Science*, *29*(2), E98–E113. https://doi.org/10.1111/j.1748-7692.2012.00591.x

Mrosovsky, N., Ryan, G. D., & James, M. C. (2009). Leatherback turtles: The menace of plastic. *Marine Pollution Bulletin*, *58*(2), 287–289. https://doi.org/10.1016/j.marpolbul.2008.10.018

Nakashima, E., Isobe, A., Kako, S., Itai, T., & Takahashi, S. (2012). Quantification of Toxic Metals Derived from Macroplastic Litter on Ookushi Beach, Japan. *Environmental Science & Technology*, *46*(18), 10099–10105. https://doi.org/10.1021/es301362g

National Oceanography Centre UK. (2020). There is at least 10 times more plastic in the Atlantic than previously thought. *ScienceDaily*. Retrieved September 20, 2020, from www.sciencedaily.com/releases/2020/08/200818114940.htm

NOAA. (2013). Thermohaline Circulation - Currents: NOAA's National Ocean Service Education. *NOAA's National Ocean Service*. Retrieved October 21, 2020, from https://oceanservice.noaa.gov/education/tutorial_currents/05conveyor1.html

Ohta, S., Ishizuka, D., Nishimura, H., Nakao, T., Aozasa, O., Shimidzu, Y., Ochiai, F., Kida, T., Nishi, M., & Miyata, H. (2002). Comparison of polybrominated diphenyl ethers in fish, vegetables, and meats and levels in human milk of nursing women in Japan. *Chemosphere*, *46*(5), 689–696. 10.1016/s0045-6535(01)00233-8

Onink, V., Wichmann, D., Delandmeter, P., & van Sebille, E. (2019). The Role of Ekman Currents, Geostrophy, and Stokes Drift in the Accumulation of Floating Microplastic. *Journal of Geophysical Research: Oceans*, *124*(3), 1474–1490. https://doi.org/10.1029/2018JC014547

Osinga, N., & 't Hart, P. (2006). Fish-Hook Ingestion in Seals (Phoca vitulina and Halichoerus grypus): The Scale of the Problem and a Non-Invasive Method for Removing Fish-Hooks. *Aquatic Mammals*, *32*(3), 261–264. https://doi.org/10.1578/am.32.3.2006.261

Pabortsava, K., & Lampitt, R. S. (2020). High concentrations of plastic hidden beneath the surface of the Atlantic Ocean. *Nature Communications*, *11*(1), 1–11. https://doi.org/10.1038/s41467-020-17932-9

Page, B., McKenzie, J., McIntosh, R., Baylis, A., Morrissey, A., Calvert, N., Haase, T., Berris, M., Dowie, D., Shaughnessy, P. D., & Goldsworthy, S. D. (2004). Entanglement of Australian sea lions and New Zealand fur seals in lost fishing gear and other marine debris before and after Government and industry attempts to reduce the problem. *Marine Pollution Bulletin*, *49*(1–2), 33–42. https://doi.org/10.1016/j.marpolbul.2004.01.006

Pincetich, C., Shore, T., & Steiner, T. (2010). *A Ban on Plastic Bags Will Save the Lives of California's Endangered Leatherback Sea Turtles*. Sea Turtle Restoration Project. Retrieved June 16, 2021, from http://seaturtles.org/article.php?id=1751

Plastics Europe. (2019). *Plastics – the Facts 2019*. Retrieved June 26, 2020, from https://plasticseurope.org/wp-content/uploads/2021/10/2019-Plastics-the-facts.pdf

Plastics Europe. (2020). *Plastics – the Facts 2020*. Retrieved January 1, 2021, from https://plasticseurope.org/wp-content/uploads/2021/09/Plastics_the_facts-WEB-2020_versionJun21_final.pdf

Pohl, F., Eggenhuisen, J. T., Kane, I. A., & Clare, M. A. (2020). Transport and Burial of Microplastics in Deep-Marine Sediments by Turbidity Currents. *Environmental Science and Technology*, *54*(7), 4180–4189. https://doi.org/10.1021/acs.est.9b07527

Quinlan, N. J., & Dooley, P. N. (2007). Models of flow-induced loading on blood cells in laminar and turbulent flow, with application to cardiovascular device flow. *Annals of Biomedical Engineering*, *35*(8), 1347–1356. https://doi.org/10.1007/s10439-007-9308-8

Rasband, W. S. (1997). *ImageJ*. U. S. National Institutes of Health, Bethesda, Maryland, USA. Retrieved May 13, 2020, from https://imagej.nih.gov/ij/

Rochman, C. M., Browne, M. A., Halpern, B. S., Hentschel, B. T., Hoh, E., Karapanagioti, H. K., Rios-Mendoza, L. M., Takada, H., Teh, S., & Thompson, R. C. (2013). Classify plastic waste as hazardous. *Nature*, *494*(7436), 169–171. https://doi.org/10.1038/494169a

Rochman, C. M., Tahir, A., Williams, S. L., Baxa, D. v., Lam, R., Miller, J. T., Teh, F. C., Werorilangi, S., & Teh, S. J. (2015). Anthropogenic debris in seafood: Plastic debris and fibers from textiles in fish and bivalves sold for human consumption. *Scientific Reports*, *5*(1), 1–10. https://doi.org/10.1038/srep14340

Rodríguez, B., Bécares, J., Rodríguez, A., & Arcos, J. M. (2013). Incidence of entanglements with marine debris by northern gannets (Morus bassanus) in the non-breeding grounds. *Marine Pollution Bulletin*, *75*(1–2), 259–263. https://doi.org/10.1016/j.marpolbul.2013.07.003

Ryan, P. G. (2018). Entanglement of birds in plastics and other synthetic materials. *Marine Pollution Bulletin*, *135*, 159–164. https://doi.org/10.1016/j.marpolbul.2018.06.057

Ryan, P. G., Dilley, B. J., Ronconi, R. A., & Connan, M. (2019). Rapid increase in Asian bottles in the South Atlantic Ocean indicates major debris inputs from ships. *Proceedings of the National Academy of Sciences of the United States of America*, *116*(42), 20892–20897. https://doi.org/10.1073/pnas.1909816116

Sadri, S. S., & Thompson, R. C. (2014). On the quantity and composition of floating plastic debris entering and leaving the Tamar Estuary, Southwest England. *Marine Pollution Bulletin*, *81*(1), 55–60. https://doi.org/10.1016/j.marpolbul.2014.02.020

Santos, R. G., Machovsky-Capuska, G. E., & Andrades, R. (2021). Plastic ingestion as an evolutionary trap: Toward a holistic understanding. *Science*, *373*(6550), 56–60. https://doi.org/10.1126/science.abh0945

Schmidt, C., Krauth, T., & Wagner, S. (2017). Export of Plastic Debris by Rivers into the Sea. *Environmental Science and Technology*, *51*(21), 12246–12253. https://doi.org/10.1021/acs.est.7b02368

Schuyler, Q. A., Wilcox, C., Townsend, K. A., Wedemeyer-Strombel, K. R., Balazs, G., van Sebille, E., & Hardesty, B. D. (2016). Risk analysis reveals global hotspots for marine debris ingestion by sea turtles. *Global Change Biology*, *22*(2), 567–576. https://doi.org/10.1111/gcb.13078

Schwarz, A. E., Ligthart, T. N., Boukris, E., & van Harmelen, T. (2019). Sources, transport, and accumulation of different types of plastic litter in aquatic environments: A review study. *Marine Pollution Bulletin*, *143*, 92–100. https://doi.org/10.1016/j.marpolbul.2019.04.029

Secretariat of the Convention on Biological Diversity. (2016). *Marine Debris: Understanding, Preventing and Mitigating the Significant Adverse Impacts on Marine and Coastal Biodiversity.* CBD Technical Series No. 83. Retrieved June 30, 2020, from https://www.cbd.int/doc/publications/cbd-ts-83-en.pdf

Secretariat of the Convention on Biological Diversity and the Scientific and Technical Advisory Panel – GEF. (2012). *Impacts of marine debris on biodiversity: current status* *and potential solutions.* CBD Technical Series No. 67. Retrieved November 17, 2021, from https://wedocs.unep.org/20.500.11822/32622.

Shamskhany, A., Li, Z., Patel, P., & Karimpour, S. (2021). Evidence of Microplastic Size Impact on Mobility and Transport in the Marine Environment: A Review and Synthesis of Recent Research. *Frontiers in Marine Science*, *8*. https://doi.org/10.3389/fmars.2021.760649

Singhal, P., Rodriguez, J. N., Small, W., Eagleston, S., van de Water, J., Maitland, D. J., & Wilson, T. S. (2012). Ultra low density and highly crosslinked biocompatible shape memory polyurethane foams. *Journal of Polymer Science, Part B: Polymer Physics*, *50*(10), 724–737. https://doi.org/10.1002/polb.23056

Smith, B. L., & Neal, D. R. (2016). Particle Image Velocimetry. In R. W. Johnson (Ed.), *Handbook of Fluid Dynamics, 2*, (48-1–48-27). CRC Press.

Stelfox, M., Hudgins, J., & Sweet, M. (2016). A review of ghost gear entanglement amongst marine mammals, reptiles and elasmobranchs. *Marine Pollution Bulletin*, *111*(1–2), 6–17. https://doi.org/10.1016/j.marpolbul.2016.06.034

Takahashi, M., & Ohtsu, I. (2017). Effects of inflows on air entrainment in hydraulic jumps below a gate. *Journal of Hydraulic Research*, *55*(2), 259–268. https://doi.org/10.1080/00221686.2016.1238016

The Litterboom Project. (2020). Plastic Waves 2020. YouTube. Retrieved December 14, 2021, from https://www.youtube.com/watch?v=1Az-mN01W4s

Thiel, M., Luna-Jorquera, G., álvarez-Varas, R., Gallardo, C., Hinojosa, I. A., Luna, N., Miranda-Urbina, D., Morales, N., Ory, N., Pacheco, A. S., Portflitt-Toro, M., & Zavalaga, C. (2018). Impacts of marine plastic pollution from continental coasts to subtropical gyres-fish, seabirds, and other vertebrates in the SE Pacific. *Frontiers in Marine Science*, *5*, 238. https://doi.org/10.3389/fmars.2018.00238

US Department of Energy, National Energy Technology Laboratory. (2019a). *Tracker* (19.1). Retrieved December 8, 2020, from https://mfix.netl.doe.gov/tracker/

US Department of Energy, National Energy Technology Laboratory. (2019b). *Tracker's documentation*. Retrieved December 20, 2020, from https://mfix.netl.doe.gov/products/tracker/tracker-documentation/

van Cauwenberghe, L., & Janssen, C. R. (2014). Microplastics in bivalves cultured for human consumption. *Environmental Pollution*, *193*, 65–70. https://doi.org/10.1016/j.envpol.2014.06.010

van Franeker, J. A., Blaize, C., Danielsen, J., Fairclough, K., Gollan, J., Guse, N., Hansen, P. L., Heubeck, M., Jensen, J. K., le Guillou, G., Olsen, B., Olsen, K. O., Pedersen, J., Stienen, E. W. M., & Turner, D. M. (2011). Monitoring plastic ingestion by the northern fulmar Fulmarus glacialis in the North Sea. *Environmental Pollution*, *159*(10), 2609–2615. https://doi.org/10.1016/j.envpol.2011.06.008

van Franeker, J. A., & Law, K. L. (2015). Seabirds, gyres and global trends in plastic pollution. *Environmental Pollution*, *203*, 89–96. https://doi.org/10.1016/j.envpol.2015.02.034

van Utenhove, E. (2019). *Modelling the transport and fate of buoyant macroplastics in coastal waters*, Master of Science thesis. Delft University of Technology.

Waluda, C. M., & Staniland, I. J. (2013). Entanglement of Antarctic fur seals at Bird Island, South Georgia. *Marine Pollution Bulletin*, *74*(1), 244–252. https://doi.org/10.1016/j.marpolbul.2013.06.050

Wang, H., & Chanson, H. (2015). Air entrainment and turbulent fluctuations in hydraulic jumps. *Urban Water Journal*, *12*(6), 502–518. https://doi.org/10.1080/1573062X.2013.847464

Wardrop, P., Shimeta, J., Nugegoda, D., Morrison, P. D., Miranda, A., Tang, M., & Clarke, B. O. (2016). Chemical Pollutants Sorbed to Ingested Microbeads from Personal Care Products Accumulate in Fish. *Environmental Science and Technology*, *50*(7), 4037–4044. https://doi.org/10.1021/acs.est.5b06280

Weber, J., Bobek, M., Rowan, S., Yang, J., & Breault, R. (2019). Tracker: An opensource particle tracking velocimetry (PTV) application applied to multiphase flow reactors. *ASME-JSME-KSME 2019 8th Joint Fluids Engineering Conference*, *5*. https://doi.org/10.1115/AJKFluids2019-5181

Wilcox, C., van Sebille, E., Hardesty, B. D., & Estes, J. A. (2015). Threat of plastic pollution to seabirds is global, pervasive, and increasing. *Proceedings of the National Academy of Sciences of the United States of America*, *112*(38), 11899–11904. https://doi.org/10.1073/pnas.1502108112

Xie, P., & Chu, V. H. (2019). The forces of tsunami waves on a vertical wall and on a structure of finite width. *Coastal Engineering*, *149*, 65–80. https://doi.org/10.1016/j.coastaleng.2019.03.013

Yamashita, R., Takada, H., Fukuwaka, M. aki, & Watanuki, Y. (2011). Physical and chemical effects of ingested plastic debris on short-tailed shearwaters, Puffinus tenuirostris, in the North Pacific Ocean. *Marine Pollution Bulletin*, *62*(12), 2845–2849. https://doi.org/10.1016/j.marpolbul.2011.10.008

Ye, S., & Andrady, A. L. (1991). Fouling of floating plastic debris under Biscayne Bay exposure conditions. *Marine Pollution Bulletin*, *22*(12), 608–613. https://doi.org/10.1016/0025-326X(91)90249-R

Zbyszewski, M., & Corcoran, P. L. (2011). Distribution and degradation of fresh water plastic particles along the beaches of Lake Huron, Canada. *Water, Air, and Soil Pollution*, *220*(1), 365–372. https://doi.org/10.1007/s11270-011-0760-6

Zbyszewski, M., Corcoran, P. L., & Hockin, A. (2014). Comparison of the distribution and degradation of plastic debris along shorelines of the Great Lakes, North America. *Journal of Great Lakes Research*, *40*(2), 288–299. https://doi.org/10.1016/j.jglr.2014.02.012

Zeri, C., Adamopoulou, A., Bojanić Varezić, D., Fortibuoni, T., Kovač Viršek, M., Kržan, A., Mandic, M., Mazziotti, C., Palatinus, A., Peterlin, M., Prvan, M., Ronchi, F., Siljic, J., Tutman, P., & Vlachogianni, T. (2018). Floating plastics in Adriatic waters

(Mediterranean Sea): From the macro- to the micro-scale. *Marine Pollution Bulletin*, *136*, 341–350. https://doi.org/10.1016/j.marpolbul.2018.09.016

Zhang, J., Zheng, J., Jeng, D. S., & Guo, Y. (2015). Numerical simulation of solitary-wave propagation over a steady current. *Journal of Waterway, Port, Coastal and Ocean Engineering*, *141*(3), 1–11. https://doi.org/10.1061/(ASCE)WW.1943-5460.0000281